Investigation and Evaluation of Water Permeation through $BaCe_{0.8}Y_{0.2}O_{3-\delta}$ Electrolyte for Solid Oxide Fuel Cells

Selgin AL

A thesis submitted for the degree of Doctor of Philosophy (PhD) in Chemical Engineering at Newcastle University

School of Chemical Engineering and Advanced Materials

February 2016

Abstract

The commercial development of solid oxide fuel cells (SOFCs) is limited due to problems such as carbon deposition at the anode, temperature gradients in the cell and dilution of fuel at the anode. The purpose of this study is to investigate the feasibility of utilising a water permeable membrane in an SOFC with simultaneous water permeation. The idea is to transport water from cathode to anode for reforming of hydrocarbon fuels at the anode which could help overcome the above mentioned limitations.

A mathematical model is developed for hydration of $BaCe_{0.8}Y_{0.2}O_{3-\delta}$ (BCY20) and $BaCe_{0.9}Y_{0.1}O_{3-\delta}$ (BCY10) using the Nernst–Planck equation. This is used to calculate diffusion coefficients of protonic defects and oxygen vacancies (responsible for water permeation). The diffusion coefficients of protonic defects are found to be greater than oxygen vacancies within the membranes, which are in agreement with literature. The concentration of protonic defects increases rapidly at the hydration surface of the membrane following the introduction of water into the reaction chamber. This suggests that the presence of water initiates a rapid formation of protonic defects.

The water permeation for unmodified and catalytically modified BCY20 surfaces with platinum is measured between 500–800 °C. The feasibility of coupled water permeation with the water gas shift reaction (WGSR) is done at 700 °C. Data suggests that there is an increase in water permeation when the feed side surface is catalytically modified compared with unmodified surface. This implies that platinum catalyses water permeation by increasing the oxygen/hydrogen exchange rate on the feed side surface. However, the water permeation decreases when platinum is applied on the permeate side surface, indicating that platinum plays a blocking role in water recombination. When 1% carbon monoxide is supplied to the permeate side during the coupled water permeation with the WGSR study, a 1.5 fold increase in the water permeation is observed. The post operation x−ray diffraction analysis of membranes revealed that BCY20 decomposed to cerium oxide and barium carbonate.

The study also explored the simultaneous water and oxygen transport through BCY20. Results demonstrated that water transport is independent of externally applied potential. Additionally, there is no dramatic change observed in oxygen transport due to presence of water in air at the cathode. Fuel cells fuelled with carbon monoxide or methane displayed low power densities compared to conventional SOFCs due to insufficient water permeation and low catalytic activity of anode towards reforming reactions as well as carbon deposition.

Acknowledgements

I would first of all like to acknowledge the Ministry of National Education of Turkey, my sponsor, for financial support.

I would like to thank my supervisors, Prof Ian Metcalfe and Dr Evangelos Papaioannou, for their supervision and advice throughout my study. I would also like to thank Dr Danai Poulidi for her guidance and help in the laboratory in the early stage of the study.

My sincere appreciation is extended to Dr Guangru Zhang and Dr Feng Song for their useful advice, support and help. I would like to acknowledge Dr Feng Song for his help with the model and software. Next, I would like to thank technical and administrative stuff of the Newcastle University.

Special thanks and appreciation go to my family. I am grateful for their support and patience. I would further like to thank Dr Deniz Sarica, Prasna Ray, Sotiria Tsochataridou and Dr Claire Thompson for being such great friends.

Table of Contents

List of Figures

List of Tables

Nomenclature

List of acronyms

SOFC	Solid oxide fuel cell
MCFC	Molten carbonate fuel cell
BCY	Yttrium–doped barium cerate
BCG	Gadolinium–doped barium cerate
BCY20	20 mol% yttrium–doped barium cerate
AFC	Alkaline fuel cell
PEMFC	Proton exchange membrane fuel cell
PAFC	Phosphoric acid fuel cell
YSZ	Yttria–stabilised zirconia
LSGM	$La_{0.8}Sr_{0.2}Ga_{0.8}Mg_{0.2}O_{2.8}$
CGO	Gadolinium–doped ceria
CSO	Samarium–doped ceria
TGA	Thermo–gravimetric analysis
IT–SOFC	Intermediate temperature solid oxide fuel cell
BCY10	10 mol% yttrium–doped barium cerate
STP	Standard temperature and pressure
MFC	Mass flow controller
XRD	X–ray diffraction
SEM	Scanning electron microscopy
EDXS	Energy dispersive X–rays spectroscopy
LSCF	$La_{0.6}Sr_{0.4}Co_{0.2}Fe_{0.8}O_{3-\delta}$
WGSR	Water gas shift reaction
WE	Working electrode
CE	Counter electrode
OCP	Open circuit potential
DC	Direct current

List of symbols

$e^{'}$	Electron
F	Faraday`s constant (96485 C/mol)
N	Avogadro's number
n	Amounts of electrons
E	Reversible open circuit voltage
ΔG	Change in Gibbs–free energy (J/mol)
ΔH	Change in enthalpy of reaction (J/mol)
ΔS	Change in entropy of reaction (J/K.mol)
T	Temperature
ΔG^{0}	Change in standard state Gibbs–free energy
R	Universal gas constant (8.314 J/K.mol)
P	Partial pressure of species
Cp	Heat capacity of species
E^{0}	Standard cell voltage
A	Electron transfer coefficient
i_0	Exchange current density
η_{act}	Activation overpotential
η_{ohm}	Ohmic overpotential
I	Current
R	Ohmic resistance (not to be confused with universal gas constant)
η_{cont}	Concentration overpotential
i_L	Limiting current density
t	Goldschmidt tolerance factor
r_A	Radius of the A-site cation
r_B	Radius of the B-site cation
r_O	Radius of the lattice oxygen
δ	Oxygen deficiency
K	Equilibrium constant
S	Effective dopant concentration
ΔH^{0}	Hydration enthalpy

ΔS^0	Hydration entropy
$\widetilde{D}_{H_2O}$	Chemical diffusion coefficient of water
$D_{OH_o^{\bullet}}$	Diffusion coefficient of protonic defects
$D_{V_o^{\bullet\bullet}}$	Diffusion coefficient of oxygen vacancies
J_{H_2O}	Water flux
J	Mass transfer flux (mol/m^2.s)
u	Convection rate (m/s)
C	Concentration (mol/m^3)
∇V	Electrical potential difference (V)
z	Charge number of species
k_B	Boltzman constant
U	Mobility of ions (m^2/V.s)
R_e	Reaction rate (mol/m^2.s)
k_f	Film mass transfer coefficient (m/s)
C_{out}	Bulk concentration (mol/m^3)
k_1	Forward reaction rate constant (m^2/mol.s)
k_2	Reverse reaction rate constant (m^2/mol.s)
$P^*_{H_2O}$	Partial pressure of water on the membrane surface
R_a	The value of reaction rate (m^2/mol.s)
P_0	Atmospheric pressure (Pa)
S	Surface area (m^2)
Δt	Time interval (s)
Δx	Space interval (m)
L	Membrane thickness
Tpb	Three–phase boundaries
$h^{\bullet}$	Electron holes
V_{WR}	Potential between working and reference electrodes (V)
η	Overpotential (V)
$V_o^{\bullet\bullet}$	Oxygen vacancy
O_o^x	Lattice oxygen
$OH_o^{\bullet}$	Hydroxide species

Chapter 1
Introduction

1.1 Overview

One of the main concerns of society is to produce clean and environmentally friendly energy from renewable sources by shifting from high carbon technology to low carbon technology. The use of traditional techniques such as combustion based power plants depend on fossil fuels. The standard way of producing energy relies on transforming chemical energy of a fossil fuel into thermal energy, then mechanical energy and finally electrical energy in terms of producing stationary power which decreases the transformation efficiency and increases the production of CO_2. Although being industrially relevant, use of fossil fuels to generate power had led to the phenomena of global warming. Therefore, it is vital for the future to implement new efficient and environmentally friendly energy technologies.

Fuel cells are electrochemical devices which can directly convert the chemical energy of fuels into electrical energy. This can offer to the world a prospect of power generation with lower pollutant emission and high energy efficiency. These devices have wide applications such as combined heat and power systems, domestic heat and power, portable power and transportation [1]. Especially, stationary fuel cell systems are attractive due to the fact that they have potential to compete with the current technologies in terms of efficiency and cost. High temperature fuel cells such as solid oxide fuel cells (SOFCs) and molten carbonate fuel cells (MCFCs) can use natural gas or hydrocarbon fuels without the need for external reformer to convert the fuel to hydrogen. Therefore, they can eliminate the need for hydrogen production and storage. Moreover, the overall efficiency of the high temperature fuel cells can be increased up to 70% by using combined systems such as SOFC–gas turbine to use the waste heat to produce electricity [1, 2]. The gas turbine can be run by the SOFC exhaust.

One of the strongest candidates in fuel cell technology is solid oxide fuel cells owing to their high conversion efficiency and fuel flexibility. This type of cell offers using a range of fuels obtained from fossil fuels to synthetic hydrocarbons produced from biomass and other renewable sources (i.e. electrolysis) [3]. A conventional SOFC utilises an oxide ion conducting ceramic electrolyte, usually yttria–stabilised zirconia operating at elevated temperature (750–1000 °C) [4]. However, operation of an SOFC at high temperature has limitations such as longer start up time, electrode sintering, catalyst poisoning, thermal stress and expensive interconnect materials [5]. A period is required to burn fuel in order to reach the operating temperature. In addition, the thermal mismatch due to different thermal coefficients of cell components can cause mechanical failure of the cell. Agglomeration of metal electrodes at high operational temperature reduces active surface area of electrodes. Due to those operational limitations of high temperature SOFC's, developments in SOFC technology is recently focused on lowering the operating temperature (500–800 °C) and enhancing the ionic conductivity of electrolyte. Enhancement of conductivity of electrolyte is concentrated on two major approaches; investigation of new materials and improvement of existing materials. One of the approaches in development of new materials is based on proton conducting electrolytes which show high protonic conductivity at intermediate temperatures (500–800 °C) and can utilise hydrocarbon fuels such as natural gas.

SOFCs use hydrogen or a mixture of hydrogen and carbon monoxide obtained by internal reforming of hydrocarbons or natural gas. Internal reforming of a fuel is more effective than external reforming due to the fact that no additional system for hydrogen production and storage is required. This reduces heat losses and expense of SOFCs. However, there are several limitations with internal reforming which are needed to be overcome. One of the major issues with use of carbon containing fuel is carbon deposition (coking) owing to hydrocarbon pyrolysis, especially when a nickel containing anode is used. (Nickel is typically used as an electrode for high temperature fuel cells.) Coking causes deactivation of the anode very rapidly when the fuel cell is operated at temperatures below 850 °C [6].

In addition to carbon build up, temperature gradient along the cell is another major issue. For instance, steam reforming of methane is a fast endothermic reaction that takes place at the fuel entry of the fuel cell whereas exothermic fuel cell reactions take place slowly in the cell. This results in instabilities and sub–cooling in this section of the SOFC. This temperature gradient

is very difficult to control and causes cracking of the anode and the electrolyte due to mechanical failure (owing to thermal stress). An increase in ohmic losses in the electrolyte and over potentials at the electrodes is caused due to this thermo–mechanical failure of the SOFC [7-9].

The SOFCs require addition of water to the anode especially at low and intermediate temperature to produce hydrogen from hydrocarbon fuel which is typically achieved via internal steam reforming reaction. This dilutes the fuel at the anode, which decreases the fuel cell efficiency, increasing complexity of the system and generates water management issues. Even though new anode materials have been investigated for direct oxidation of methane, direct oxidation increases the amount of unused fuel and decreases the efficiency of the cell. Direct oxidation of methane is a great challenge due to low catalytic activity of the anode and carbon formation because of methane decomposition [8]. The use of ceramic water permeable solid electrolytes could prevent SOFCs from these limitations. Perovskite–type ceramics such as yttrium or gadolinium–doped barium cerate (BCY and BCG) display high proton conduction along with water permeation [10, 11]. In particular, yttrium–doped barium cerate has shown highest conductivity and selective water permeation [12, 13]. The incorporation of water occurs at the surface of the material under humidified conditions according to Equation 1.1 (in Kröger–Vink notation).

$$H_2O + V_o^{\bullet\bullet} + O_o^x \leftrightarrow 2OH_o^{\bullet} \qquad 1.1$$

where, $V_o^{\bullet\bullet}$ represents an oxygen vacancy at an oxygen site, O_o^x represents lattice oxygen and $OH_o^{\bullet}$ represents a proton at an oxygen site. Water enters the crystal lattice of the ceramic at high water partial pressure on the surface by reacting with one oxygen vacancy and one occupied oxygen site and forms two hydroxyl species (Equation 1.1). Protons then can migrate by hopping from one hydroxide site to another (Grotthuss mechanism) and finally reacts with available surface oxygen atom to form water at the low water partial pressure surface [14, 15]. Further detailed water transport mechanism is explained in *Section 2.5.*

In the current study water permeability feature would be applied to allow ceramic materials such as $BaCe_{0.8}Y_{0.2}O_{3-\delta}$ (BCY20) to provide water permeation across the cell. This could reduce the need for addition of water into the anode side of the cell in the case of internal

reforming. Hence, fuel dilution limitation can be overcome. The conversion of fuel and the overall efficiency of the cell may increase. Additionally, water permeation across the cell could facilitate carbon removal. Permeated water from cathode to anode can react with carbon and form carbon dioxide and hydrogen. This could make the use of hydrocarbon fuels possible without carbon deposition.

Water permeation could provide less complex reforming steps in the cell. Since water permeation will occur from the cathode through the electrolyte to the anode, the addition of water to fuel at the anode may be reduced. Even at a later stage the addition of water to the anode may be interrupted owing to the fact that product water will be available as a result of electrochemical cell reactions at both anode and cathode. In the case of use of methane as fuel, CO and H species will be produced as a result of steam reforming reaction and oxidised electrochemically at the triple–phase boundaries (the solid electrolyte–anode–gas interface) of the anode side to form water and carbon dioxide. Therefore, high thermal efficiency, lower temperature gradient and uniform fuel distribution may be achieved along with reduced coking due to distributed water permeation. Furthermore, the exothermic fuel cell reactions can provide the necessary heat required for the endothermic hydrocarbon reforming reaction, such as steam reforming of methane. The SOFC would thus behave as a heat exchange membrane reactor.

1.2 Project Rationale

Researchers have looked at the structural evolution, phase transitions from room temperature to high temperature, thermal analysis and electrical conductivity studies for yttrium doped barium cerates so far [16-20]. A few research groups have studied hydration thermodynamics of materials such as lanthanum tungstate, barium cerate and zirconate using thermogravimetric analysis [21-23]. These studies mostly involved determination of the standard enthalpy and entropy of hydration of the materials. In addition, there are still on–going research on rare earth metal yttrium doped barium cerates and mixed barium cerate/barium zirconate as electrolytes for SOFCs [24-26]. However, most of the research has focused on different fabrication methods, utilisation of humidified H_2 or dry H_2 as a fuel and air or O_2 as oxidant, conductivity measurements, sinter activity, chemical stability [24, 27-32].

These reports have not investigated the water transport features of proton conductors in terms of internal reforming and use of hydrocarbon fuels via water permeation in a fuel cell. For such an approach to be viable it is important to understand the mechanism of water transport and specifically the nature of the surface sites that are required for water incorporation into the membrane as well as water evolution. It is also crucial to confirm that water permeation can occur without compromising power output (as fuel oxidation leads to water production anyway). Thus, there is a need for determining to what extent the water permeation will be beneficial for this system. This type of novel SOFC (which can act as a fuel cell, a water permeator and a heat exchanger) is a complex device and has not been investigated in literature to the best of the author's knowledge.

The overall aim of this study is to investigate yttrium–doped barium cerate in terms of water permeation behaviour along with multi–species transport at the intermediate temperature (500–800 °C) and its application on a solid oxide fuel cell including simultaneous water permeation. This feature will be evaluated in terms of internal reforming for the cell. The mechanistic understanding of water permeation coupled with hydrocarbon SOFC, can also allow rational design of fuel cells for improved water permeation and performance.

Figure 1.1 presents a schematic of the distributed water introduction in an operational solid oxide fuel cell. Water and air are introduced at the cathode where protonic defects are created as a result of the reaction between water, oxygen vacancies and the lattice oxygen. (Water does not diffuse as molecules, but rather as a result of diffusion of protonic defects and oxygen vacancies within the material). The cathode here represents the high partial pressure of the water surface and the anode represents the low partial pressure of the water surface. The chemical potential difference of water between cathode and anode creates continuum driving force for water permeation in the cell. The permeated water is consumed in the internal hydrocarbon reforming reactions at the anode where protons and electrons are also formed as a part of the fuel cell reaction (e.g. the fuel is chosen as methane). This should result in direct internal reforming and reduce fuel cell temperature gradients (due to distributed water permeation) compared to conventional internal reforming as well as facilitate carbon removal which could make the use of hydrocarbons possible without carbon deposition. Even, injection of water to cathode may be interrupted at a later stage since water will be produced as a result of anode and cathode electrochemical reactions which can be used

for reforming reactions without the need for addition of water to cathode (probably at high current densities). The final system could theoretically be self–sustained in water supply.

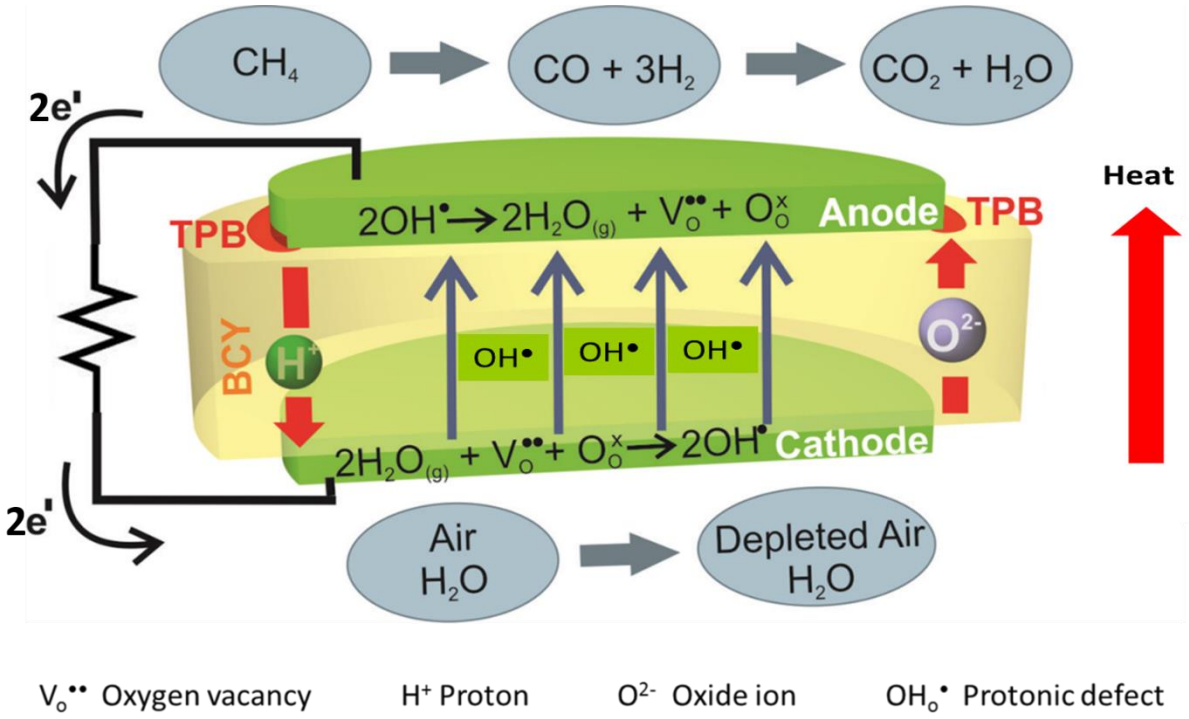

Figure 1.1: A schematic representation of a working solid oxide fuel cell with simultaneous water permeation, $V_o^{\bullet\bullet}$ represents an oxygen vacancy at an oxygen site, O_o^x represents a lattice oxygen and $OH_o^{\bullet}$ represents a proton at an oxygen site (protonic defect). The transport of water takes place via protons that hop between hydroxide sites and counter diffusion of oxygen vacancies throughout the membrane from the cathode to the anode. The electrons are transported via the external circuit. The steam reforming reaction takes place at the anode to produce hydrogen and carbon monoxide. Carbon monoxide further undergoes water gas shift reaction to produce hydrogen and carbon dioxide. The heat is transferred to the anode for endothermic reforming reactions.

In order to study the practicability of the concept described above the following objectives are evaluated.

1. Hydration behaviour of BCY membrane and defect distribution during hydration and extract diffusion coefficients of defects.
2. The water permeation flux of BCY20 membrane under different temperatures.
3. The effect of surface modification on water permeation.

4. The ability and stability of BCY20 membrane for coupled water gas shift reaction (WGSR) and water permeation in addition to the role of surface modification.
5. The effect of simultaneous oxygen and water transport on water and oxygen transport in one membrane reactor.
6. The fuel cell performances with simultaneous water permeation via utilisation of different fuels.

1.3 Thesis Organisation

This thesis is comprised of seven chapters. *Chapter 1* gave a general overview and introduction of the project. *Chapter 2* presents a literature survey regarding fuel cells, perovskite structure, electrolyte materials, water permeation mechanism related to defect chemistry. *Chapter 3* describes the membrane preparation process, reactor module, experimental protocol, the list of experiments that were performed, the fundamental of the analytical techniques that were used to analyse structure, morphology and texture of the membrane as well as the studied high temperature membrane sealant materials which is crucial for permeation experiments. *Chapter 4* provides information about investigation of hydration and dehydration behaviour of the membrane and exploration defect distribution during hydration and extraction of diffusion coefficient of defects. *Chapter 5* characterises the membrane and discusses water permeation of the membrane at different temperatures as well as the effect of surface modification on water permeation. The feasibility of water gas shift reaction via water permeation and post operation analysis are also presented. *Chapter 6* investigates the effect of simultaneous oxygen and water transport on water and oxygen permeation. Besides, an evolution of the fuel cell performances with simultaneous water permeation. Finally, *Chapter 7* discusses overall conclusions and recommendations for future work.

Chapter 2
Literature Survey

This chapter presents a brief introduction to fuel cells in *Section 2.1*, followed by details on SOFCs in Sec*tion 2.2*. The general thermodynamics of SOFCs are described in *Section 2.3*. The electrolyte materials based on the type of conducting species (charge carriers) are described in *Section 2.4*. Finally, *Section 2.5* contains information about BCY electrolyte material and its specific feature for water permeation. The transport mechanism for water permeation as well as reported experimental values is also described.

2.1 Introduction to Fuel Cells

Fuel cells are electrochemical devices which can convert directly the chemical energy of fuels into electrical energy through chemical reactions. A single fuel cell consists of two electrodes, anode and cathode, and an electrolyte which separates the two electrodes and ensures ionic conduction for fuel oxidation [33]. Although the charge carrier depends on the type of fuel cells, direct or indirect oxidation of fuels via reforming steps take place at the anode and oxygen reduction usually from air takes place at the cathode [34]. The electrolyte enables ionic conduction between anode and cathode and prevents direct combustion of fuel and oxidant. A schematic operation of a fuel cell along with directions for ion conduction across the cell is shown in Figure 2.1.

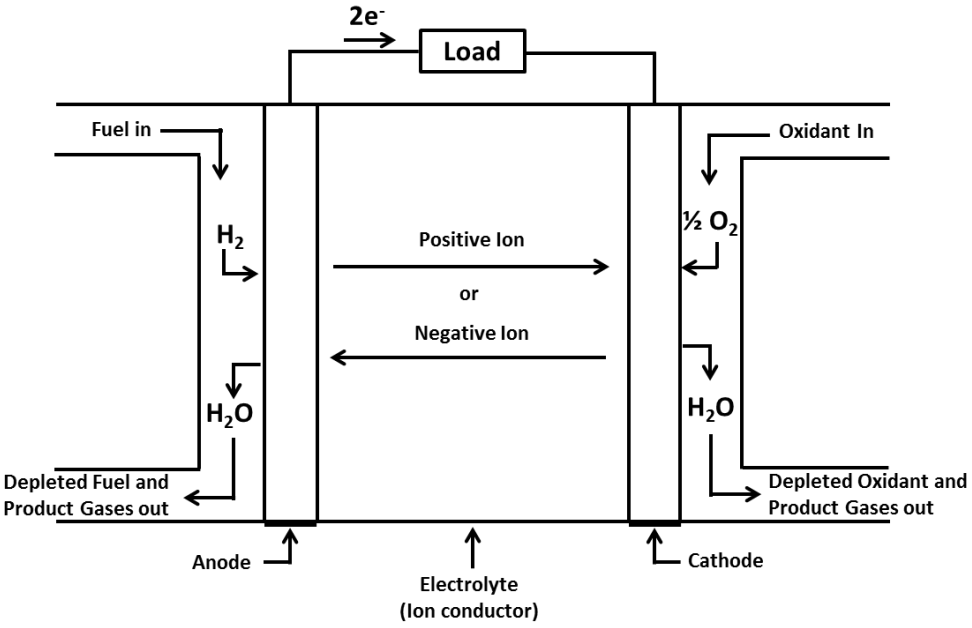

Figure 2.1: Schematic of a fuel cell consists of a porous anode and cathode and a dense electrolyte between them. Reactant gases are fed to anode and cathode inlets, product gases leave from anode and cathode outlets; directions of ions through electrolyte are shown. Electrons flow through an external circuit. [35].

The main types of fuel cells depending on the electrolyte type used, such as Alkaline (AFC), Proton Exchange Membrane or Polymer Electrolyte Membrane Fuel Cell (PEMFC), Phosphoric Acid Fuel Cell (PAFC), Molten Carbonate Fuel Cell (MCFC), Direct Methanol Fuel Cell (DMFC) and Solid Oxide Fuel Cell (SOFC) are presented in Table 2.1 including applications and specifications [36-38]. Each fuel cell operates with the same procedure, but differs from each other by charge carrier. MCFCs and SOFCs are also classified as high temperature fuel cells whereas AFCs, PEMFCs and PAFCs are classified as low temperature fuel cells.

Table 2-1: Summary of major different types of fuel cells based on the type of used electrolyte [34, 36-40]

Fuel Cell Type	Mobile ion	Temperature	Fuel	Common Electrolyte	Applications
Alkaline (AFC)	OH^-	50–200 °C	H_2	Aqueous KOH	Space vehicles and drinking water, i.e. UTC power
Proton exchange membrane (PEMFC)	H^+	70–110 °C	H_2, CH_3OH	Sulfonated polymers(Nafion™)	Transport and stationary power, i.e. Toyota Prius, Honda FCX.
Phosphoric acid (PAFC)	H^+	150–250 °C	H_2	H_3PO_4	Transport and stationary power, i.e. UTC fuel cell, Toshiba, Fuji Electric.
Molten carbonate (MCFC)	CO_3^{2-}	600–800 °C	Hydrocarbons, CO	$(Na,K)_2CO_3$	Stationary power, i.e. Fuel Cell Energy
Solid oxide (SOFC)	O^{2-}	800–1000 °C 500–600 °C possible	Hydrocarbons, CO	Y_2O_3-doped ZrO_2	Stationary power, i.e. Hexis, Vaillant, Ceres power
Direct methanol (DMFC)	H^+	80–110 °C	Methanol	Nafion	Transport, Portable, i.e. Toshiba, Ball Aerospace and Technologies

The first demonstration of a basic fuel was done by a lawyer and scientist William Grove in 1839 which was published in the Philosophical Magazine [41]. William Grove performed the experiment using two platinum electrodes and dilute acid electrolyte. Grove obtained a small current flowing through an external circuit [1]. In 1950s, a first 6 kW fuel cell was produced by Francis T. Bacon [41]. The first major application of fuel cells was included by the US Space program. The first polymer electrolyte membrane fuel cells (PEMFCs) were developed by General Electric and used in the program of Gemini in 1960s. In 1990s, PEMFCs were used to power submarines and produce cell–powered buses [36]. Many fuel cell technologies

and ideas have been under development since then. Fuel cells created very attractive new technology due to its–low/zero pollutant (no harmful pollutants such as NO_x and SO_x) and higher efficiency compared to conventional energy systems.

The SOFC technology has been attracting much attention among these five main types of fuel cells and many researchers and companies are investigating possible developments due to the fact that SOFCs are the most suitable and green sources for residential energy purposes and they have the ability to hybridise with gas turbines and combined heat power systems (CHPs) [4]. Such a hybrid system can reach the efficiency of 70% [2]. Besides, higher operation temperature SOFCs provide the fuel flexibility for hydrocarbons and higher fuel cell efficiency (has the highest conversion rate) at about 1000 °C among these fuel cells [42]. The uses of hydrocarbons eliminate the problems regarding with hydrogen production, storage, safety and cost. Recent developments focused on the intermediate temperature operation of SOFCs between 500–800 °C and development of the electrical performance of the cell. These include investigation of carbon/sulphur tolerant anodes, low cost current collectors, sealant materials and lowering the operating temperature.

2.2 Solid Oxide Fuel Cells

Figure 2.2 shows the basic operation principle of an SOFC with an oxide ion conductor and a proton conducting electrolyte. An SOFC composes two electrodes and an electrolyte between them. In a conventional SOFC, a nickel cermet anode, a perovskite cathode and a dense yttria–stabilized zirconia oxide ion conducting ceramic electrolyte are generally used as components. SOFC operates at 500–1000 °C and can utilise various range of fuel types such as natural gas, methane and other hydrocarbons [43]. In the case of a proton conducting SOFC, hydrogen will be oxidised to produce protons at the anode then protons migrate through the solid electrolyte to react with oxygen and produce water at the cathode.

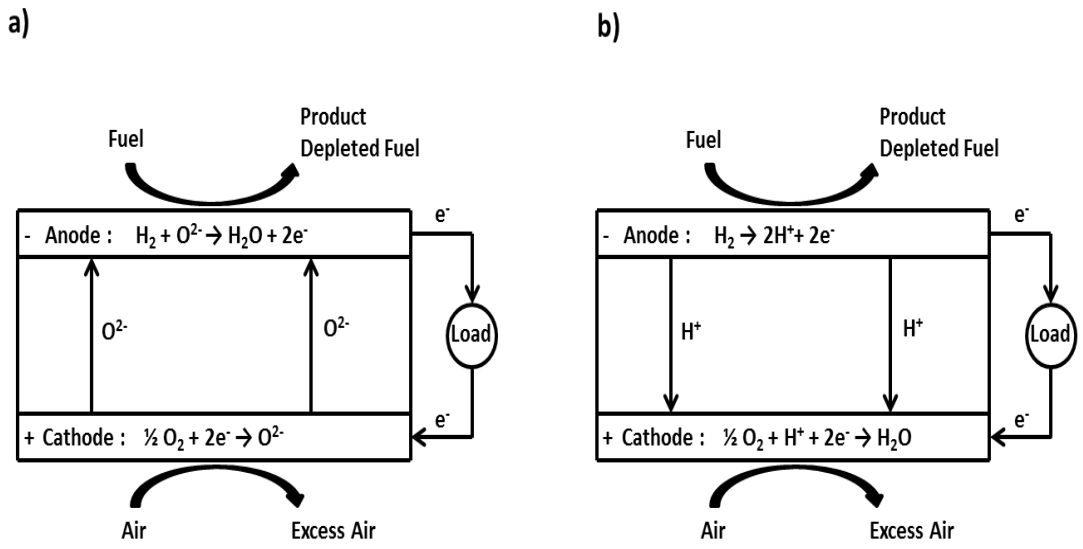

Figure 2.2: Schematic of a solid oxide fuel cell with **a)** oxide ion conducting electrolyte; oxidation of fuel takes place at the anode and reduction of oxygen takes place at the cathode, oxide ions are transported through electrolyte from cathode to anode. Electrons flow through an external circuit from anode to cathode to produce useful power **b)** Proton conducting electrolyte; oxidation of hydrogen takes place at the anode and reduction of hydrogen occurs at the cathode, protons are transported through electrolyte from anode to cathode [43].

The electrochemical reactions can happen at the cathode and anode in an oxide ion conducting SOFC:

$$Cathode: ½\ O_2 + 2e' \rightarrow O^{2-} \qquad 2.1$$

$$Anode: H_2 + O^{2-} \rightarrow H_2O + 2e' \qquad 2.2$$

$$Anode: CO + O^{2-} \rightarrow CO_2 + 2e' \qquad 2.3$$

The overall reaction can be written as follows;

$$H_2 + ½\ O_2\ (+ CO + ½\ O_2) \rightarrow H_2O\ (+CO_2) \qquad 2.4$$

In the case of a proton conducting SOFC, the electrochemical reactions that can take place are;

$$Cathode: \tfrac{1}{2} O_2 + 2H^{\bullet} + 2e' \rightarrow H_2O \quad (2.5)$$

$$Anode: H_2 \rightarrow 2H^{\bullet} + 2e' \quad (2.6)$$

2.2.1 Benefits and Drawbacks

The SOFC technology can provide some advantages such as use of existing fuels (i.e. methane, natural gas) and infrastructure, high conversion efficiency, silent operation, low/zero pollutant emission [43]. An operational SOFC offers about 40%–55% total energy efficiency, however, they can reach up to about 70% total energy efficiency with combined heat and power generation [44]. This is a significant improvement compared to conventional internal combustion engines which offer about 30% total energy efficiency. In vehicles SOFC could be employed as an auxiliary unit to run air conditioning, for this application SOFC could offer useful heat, low emission, use of the same hydrocarbon fuel as the engine compared to existing battery [45]. In terms of stationary application, SOFC can reduce carbon dioxide emission by up to 50% compared to electric generation using pipeline gas. However, there are some disadvantages in terms of application of SOFCs. The SOFCs should have sufficient power density to compete with internal combustion engines and also should have less cost compared to other ways of power generation. The current cost is reported as about $1 500/kW and should be reduced to about $400/kW to be commercially available [44]. Due to requiring long time and more energy to start up compared to existing petrol and electrical vehicles, it is not common in transportation yet [2].

2.3 Thermodynamics and Electrochemistry of SOFCs

2.3.1 Nernst Potential

In a hydrogen fuel cell, n electrons pass through an external circuit, water is produced and hydrogen is used. The charge that passes through the circuit is;

$$-nNe = -nF \ (Coulombs) \qquad 2.7$$

F is the Faraday's constant (96487 Coulombs/mole of electrons), N is Avogadro's number; e is the charge of one electron, n is mole of electrons transferred per mole of hydrogen. The electrochemical work is done [41];

$$W_e = - n_eFE \qquad 2.8$$

E is the reversible open circuit voltage of the cell. If there is no loss in the system, the electrochemical work corresponds to the Gibbs–free energy released (ΔG), which is also defined as the maximum work the cell can produce [41].

$$\Delta G = -n_eFE \qquad 2.9$$

$$E = -\Delta G / n_eF \qquad 2.10$$

Equation 2.10 presents reversible open circuit voltage of the hydrogen fuel cell [1].

The Gibbs energy is defined as below:

$$\Delta G = \Delta H - T\Delta S \qquad 2.11$$

In the case of hydrogen oxidation in solid oxide fuel cells the overall reaction involved is:

$$H_2 + ½O_2 \rightarrow H_2O \quad (2.12)$$

The Gibbs−free energy of this reaction (Equation 2.12) can be written as [46]:

$$\Delta G = \Delta G^{\circ} + RT\ln\frac{P_{H_2O}}{P_{H_2}P_{O_2}^{1/2}} \quad (2.13)$$

Where ΔG° is the standard state Gibbs-free energy at 25 °C and 1 atm, R is the universal gas constant (8.314 J/K mol), T is the temperature in Kelvin (298 K) and P is the partial pressure of the species. ΔG° can be calculated for Equation 2.12 as follows:

$$\Delta G = \Delta G_{products} - \Delta G_{reactants} \quad (2.14)$$

$$\Delta G^{\circ} = G^{0}_{H_2O} - G^{0}_{H_2} - ½\, G^{0}_{O_2} \quad (2.15)$$

At a temperature T, ΔG can be calculated using Equation 2.11 and the Equations below:

$$H_T = H^{0} + \int_{298}^{T} Cp\,dT \quad (2.16)$$

$$S_T = S^{0} + \int_{298}^{T} \frac{Cp}{T}\,dT \quad (2.17)$$

Cp represents the heat capacity of species.

From Equations 2.10 and 2.13 it is possible to calculate the ideal potential of the cell:

$$E = \frac{\Delta G^{0}}{n_e F} - \frac{RT}{n_e F}\ln\frac{P_{H_2O}}{P_{H_2}P_{O_2}^{1/2}} \quad (2.18)$$

The Nernst equation is then:

$$E = E^0 - \frac{RT}{n_e F} ln \frac{P_{H_2O}}{P_{H_2} P_{O_2}^{1/2}} \quad 2.19$$

The electrons transferred in Equation 2.12 is 2, thus, n_e= 2.

$$E = E^0 - \frac{RT}{2F} ln \frac{P_{H_2O}}{P_{H_2} P_{O_2}^{1/2}} \quad 2.20$$

Where E represents the actual voltage of the cell and E^0 represents the standard cell potential.

Equation 2.20 shows that the Nernst equation is influenced by the temperature and reactant concentrations.

2.3.2 Fuel Cell Efficiency

The theoretical efficiency of the fuel cell is determined by the Gibbs free energy, ΔG, and the enthalpy of formation, ΔH. The enthalpy of formation presents the heat obtained from burning the fuel [44].

$$Efficiency = \frac{\Delta G_f}{\Delta H_f} \quad 2.21$$

However, the irreversible voltage losses exist in real applications. The real efficiency of the cell depends on those losses; activation losses, ohmic losses and concentration losses which are described in the following section.

2.3.3 Irreversible Voltage Losses

The theoretical potential of the cell is usually higher than its actual potential owing to three main voltage losses: activation losses, ohmic losses and concentration losses. The regions where these voltage losses are dominant are shown in Figure 2.3.

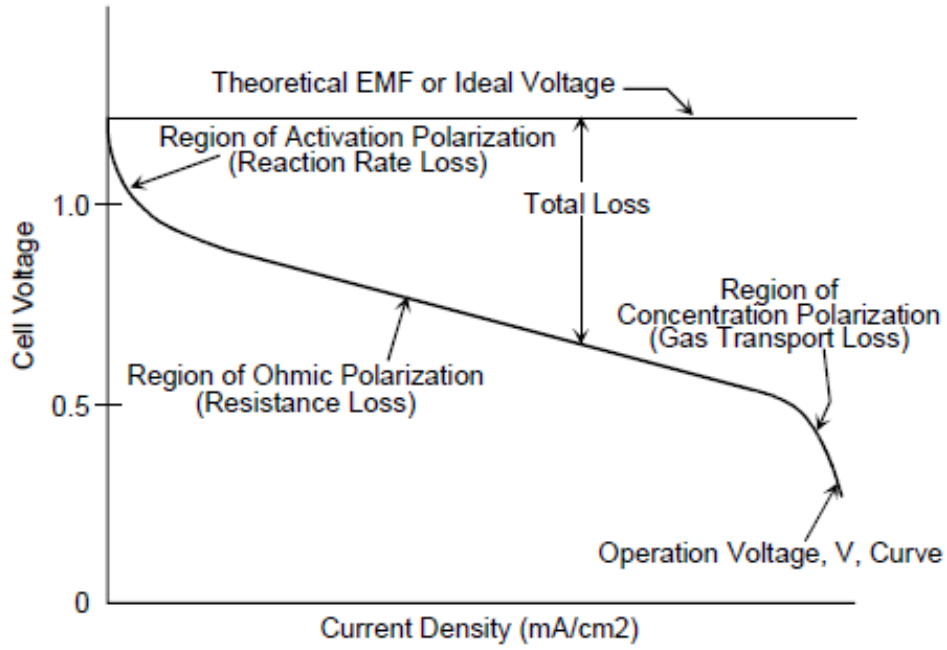

Figure 2.3: The theoretical and actual fuel cell voltages. The activation polarisation voltage losses dominate at low current density region due to slow kinetics of electrode reactions. The ohmic polarisation becomes dominant at the intermediate current density region mainly due to electrolyte resistance to ions. At high current density region, concentration polarisation is present due to mass transport reduction to electrodes [35]

Activation Losses

The reason for the activation over potentials is the slow kinetics of the reactions in both anode and cathode. The activation losses are usually expressed by a semi–empirical Tafel Equation.

$$\eta_{act} = \frac{RT}{\alpha nF}\ ln\ i/i_0 \qquad 2.22$$

α is electron transfer coefficient, R is the ideal gas constant and i_0 represents the exchange current density [35]. Exchange current density is the rate at which the fuel cell reaction is in equilibrium, in which case the net current equals to zero. Activation losses decrease with the increasing reaction kinetics. Thus, high temperature SOFCs have lower activation losses than low or intermediate temperature SOFCs since higher operation temperature increases the reaction rate.

Ohmic Losses

Ohmic losses are caused by the resistance to the electrons through the electrodes and interconnects and to the ions through the electrolyte [1]. The total ohmic resistance of the cell is composed of electronic, ionic and contact resistance of the cell. It is represented by Ohms Law.

$$\eta_{ohm} = iR \qquad 2.23$$

where i represents current and R presents resistance of the electrolytes and electrodes.

The big contribution of the ohmic resistance of the fuel cell comes from the electrolyte of the cell since ionic conduction has higher impact on the ohmic resistance than electronic resistance and contact resistance. Ohmic losses could be decreased by using high conductive electrodes, designing good bipolar plates and interconnects, using appropriate materials, and by making electrolytes thinner [1].

Concentration Losses

The change in the mass transport of the surface electrodes causes concentration losses. The failure to transport enough reactant mass to the electrode surface results in reduction in cell voltage. Concentration polarisation of the cell is expressed by the equation [1]:

$$\eta_{cont} = \frac{RT}{nF}\, ln\,(1 - \frac{i}{i_L}) \qquad 2.24$$

Where R corresponds to ideal gas constant, T represents temperature of the cell, F represents Faraday constant, n represents the number of electrons exchanged, i_L represents limiting current density when the fuel is consumed at its maximum speed and i represents current density of the cell.

Activation losses are slightly smaller than concentration losses for high temperature SOFCs [35].

2.4 Electrolyte Materials for SOFCs

A good solid state electrolyte should have the following features; high ionic conductivity and low electronic conductivity, high chemical stability in oxidising/reducing environment at elevated temperature, thermal expansion compatibility with other cell components and low gas permeability [34]. The electrolyte in SOFCs can carry oxide ion (O^{2-}), proton (H^{+}) or both charges. In this section, both oxide ion conductors and proton conductors will be discussed. Special focus will be given on both oxide ion and proton transport which results in water permeation.

2.4.1 Oxide Ion Conductors

Oxide ion conductors are promising electrolytes owing to their high ionic conductivities and selectivities at high temperatures. A number of oxide ion conductors have been investigated with different structures; fluorite–type (MO_2) (doped bismuth oxide, zirconia, ceria, pyrochlore) perovskite, apatite and related structures (lanthanum gallate, brownmillerites, BiMeVOX) [47]. Yttria stabilised zirconia (YSZ), magnesium–doped lanthanum gallate (LSGM) and gadolinium or samarium–doped ceria (CGO or CSO) have been widely investigated for SOFCs. The conduction mechanism of solid oxide ion conductors is based on creation of oxygen vacancy by doping rare earth metals or metal oxides into the crystal structure. In fluorite oxides, MO_2 where M is a relatively large four-valent cation such as Zr^{4+}, substitution of lower valent cations such as Y^{3+} into the host lattice creates oxygen vacancies to maintain charge neutrality. YSZ is the typical example of this kind of doped-oxide material with fluorite structure (as shown in Figure 2.4), and has good mechanical and electrical properties at high temperatures. It can also show oxide ion conductivity of approximately 0.1 S/cm at 1000 °C [2]. At low temperatures, oxide ion conductivity decreases due to lower mobility and high activation enthalpy of oxygen ions [48]. The maximum conductivity was achieved for YSZ with 8% Y_2O_3 doping [49]. Higher substitution of yttrium into the crystal causes lattice distortion (lattice stress and deviation from cubic symmetry) to the crystal which results in lower ionic conductivity [45, 50].

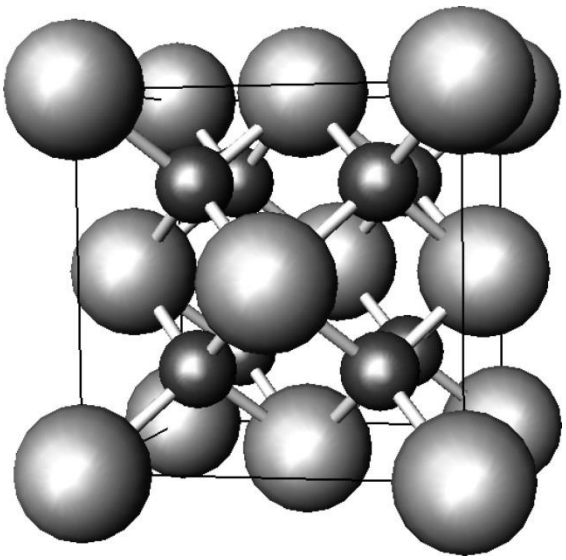

Figure 2.4: Fluorite structure of stabilized zirconia (large sphere; Zr/Ce, small; O) [49].

Each electrolyte has advantages and disadvantages. For instance, LSGM has higher ionic conductivity than YSZ as can be seen from Figure 2.5; however, LSGM is reported to react with Ni in the case of use of a Ni-ceria anode. The reaction between LSGM and Ni results in a highly resistive phases and higher anode polarisation which leads to degradation of the cell performance [51]. The conductivities of major oxide ion conductors are given in Figure 2.5.

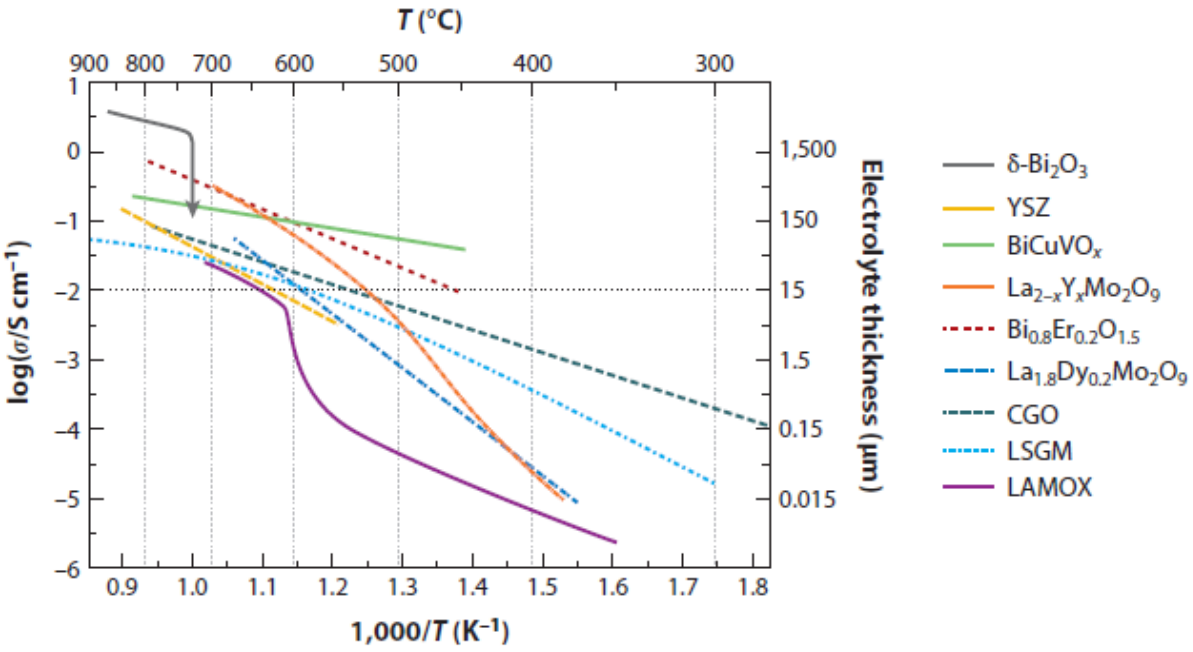

Figure 2.5: Temperature dependence of oxide ion conductivity for major SOFC electrolytes. The horizontal dotted line displays the limit of conductivity to build devices with an electrolyte thickness of 15 micron or less. CGO; $Ce_{1-x}Gd_xO_{2-x/2}$, LAMOX; $La_2Mo_2O_9$, LSGM; $La_{0.8}Sr_{0.2}Ga_{0.8}Mg_{0.2}O_{2.8}$, YSZ; yttria-stabilized zirconia [3].

Besides the fluorite structure, pyrochlore and the perovskite structures have been investigated for oxide ion conductivity. The pyrochlore structure has the formula of $A_2B_2O_7$, for instance, $Gd_2Zr_2O_7$. Doped ceria based electrolytes have higher ionic conductivity than YSZ especially at low temperatures such as 500 °C. However, these electrolytes are relatively unstable at the temperature of above 700 °C. Even though Bi_2O_3 has higher ionic conductivity compared to YSZ, Bi_2O_3 based electrolytes are thermodynamically unstable in reducing atmosphere. They decompose to metallic Bi under reducing atmosphere [52].

Acceptor doping of perovskite aluminates, for example $LnAlO_3$, is one of the attractive materials due to their low cost, moderate thermal expansion and higher stability in reducing atmosphere. The reasons that prevent these materials from becoming commercially viable are poor sinterability, porosity and high grain boundary resistance. These difficulties can be solved by different applications such as addition of aluminium with gallium [52]. The oxygen

ion conductivity of In-, Sc-, Y- doped perovskites is sufficient, however, the application remains in the research scale owing to the high cost [52].

Recent studies include $LaGaO_3$- based perovskites, derivatives of $Bi_4V_2O_{11}$, $La_2Mo_2O_9$, perovskite and brownmillerite like phases, several new pyrochlores such as $(Gd, Ca)_2Ti_2O_{7-\alpha}$ and apatite materials derived from $Ln_{10-x}Si_6O_{26\pm\alpha}$ where Ln is a rare earth cation [52]. These materials show better performance over common ZrO_{2-} and CeO_{2-} based solid electrolytes. In order to reduce the operating temperature of SOFCs, other types electrolyte materials such as proton conductors gained interest.

2.4.2 Proton Conductors

The oxides with perovskite structure (ABO_3) show proton conductivity when they are exposed to hydrogen and/or water rich environment.

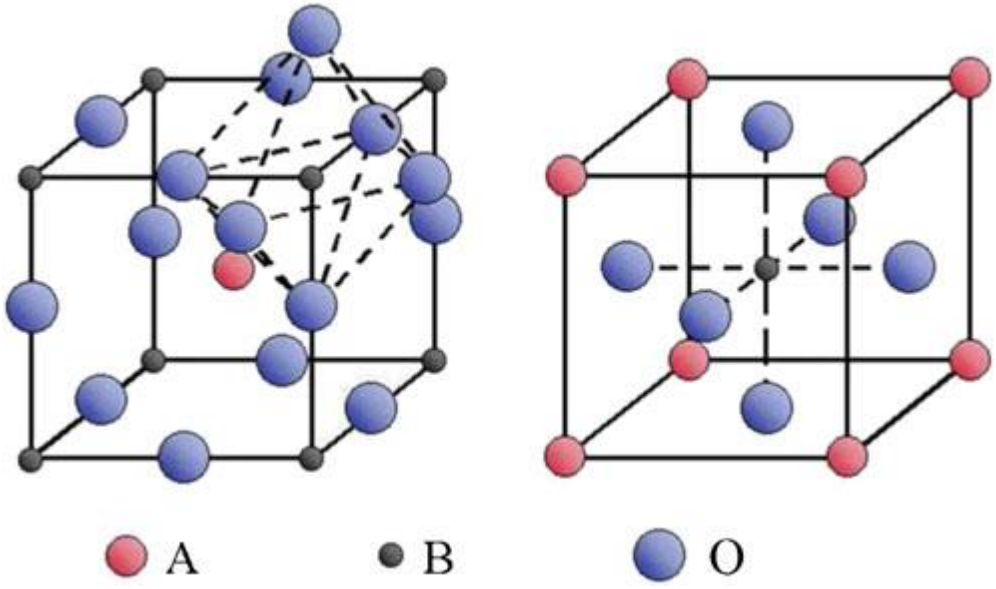

Figure 2.6: Ideal crystal structure of perovskite oxide ABO_3 [53].

The ideal structure of a cubic ABO_3 perovskite is shown in Figure 2.6 in which A and B represents cations. A cation has 12–fold oxygen coordination while B cation has 6–fold

oxygen coordination. The BO_6 octahedra share corners and have 180° B-O-B bonding. The ideal cubic structure can deviate due to the difference between the ionic radii of A, B and O^{2-}. The relationship between radii's is given below.

$$t = \frac{r_A + r_O}{\sqrt{2}(r_B + r_O)} \qquad 2.25$$

Where t represents the tolerance factor (also known as the Goldschmidt tolerance factor) and r_A, r_B , r_O present the ionic radii of A^{n+}, B^{m+}, O^{2-}, respectively.

Perovskite oxide is formed between $0.75 < t < 1.1$. The ideal cubic perovskite structure ($t \approx 1$) has higher oxide ion mobility due to the fact that the oxygen sites have the same energy levels [54]. The deviation creates lower symmetries such as orthorhombic and monoclinic [55]. This can increase activation energy for proton conduction. The ionic conductivity can be improved by doping the A and/or B site with a similar radius cation and lower valence. This leads to less local distortions from the perovskite structure and increases stability.

The generation of oxygen vacancies in perovskite oxides occur by substitution of B- site cation by a lower valent cation. This doping introduces oxygen vacancies to compensate for an acceptor dopant M as shown in the following solid state reaction using Kröger–Vink notation [56]:

$$M_2O_3 \rightarrow 2\delta M_B' + \delta V_o^{\bullet\bullet} + 2(1-\delta)M_A^{\bullet} + (6\text{-}\delta)O_o^x \qquad 2.26$$

Where δ is the effective number of oxygen vacancies generated by doping per unit cell (normally less than 0.2). The dopant atoms generally sit in the B sites, however, it may also sit in A sites as shown in Equation 2.26. The doping of aliovalent cation such as Y^{3+} introduces oxygen vacancies owing to the electrical neutrality condition from a few percent to twenty percent [56, 57] (Aliovalent cations have different valence electrons, i.e. A Y^{3+} ion (ionic radiu, 0.83 Å) replacing a Ce^{4+} (ionic radiu, 0.94 Å) [17]). Further doping can diminish conductivity after reaching the maximum value due to the formation of neutral defect pairs. The doping is generally notated with the initial letters of oxide material following with the one letter abbreviation of the dopant material and the mole percent of the doping material. For

instance, BCY20 ($BaCe_{0.8}Y_{0.2}O_{3-\delta}$) signifies twenty mole percent yttrium doped barium cerate.

The point defects in crystals are described by Kröger–Vink notation as stated below in Table 2.2 [57, 58].

Table 2-2: Kröger-Vink notation for point defects in crystals. MX is chosen as an example compound with M^{2+} as cation and X^{2-} as anion.

Symbol	Type of defect
$V_M^{''}$	Vacant M site with effective -2 charge (with respect to the ideal lattice)
$V_X^{\bullet\bullet}$	Vacant X site : X ion vacancy with effective +2 charge
M_M^x, X_X^x	M , X ion on lattice site, respectively, (neutral)
L_M'	L^+ dopant ion on M site with effective charge -1
$N_M^{\bullet}$	N^{3+} dopant ion on M site with effective charge +1
e'	Free electron in conduction band
$h^{\bullet}$	Free electron hole in valance band
$M_i^{\bullet\bullet}$	Interstitial M ion with effective charge +2
$X_i^{''}$	Interstitial X ion with effective charge -2

The transport of protons occur via formation of $OH_o^{\bullet}$ groups in the perovskite structure. In dry hydrogen atmosphere, this takes place according to Equation 2.27 [59];

$$H_2 + 2O_o^x \leftrightarrow 2OH_o^{\bullet} + 2e' \qquad 2.27$$

The dissociative adsorption of water also leads to formation of $OH_O^{\bullet}$ groups in water rich environment as given in Equation 1.1. Hydrogen dissolves into the oxide as protons and bonds to oxygen ions to form $OH_O^{\bullet}$ groups (substitutional hydroxide). This defect is described as interstitial protons; $H_i^{\bullet}$, and presumed as protonic defects [60]. The protons then hop from one oxygen atom to another in the crystal by diffusing rotationally around the oxygen ion. The attached hydrogen to the oxygen atom may cause reduction of perovskite to elemental metals or binary oxides in Equation 2.27 [61]. Thus, Equation 1.1 is considered to be the most important reaction for formation of $OH_O^{\bullet}$ groups.

Proton conduction was first shown in doped–$SrCeO_3$ ceramics by Iwahara *et al* [62] in 1981. They show the highest proton conduction in hydrogen containing atmosphere at high temperatures by using metal doped $SrCeO_3$ as an electrolyte at 600–1000 °C. They also verified the proton conduction by the voltage behaviour of a hydrogen-oxygen cell. The voltage of the cell increased with decreasing water vapour pressure at the cathode. The water vapour pressure change at the anode influenced the voltage of the cell. In the case of oxygen ion conducting electrolyte, the reverse situation should happen.

Similar studies have been done on $SrCeO_3$, $BaCeO_3$, $BaZrO_3$ based ABO_3 type perovskites by doping a trivalent cation M such as Y, Nd, Sm, Gd and Yb since they displayed protonic conduction under hydrogen containing atmosphere at elevated temperatures [63]. The activation energy required for proton conduction is lower than conventional oxide ion conductors. Moreover, they exhibit both oxygen and proton ion conduction and can be used as solid electrolyte for various purposes such as steam electrolyser, fuel cells and membrane reactor for gas separations.

Recently, they have been investigated for intermediate temperature solid oxide fuel cells since the benefit of water production at the cathode hence the fuel dilution at the anode is avoided [19]. Kreuer and co–workers [15] studied the diffusivity of protonic defects, oxygen ion vacancies and water solubility in single Gd and Y–doped $BaCeO_3$ crystals. The data obtained from conductivity measurements and TGA (Thermo gravimetric analysis) were used to calculate transference numbers and the chemical diffusion coefficient of water. Their results exhibited no strong evidence for the degree of hydration for defect interactions whereas an

increase in the oxygen relaxation around oxygen ion vacancies with decreasing vacancy concentration was found. They suggested the water saturation limit was controlled by the dopant distribution over two cation sites.

Thangadurai and co–workers [55] have recently studied materials for proton conducting solid oxide fuel cells. They looked at the role of A- and B- site cations in the perovskite structures on electrical properties and their chemical stabilities in CO_2, H_2S and H_2O. They prepared Gd+Pr, Sm, Sm+Ca, Eu–doped perovskite type $BaCeO_3$ and some double perovskite–related structure. Their chemical stability results showed that Ce based compounds were unstable in CO_2 at elevated temperature and in H_2O at around 100 °C whereas Nb based sample showed good stability in these environments. Barium zirconate was indicated to be stable in CO_2 environment, however, various conductivity data of the barium zirconate was reported by the research groups from as low as 10^{-6} S/cm to as high as 10^{-2} S/cm at 600 °C as reported by Babilo *et al* [64]. Therefore, due to the highest electrical conductivity for Ce–based perovskites and consistency in the literature with regards to conductivity and transport mechanism, Y–doped barium cerate is chosen in this study.

2.4.3 Y-Doped Barium Cerate (BCY)

Protons were reported as minority charge carriers in 1960s in some oxide ion conductors such as $LaAlO_3$, $LaYO_3$ and $SrZrO_3$. These materials then turn out to be proton conductors in a hydrogen containing atmosphere [14]. Especially $SrCeO_3$ and $BaCeO_3$ related compounds show high protonic conductivity. The first orthorhombic structure of $BaCeO_3$ was determined by Jacobson *et al* [65] at the room temperature which was found to be more stable. Barium cerate exhibits predominantly ionic conductivity at the region of low oxygen partial pressure and mixed ionic–electronic conductivity (hole conductivity) at high oxygen partial pressure region [66]. These materials are very poor hydrogen transport membranes due to lack of electronic conductivity (see Equation 2.27).

Since then these materials have been tested by many researchers using porous platinum or nickel as anode and cathode in various electrochemical cells. The proton conducting oxides can be used as an electrolyte in SOFCs and could reduce the operating temperature in the

range of 500–800 °C. The proton conducting based intermediate temperature solid oxide fuel cells (ITSOFCs) can have higher power output than oxygen ion conducting electrolytes owing to having higher ionic conductivity in these temperature ranges. Their protonic conductivities were reported in the order of 10^{-3} to 10^{-2} S/cm in hydrogen containing environment [63]. Stoichiometric modification of $BaCeO_3$ permits improvement of its properties. Yttrium–doped barium cerate showed the highest conductivity among the other rare–earth metal doped oxides as shown in Figure 2.7 [12, 67]. The conductivity of barium cerate was reported as about 5×10^{-2} S/cm at 700 °C by 20% Y doping in hydrogen containing environment by Iwahara [12]. Similar results (0.049 S/cm) were obtained in wet hydrogen environment in this study using electrochemical impedance spectroscopy. The conductivity measurements were carried out in three different atmospheres and the results are presented in Appendix A. The conductivity of barium cerate increases with Y concentration up to 0.2 [68] which may be due to an increase in charge carrier concentration.

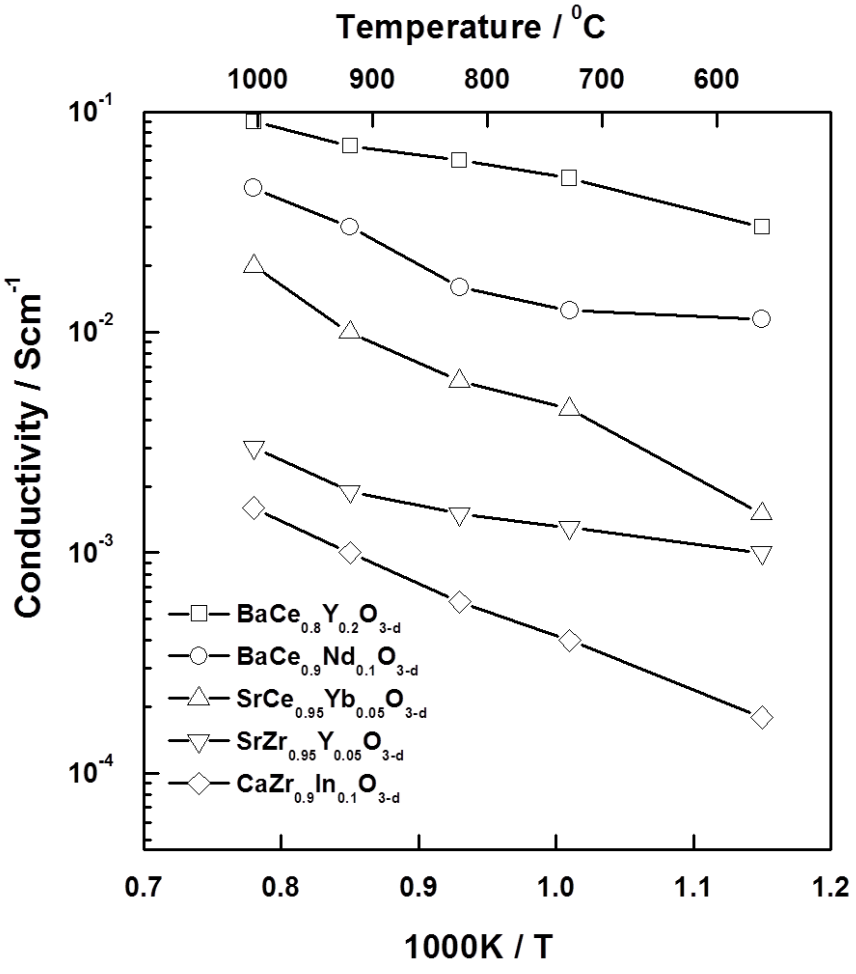

Figure 2.7: The conductivities of major proton conducting perovskites in hydrogen versus temperature [12].

The effect of dopant concentration on conductivity, crystal structure and hydration properties were studied by Takeuchi *et al* [17] and Tauer *et al* [69]. Takeuchi *et al* investigated yttrium doping level of $0 \leq x \leq 0.3$ for $BaCe_{1-x}Y_xO_{3-\delta}$ and reported the maximum total conductivity in the range of $0.15 \leq x \leq 0.25$. Tauer *et al* reported a linear correlation between the dopant concentration and hydration expansion of BCY.

One of the significant properties that can affect proton conduction in these types of ceramics as well as doping level is synthesis method. Several synthesis and sintering methods were studied in order to produce dense ceramic pellets [18, 70-72]. Densification and crystal structure of the material are important parameters for proton conduction. The most common methods used in the field are solid state reaction and sol–gel method. It is possible to obtain dense ceramics with density values of ~95% using both processes. However, solid state reaction procedure requires higher sintering temperature (~1200 °C) than sol gel method (~1000 °C).

BCY20 was also studied to solve carbon deposition problem which is widely seen with the oxide ion conductors. Tomita *et al* [73] studied an SOFC based on BCY20 as an electrolyte and anode without using an anode. A layer was about 10 µm thick created by using heat treatment at 1700 °C to serve as an anode. The heat treatment ensured BaO vaporisation on the membrane surface and creation of Ce rich phase. The heat treated BCY20 cells showed good performance with methane, ethane, propane, and butane. There was no carbon deposition observed. In addition, the cell did not react with CO_2 under CO_2 containing environment, showing that Ce–rich phase acted as a protective layer to CO_2 in the gas mixture due to the fact that a reaction between CeO_2 and CO_2 is not possible thermodynamically.

In addition to the highest conductivity of BCY20, the feature of mixed oxide ion and proton conduction at the intermediate temperatures (500–800 °C) made this material promising for SOFCs due to the fact that both conduction mechanism will result in ambipolar diffusion of protonic defects and oxide ion vacancies [74]. BCY20 membrane can absorb water vapour into oxygen ion vacancies and create interstitial protonic defects in the wet surface by reacting with one oxygen vacant and one occupied oxygen site [75]. The evolution of water can then occur in the dry surface. This water permeation ability makes BCY20 interesting for solid

oxide fuel cells as electrolytes because of the fact that it could be beneficial to overcome the following problems regarding with SOFCs:

Carbon deposition: The use of hydrocarbons as fuel in SOFCs, especially when an anode consists of nickel is used cause large amounts of carbon deposition on the anode surface [76, 77]. The accumulation of carbon blocks the active sites and results in deactivation of anode and degradation in fuel cell performance. For instance, methane will decompose to carbon and hydrogen in the absence of water at a temperature of above 650 °C [1].

$$CH_4 \rightarrow C + 2H_2 \quad \Delta H_{298K} = 75\ kJ/mol \qquad 2.28$$

In addition, high molecular weight hydrocarbons (e.g. propane, butane) tend to crack easier than low molecular weight hydrocarbons (e.g. natural gas). Thus, risk of carbon deposition is high with the liquefied petroleum fuels. Another reason for carbon deposition is carbon monoxide disproportionation reaction, also called Boudouard reaction [5]:

$$2CO \rightarrow C + CO_2 \quad \Delta H_{298K} = -172\ kJ/mol \qquad 2.29$$

Carbon monoxide disproportionation reaction (Equation 2.29) can easily be catalysed by using a nickel containing anode and could be a very fast process. Therefore, carbon deposition will occur within seconds.

The conventional procedures to avoid carbon deposition are pre–reforming of fuel before introduction to the anode or addition of water into fuel. Pre–reforming before introducing the fuel to the fuel cell requires additional unit in order to reform high molecular weight hydrocarbons at low temperatures (250–500°C) which will increase the cost of the system [1]. Furthermore, the ratio of water to carbon should be 2 to 3 to avoid carbon deposition in these systems. This high ratio dilutes the fuel and decreases the power density of the cell [9].

The water permeable ceramic electrolyte could offer another prospect to this problem. The distributed water permeation from cathode through electrolyte to anode could facilitate carbon removal as follows [78, 79]:

$$C + H_2O \rightarrow CO + H_2 \qquad \Delta H_{298K} = 131.3\ kJ/mol \tag{2.30}$$

$$C + 2H_2O \rightarrow CO_2 + 2H_2 \quad \Delta H_{298K} = 90.1\ kJ/mol \tag{2.31}$$

The reactions shown in Equations 2.30 and 2.31 can remove the accumulated carbon from active sites of the anode. Thus, a carbon deposition free internal reforming may be achieved.

Temperature Gradient: In order to avoid carbon deposition, high ratio of water/carbon is used. However, this creates large temperature gradients in the anode due to the fast and endothermic reforming reactions along with dilution of the fuel [78, 80]. The heat produced due to exothermic electrochemical cell reactions is higher than the heat consumed in reforming reaction which introduces the management of temperature gradient in the cell as a problem and requires cooling of the cell. It was also reported [9] that hydrogen coverage is higher because of low use of hydrogen in electrochemical reactions and the current density is lower at the beginning of anode compared to downstream of cell due to temperature drop at this point.

These inhomogeneity's could be eliminated by the introduction of distributed water through the electrolyte. As a result, hydrogen will be consumed as it is produced. That will ensure even distribution of hydrogen (fuel distribution) which will result in distribution of temperature in the cell. Moreover, it will decrease addition of water since product water will also be available to be consumed. Thus, fuel conversion will increase and hence efficiency of the system.

2.5 Water Permeation Mechanism in BCY Membrane

2.5.1 Mechanism of Water Transport

The water is transported through the membrane in the form of protonic defects and oxygen vacancies by a water partial pressure gradient across the membrane. In a region where oxygen partial pressure is low to moderate (where electronic defects can be ignored), the ambipolar transport of protonic defects and oxygen vacancies is possible [81]. The protonic defects ($OH_O^{\bullet}$) are formed when the doped oxide is exposed to water vapour by reacting with an oxygen vacancy ($Vo^{\bullet\bullet}$) and a stationary oxygen site (O_o^x) at this surface [82]. The protonic defects are then free to jump from one oxygen site to another (Grotthuss mechanism) whereas the oxygen vacancies move in the opposite direction as shown in Figure 2.8.

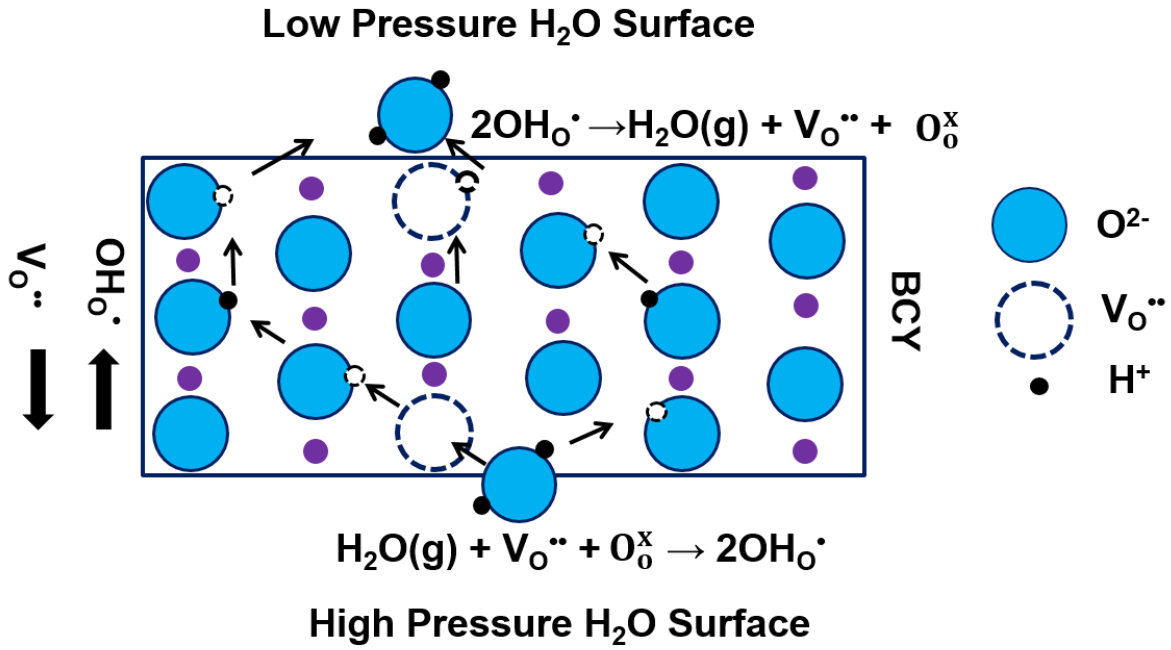

Figure 2.8: Schematic representation of water transport mechanism within BCY membrane. H_2O reacts with one $V_o^{\bullet\bullet}$ and one O_o^x at the high P_{H_2O} surface and forms two hydroxyl groups ($OH_o^{\bullet}$). Then the protons as an interstitial defects hop between hydroxyl groups towards low P_{H_2O} surface as $V_o^{\bullet\bullet}$ diffuses at the opposite direction. At the low P_{H_2O} surface, H_2O is released and $V_o^{\bullet\bullet}$ and O_o^x are formed. No electronic charge carrier is involved.

The reaction equilibrium constant as a function of the concentration of protonic defects and oxygen vacancy and partial pressure of water (P_{H_2O}) for Equation 1.1 is expressed as:

$$K = \frac{C_{OH_O^{\bullet}}^2}{P_{H_2O}\, C_{V_O^{\bullet\bullet}} C_{O_O^x}} \quad 2.32$$

Due to the constant oxygen site (site restriction) in the membrane, electroneutrality condition, and the assumption of the negligible electronic charge carriers in barium cerate the following reactions can be written [14];

$$C_{OH_O^{\bullet}} + C_{V_O^{\bullet\bullet}} + C_{O_O^x} = 3 \quad 2.33$$

From the electroneutrality condition;

$$2C_{V_O^{\bullet\bullet}} + C_{OH_O^{\bullet}} - S = 0 \quad 2.34$$

Where S refers to the effective dopant concentration, $S = C_{Y'_{Ce}} - C_{Y^{\bullet}_{Ba}}$, Y'_{Ce} is the doping level of yttrium on Ce site and $Y^{\bullet}_{Ba}$ is the doping level of yttrium on Ba site.

From Equation 2.33 and 2.34, $C_{V_O^{\bullet\bullet}}$ and $C_{O_O^x}$ can be obtained as a function of protonic defect concentration:

$$C_{V_O^{\bullet\bullet}} = \frac{S - C_{OH_O^{\bullet}}}{2} \quad 2.35$$

$$C_{O_O^x} = \frac{6 - S - C_{OH_O^{\bullet}}}{2} \quad 2.36$$

By substituting Equations 2.33 and 2.34 in Equation 2.32, the concentration of protonic defects can be obtained as a function of P_{H_2O} and K as follows [83]:

$$C_{OH_O^\bullet} = \frac{3K\,P_{H_2O} - \sqrt{K\,P_{H_2O}\,(9K\,P_{H_2O} - 6K\,P_{H_2O}\,S + K\,P_{H_2O}\,S^2 + 24S - 4S^2}}{K\,P_{H_2O} - 4} \quad 2.37$$

The equilibrium constant can be determined by using the theoretically obtained Equation 2.37 with the experimental data obtained from the thermogravimetric analysis [84]. From the thermogravimetric analysis, the concentration of protonic defects at a fixed water vapour and oxygen partial pressure can be obtained from the mass change of sample using the following equation:

$$C_{OH_O^\bullet} = \frac{2M_{sample}}{M_{H_2O}} \frac{\Delta w}{w_{sample}} \quad 2.38$$

Where M_{sample} and M_{H_2O} are the molar mass of the perovskite material and water, respectively, w_{sample} is the mass of the sample and Δw is the mass change of the sample. The change in weight of the sample is measured as a function of time at a fixed water and oxygen partial pressure. When the weight of the sample reaches a stable value by time, the equilibrium is assumed between the sample and gas phase. The weight of the sample at equilibrium at each condition is obtained and used to calculate concentration of protonic defects via Equation 2.38. Similar approach can be applied to determine concentration of oxygen vacancies at a fixed oxygen partial pressure using the thermogravimetric measurements. From Equation 2.32, the equilibrium constant can be found.

The equilibrium constant, *K*, for hydration reaction given in Equation 1.1 can also be calculated from [85]:

$$K = e^{-\left(\frac{\Delta H}{RT} + \frac{\Delta S}{R}\right)} \quad 2.39$$

Where, ΔH and ΔS represents hydration enthalpy and entropy, respectively. Hydration enthalpy and entropy has been obtained by using different experimental techniques (i.e. dilatometry, conductivity, TGA measurements) at various temperatures and doping levels in literature. Those values are discussed in the next section.

2.5.2 Reported Literature Values

The hydration enthalpy and entropy are studied by a few research groups listed in Table 2.3. The hydration enthalpy and entropy of BCY membrane as a function of yttrium doping level (0< x <0.2) was reported by Kreuer *et al* [86]. The hydration enthalpy and entropy that they found were $\Delta H^{0} = -162.2\ kJ/mol$ and $\Delta S^{0} = -166.7\ J/mol\ K$. Their findings suggested that the hydration enthalpy and entropy does not show significant change with temperature and doping level has a weak impact on hydration thermodynamics.

Coors *et al* [20] performed conductivity and dilatometry measurements for $BaCe_{0.9}Y_{0.1}O_{3-\delta}$ (BCY10) at the temperature range of 300–1000 °C. They calculated hydration enthalpy and entropy of BCY10 as $\Delta H^{0} = -156.1\ kJ/mol$ and $\Delta S^{0} = -145.2\ J/mol\ K$ using dilatometry, where the lattice expansion was correlated with respect to a dry sample. They attributed the difference in data with Kreuer *et al* [86] to thermogravimetric analysis where weight gain is used to determine hydration thermodynamics and water entrance into the pores may result in overestimation of data. A few years later, Ricote *et al* [87] reported a hydration enthalpy of $-123\ kJ/mol$ and entropy of $-113\ J/mol\ K$ for BCY10.

More recently, Kjolseth *et al* [22] also studied the hydration enthalpy of $BaZr_{0.9}Y_{0.1}O_{3-\delta}$ (BZY10) at the temperature range of 300–900 °C and BCY10 at 600 °C. The authors reported standard hydration enthalpies as $\Delta H^{0} = -81 \pm 4\ kJ/mol$ for BZY10 and $\Delta H^{0} = -170 \pm 6\ kJ/mol$ for BCY10 and concluded that hydration enthalpies of samples are independent of temperature which is in agreement with Kreuer`s findings.

The data for entropy of hydration is in line with Norby`s baseline [88] where it is given as $\Delta H^{0} = -120 \pm 40\, J/mol\, K$, however, there are still some discrepancies in the values. It was suggested by Yamazaki *et al* [89] that the scatter in data might be due to barium deficiency over A and B sites or oxygen incorporation. Norby *et al* [88] also investigated about 40 perovskite systems to identify any relation between hydration enthalpy and entropy, however they could not find any relation between them.

The differences in values for hydration enthalpy and entropy between Kreuer *et al* [86] and Ricote *et al* [87] as given in Table 2.3 can be due to doping level and/or cerium content. Yttrium may sit on both A and B sites, however, only B sites doping contributes oxygen vacancy formation and so thus hydration of the sample. In addition doping level has an effect on conductivity measurements (e.g. affects proton mobility). Therefore, the effective doping level can effect hydration thermodynamics which are usually determined by doing conductivity and hydration measurements. This implies that sample preparation, density of the sample and experimental conditions have an influence on reported values.

Table 2-3: Summary of experimental results for hydration thermodynamics of BCY10 and BZY10.

Authors	Material	$\Delta H^{0}\ kJ/mol$	$\Delta S^{0}\ J/mol.K$
Kreuer *et al* (1999) [86]	BCY10	-162.2	-166.7
Coors *et al* (2005) [20]	BCY10	-156.1	-145.2
Ricote *et al* (2009) [87]	BCY10	-123	-113
Kjolseth *et al* (2010) [22]	BCY10	-170	–
Kreuer *et al* (1999) [86]	BZY10	-75.7	-86.2
Schober *et al* (2000) [90]	BZY10	-74.2	-86.8
Kjolseth *et al* (2010) [22]	BZY10	-81	–

The diffusion coefficients of species within these materials were mostly obtained by the means of conductivity measurements in literature. The total conductivity is measured with various water contents under an electrical driving force. The contribution of oxygen ion

vacancies is determined as a function of water content and subtracted from the total conductivity. The diffusion coefficient of protonic defect is then calculated from the remaining conductivity on the water content. Oishi *et al* [91] measured the mobility of each defect species from electrical conductivity and calculated the diffusion coefficients using the Nernst–Einstein equation which relates partial conductivity of species to mobility of species and then diffusion coefficients. The diffusion coefficients of defects were reported for BCY10 at 700 °C by a few researchers. Kreuer *et al* [92] reported the diffusion coefficient of oxygen vacancy as $D_{V_o^{\bullet\bullet}} = 5 \times 10^{-5} cm^2/s$, Coors *et al* [20] used AC impedance spectroscopy and found the values of $D_{V_o^{\bullet\bullet}} = 5 \times 10^{-6} cm^2/s$ and $D_{OH_o^{\bullet}} = 1.7 \times 10^{-6} cm^2/s$, Oishi *et al* [91] reported those values as $D_{V_o^{\bullet\bullet}} = 8 \times 10^{-6} cm^2/s$ and $D_{OH_o^{\bullet}} = 1 \times 10^{-5} cm^2/s$ and Grimaud *et al* [93] reported the diffusion coefficient of oxygen vacancy as $D_{V_o^{\bullet\bullet}} = 6.6 \times 10^{-6} cm^2/s$.

All the techniques that were used in those measurements have their own limitations. A TGA technique involves measuring the weight change of a sample upon exposure to a humid atmosphere which may result in overestimation of data due to water entrance into pores of the sample. Another method is AC conductivity measurement which is an indirect method and requires correlation of conductivity data with equivalent circuits. In most cases, the data of the material is not ideal and requires appropriate data fitting techniques [56]. This correlation reduces the reliability of data and brings difficulties on data interpretation. On the other hand, DC conductivity measurements are unable to distinguish between bulk and grain boundary conductivity since only total conductivity can be measured.

Apart from electrical conductivity measurements, Secondary Ion Mass Spectroscopy (SIMS) was also employed to measure diffusion coefficients of species in literature. In this technique, the sample is exposed to an atmosphere which contains isotopes of diffusing species for a certain time. Then the sample is removed and bombarded with ion beam which creates secondary ion flux emitted from the surface or near the surface of the sample [94]. This is then fed to the mass spectrometer. The ratios of isotopes are recorded while the ion beam penetrates into the sample from which the depth profile can be obtained. By correlating sample exposure time with isotopic ratio and using Fick`s second diffusion law, the coefficients of species can be obtained [95]. However, this is a very expensive technique and not available in most research laboratories.

We move the research beyond determination of hydration properties of materials and conductivity measurements, and further investigate water permeation capabilities of disc shaped membranes for practical membrane applications by studying the effects of presence of electrodes (surface treatments –surface reactions) on either side (feed or permeate) and on both sides of the membrane on water permeation over the temperature range of 500–800 °C which has not been investigated so far. In addition, the diffusion coefficients of defects are determined by applying a different method from literature which is cheaper and an effective way for providing in–situ and real time data. Also, the feasibility of using permeated water for reforming of fuels as well as the possibility of solving problems regarding with internal reforming is studied. Moreover, operations of fuel cells with various fuels (i.e. hydrogen, carbon monoxide, and methane) with simultaneous water permeation are carried out.

2.5.3 Modelling

The chemical diffusion coefficient of water was derived by Kreuer *et al* [82], based on the assumption that ambipolar diffusion of protonic defects and oxygen vacancies and ignoring the volume change during water absorption as follows (see derivation in Appendix B);

$$\widetilde{D}_{H_2O} = \frac{(2-X)D_{OH_O^\bullet}D_{V_O^{\bullet\bullet}}}{XD_{OH_O^\bullet}+2(1-X)D_{V_O^{\bullet\bullet}}} \qquad 2.40$$

Where $D_{OH_O^\bullet}$ and $D_{V_O^{\bullet\bullet}}$ are the diffusion coefficient of protonic defects and oxygen vacancies and X represents the degree of hydration which is defined as the fraction of oxygen vacancies in the dry state filled by OH^- groups.

The chemical diffusion coefficient of water can be obtained using the equation above under some conditions such as small oxygen vacancy concentration and no defect interactions. In humidified oxygen environment such as in fuel cells, the model may not be valid since incorporation of oxygen may compete with water dissolution reaction and ambipolar diffusion may not exist under these conditions.

Coors [81] produced an equation for the molar flux of permeated water by using Fick`s first law for steady state diffusion, assuming that the molar flux of permeated water depends on membrane thickness.

$$J_{H_2O} = -\widetilde{D}_{H_2O} \nabla C_{H_2O} \qquad 2.41$$

By using the relationship between concentration and the chemical diffusion coefficient of water and integrating the equation across the membrane thickness the following equation can be written;

$$J_{H_2O} = -\frac{1}{\Delta x} \int_{C_I}^{C_{II}} \widetilde{D}_{H_2O}(C) dC \qquad 2.42$$

Where Δx is the membrane thickness, I and II represent wet and dry surfaces of the membrane, respectively.

By inserting the expression for $\widetilde{D}_{H_2O}$ into Equation 2.42:

$$J_{H_2O} = -\frac{D_{OH_o^\bullet} D_{V_o^{\bullet\bullet}}}{\Delta x} \int_{C_I}^{C_{II}} \frac{(\gamma - C) dC}{ac + b} \qquad 2.43$$

The final solution can be obtained by integration as follows:

$$J_{H_2O} = \frac{D_{OH_o^\bullet} D_{V_o^{\bullet\bullet}}}{\Delta x \, (D_{OH_o^\bullet} - 2D_{V_o^{\bullet\bullet}})} \left[(C_{II} - C_I) + \left(\frac{b}{a} + \gamma\right) ln\left[\frac{(aC_I + b)}{(bC_{II} + b)}\right]\right] \qquad 2.44$$

Where, $\gamma = 2[Y'_{Ce}]$, $a = (D_{OH_o^\bullet} - 2D_{V_o^{\bullet\bullet}})$ and $c = 2D_{V_o^{\bullet\bullet}}$.

Equation 2.44 shows that the water flux is inversely proportional to membrane thickness. Therefore water permeation experiments are conducted in this study for different bare BCY20 membrane thicknesses to verify this hypothesis. It was observed that as the membrane thickness increases, water permeation decreases (see appendix C) which indicates that bulk diffusion reduces the overall water permeation for thicker membranes.

2.6 Summary

The demand for clean energy production from fuel cells require solving problems associated with existing materials or implementing new materials. Based on all the reviews in this chapter, oxide ion conducting SOFC electrolytes especially YSZ has limitations in terms of becoming commercially viable. Efforts have been made to overcome those limitations, however, that increased the price of the system. Doped barium cerates have been shown as good proton conductors and considered to be good electrolyte materials for SOFCs. Doping with lower valent cation creates oxygen vacancies to satisfy electro neutrality condition which allows this material to be able to permeate water from high water partial pressure surface to low water partial pressure surface. By using barium cerate as an electrolyte with given electrode materials, this specific feature of the material may be applied to overcome previously mentioned limitations with internal reforming. There are some work based on barium cerates to clarify its conductivity, however, no comprehensive work has been done to investigate this material as a water permeator and an electrolyte in SOFCs. Furthermore, a detailed study of stability and durability of barium cerate under reducing and oxidising conditions will be carried out by post operation analysis.

Chapter 3
Methodology

This chapter describes the material preparation and methods used for the membrane based experiments in addition to the experimental set up. The details of membrane fabrication, the experimental set up, the surface modification and the list of experiments are given in *Section 3.1*. The analysis system used in the experiments to collect data is also described in *Section 3.1*. The characterisation techniques used to identify the crystal structure and the morphology of the membrane before and after the experiments are detailed in *Section 3.2*. The investigation of high temperature membrane sealants, a curial step to be able to perform membrane based experiments in the laboratory was carried out systematically in *Section 3.3*.

3. 1 Experimental

3.1.1 Membrane Preparation

The electrolyte pellets were prepared uniaxially by pressing approximately 2.2 g of BCY20 and BCY10 powders at 3 tons using a 20 mm diameter die. The final green discs were approximately 2 mm thick and after a sintering program the final diameter and thickness were approximately 1.4–1.6 mm. The pellets were sintered by following the program below under ambient air.

1 Ramp to 1450 °C at a rate of 1 °C/min

2 Dwell at 1450 °C for 12 hrs

3 Ramp to room temperature at a rate of 1 °C/min

The sintering temperature of the membrane is chosen high in order to get a dense and uniform structure. The geometric dimension and mass of the pellets were used to estimate the density. The relative density of BCY pellet was more than 95% of the theoretical density (6.154 g/cm^3 [72]). After the sintering process, the pellets (solid electrolytes) were polished using a SiC sand paper with a grit of 600, washed with deionised water. The mass of sample was measured after drying the sample.

3.1.2 Experimental Set up

3.1.2.1 Membrane Reactor

A two–chamber reactor design with two gas compartments, i.e. feed side (water introduced) and permeate side (water permeated), was used in this study as shown in Figure 3.1a. The membranes were bonded to an alumina tube with 8 mm ID and 12 mm OD. The gas tightness of the membranes was ensured by using the prepared ceramic sealants around the alumina tube and the membrane as described in *Section 3.3*. This alumina tube was then placed in a quartz tube as shown in Figure 3.1a. The volume of this quartz reactor was about 50 cm^3. O–rings (Viton) were used between the tubes and the Swagelok fittings to prevent gas leak. The final reactor was inserted into a tube furnace vertically (Vecstar Furnaces, UK). The temperature of the reactor during the experiments was controlled by using a digital thermometer (Kane–May KM340) connected to a K–type thermocouple. The reactor module shown in Figure 3.1b was modified slightly for the polarisation/fuel cell experiments. The electrode connections were enabled to the Ivium potentiostat/galvanostat by the gold wires purchased from Alfa Aesar and insulated by using a one bore and two bores alumina tubes. A gold mesh (Pi–kem) was used as a current collector connected to the working and the counter electrodes.

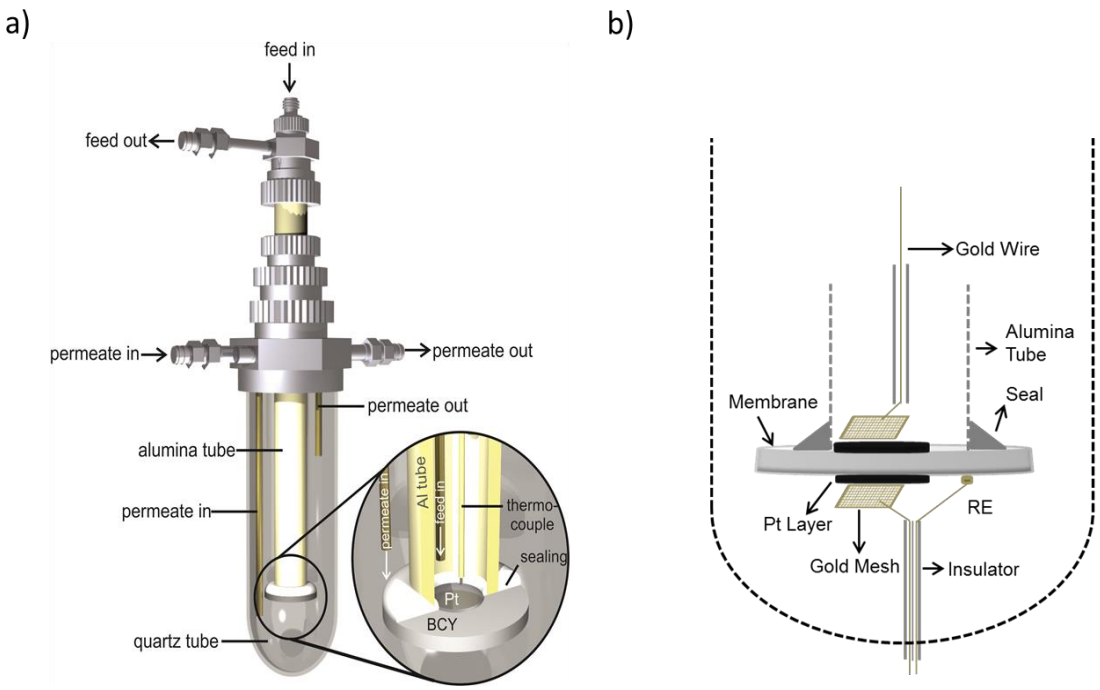

Figure 3.1: Schematic of the dual chamber membrane reactor **a)** Membrane based permeation/reaction experiments; a two–chamber reactor design with two gas compartments, i.e. feed side (water introduced) and permeate side (water permeated) was used. The membranes were bonded to an alumina tube. The gas tightness of the membranes was ensured by using the prepared ceramic sealants around the alumina tube and the membrane. This alumina tube was then placed in a quartz tube. **b)** Reactor design for fuel cell/polarisation experiments; platinum was painted on both sides of the sintered membrane covering an area of 0.5 cm^2 as cathode and anode and platinum was also painted as a reference electrode with an area of 0.05 cm^2. Gold mesh connecting with a gold wire was attached to each side of the membrane as a current collector.

3.1.2.2 Experimental Rigs

The schematics of the experimental rigs used in this study are shown in Figure 3.2a and Figure 3.2b. The stainless steel tubing was used for heated lines and Perfluoroalkoxy (PFA) tubing was used for the other gas connections in the rigs. The flow rates of gases were controlled by the Chell Hastings electronic mass flow controllers (MFCs). The flow rates of gases were also checked at the outlet using a Varian digital flow meter (1000 series). Water level was controlled with a Grant Instrument (Grant Scientific, UK) water bath. The

concentration of water leaving the water bath was controlled by changing the water bath temperature. Three percent water concentration was obtained at about 25 °C of water bath temperature. The inlet tubes were heated to 80 °C by wrapping the lines with heated tapes in order to avoid water condensation and a Cole–Parmer CRS moisture trap was used to capture the moisture in the permeate side stream before the membrane reactor. The total flow rates of the feed and permeate gas streams were 100 ml (STP)/min. All the experiments were performed under atmospheric pressure. The gases were analysed using two dew point hygrometers (Vaisala HMT330, Finland) and a mass spectrometer (Thermostar TM, Pfeiffer Vacuum).

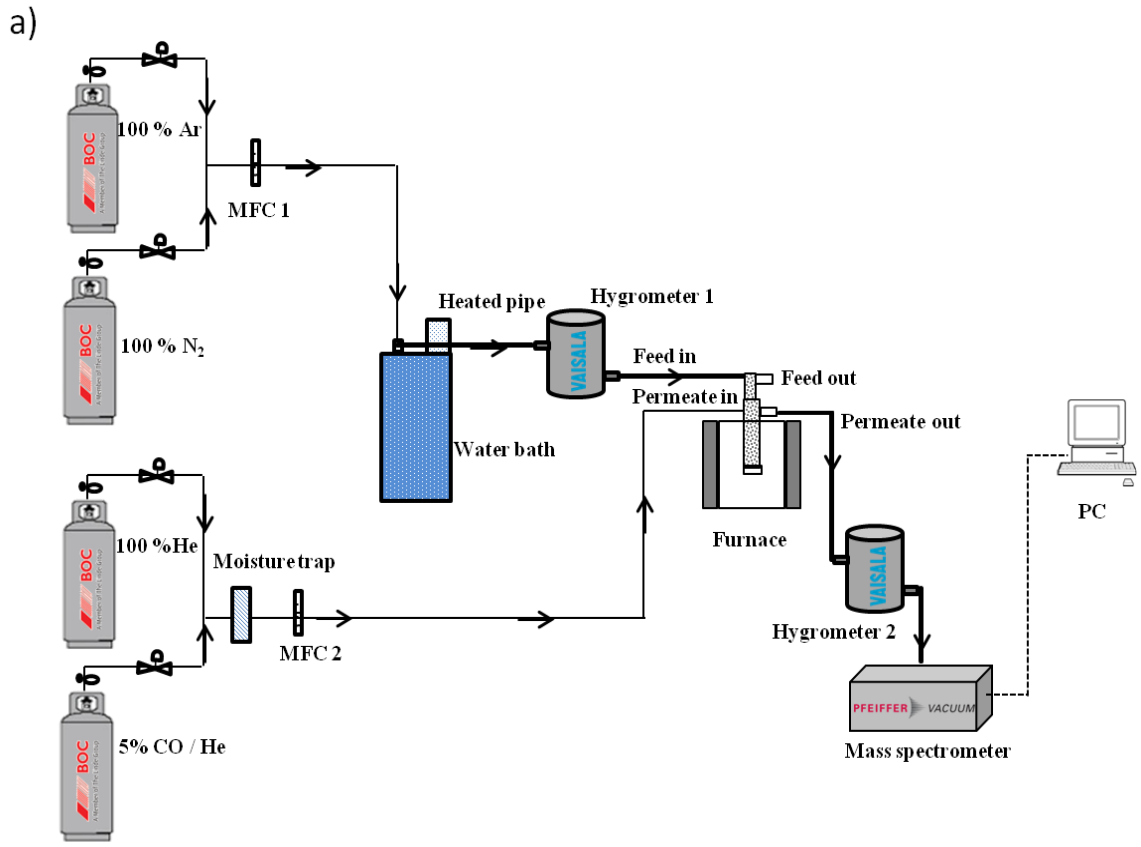

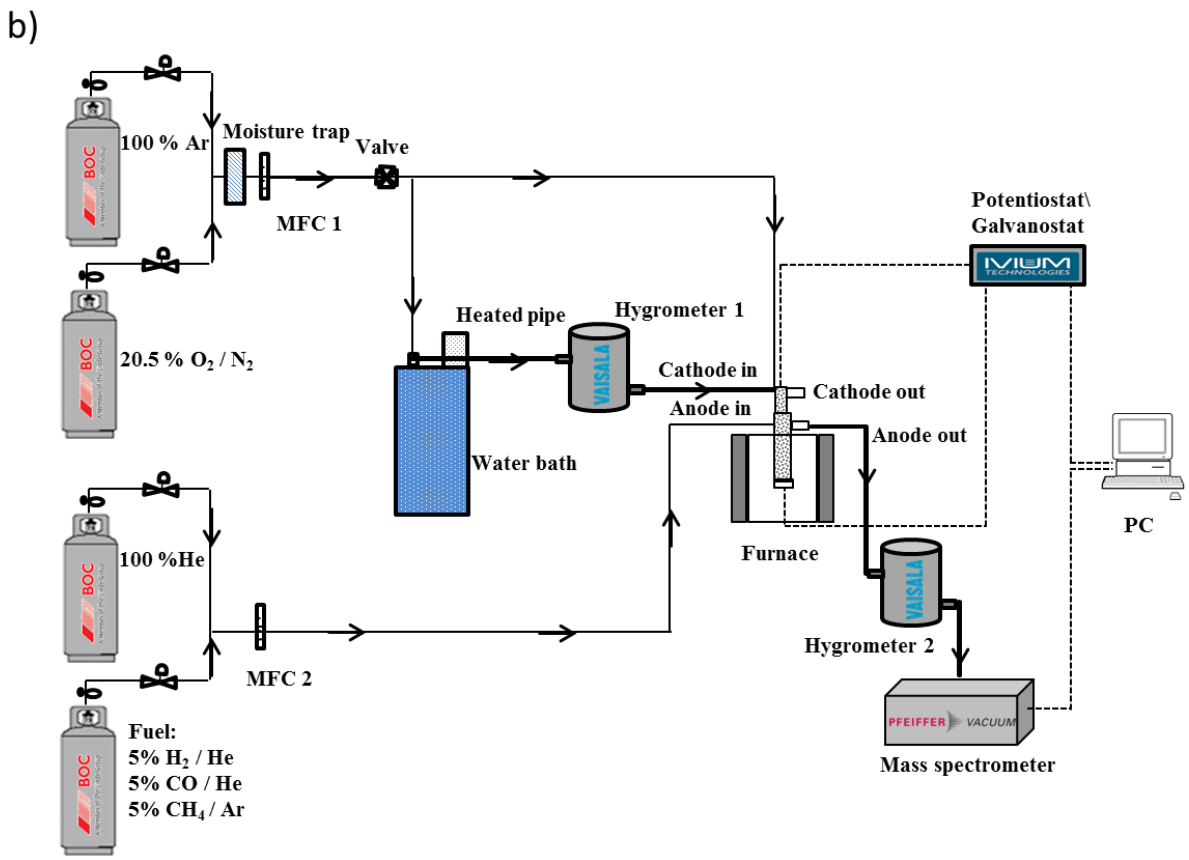

Figure 3.2: Detailed schematics of the experimental rigs compose of gas supplies, feed control, water saturator, furnace, membrane reactor, gas analysis and PC control for **a)** Permeation/reaction experiments, **b)** Fuel cell/ polarisation experiments.

3.1.3 Catalytic Membrane Surface Modification for Water Permeation and Water Gas Shift Reaction Experiments

Platinum resin obtained from ESL Europe (type 5542–print grade) was applied onto the membrane surface in different configurations using a small fine brush. The membranes were then heated up using a programmed temperature ramp of 20 °C min^{-1} to 980 °C, held for 10 min, then 20 °C min^{-1} to 25 °C to sinter platinum metal onto the membrane surface. The four different membrane configurations were prepared for water permeation and water gas shift reaction as without any platinum, platinum on both sides, platinum is only on the permeate side and platinum is only on the feed side as shown in Figure 3.3.

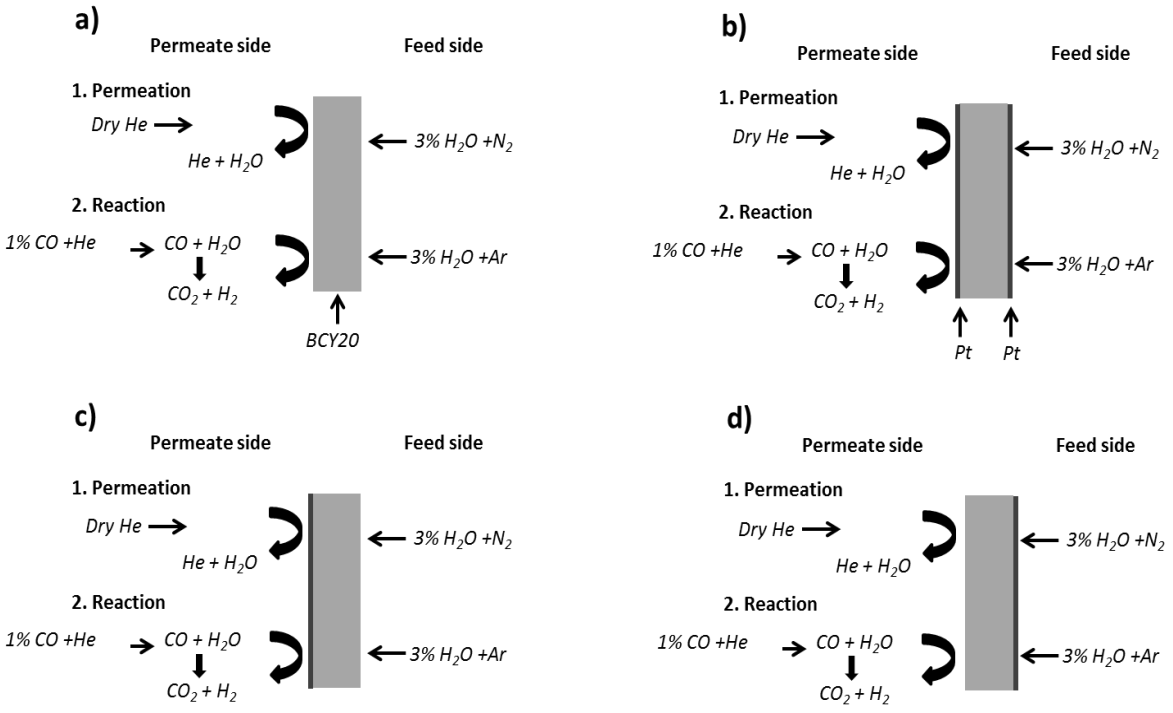

Figure 3.3: Catalytically modified and unmodified membrane systems for water permeation and water gas shift reaction experiments **a)** without any platinum, **b)** platinum is applied on both sides, **c)** platinum is applied only on the permeate side, **d)** platinum is applied only on the feed side (Platinum surfaces are sintered at 980 °C for 10 min) The compositions of feed gases to both sides of the membrane and associated permeation and reactions are also shown.

3.1.4 List of Experiments

a) Hydration Experiment for the Model

The commercial BCY20 powder was purchased from Marion Technology (France) and was used to prepare BCY20 membrane. BCY10 powder was prepared via solid state method using $BaCO_3$ (99%, Aldrich), CeO_2 (99%, Aldrich), and Y_2O_3 (99%, Aldrich). The precursors were mixed in an appropriate ratio and ground with ethanol. The mix was ball milled for 4 hrs and then calcined at 1300 °C for 10 hrs. Both membranes were prepared by uniaxial pressing of 2 g of BCY powder at 3 tons using a 20 mm diameter die and were sintered at 1450 °C for 12

hrs. The formation of perovskite structure was confirmed by XRD and the morphology of the membranes were analysed by SEM (See Appendix D for BCY10 results). The final discs were 1.44 mm and 1.14 mm thick. Platinum resin obtained from ESL Europe (type 5542–print grade) was applied onto the exposed membrane surfaces. The platinum resin was diluted with an appropriate solvent in order to get a thin and porous layer before application. A very small area of platinum (<0.05 cm^2) was also applied in the middle of the membrane on the isolated side to ensure a good electrical connection with the membrane surface for potential measurements. The electrical connections were done using gold wires. The isolated side of the membrane was covered both with a ceramic sealant and Sm–doped CeO_2 (SDC, which is inert to water permeation) to get a hydrophobic surface and isolate this surface from the surrounding atmosphere. A schematic representation of the membrane set up is shown in Figure.3. 4.

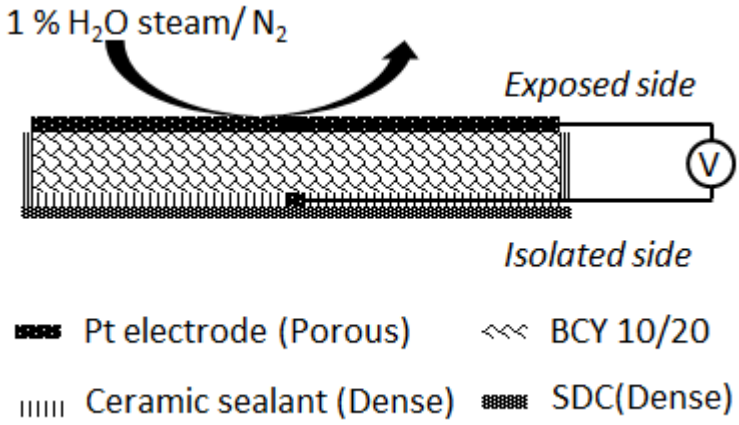

Figure 3.4: Schematic representation of the BCY membrane to measure electrical potential difference during hydration and dehydration of the membrane at 700 °C in a single chamber reactor. One side of the membrane surface is sealed by using both a hydrophobic dense membrane and a ceramic sealant to isolate this surface from the surrounding atmosphere. A thin platinum layer is applied on the exposed surface. The electrical connections are ensured by using gold wires. The flow rates of feed gases are 200 ml/min. The reactor chamber is fed with dry helium for 24 hrs to minimise water concentration in the solid oxide before the measurement, then the gas is switched to 1% H_2O in nitrogen. The reactor is fed with 1% H_2O in nitrogen during hydration process and fed with dry helium during dehydration process.

The potential measurements were done by using an electrochemical workstation in a single chamber reactor at 700 °C and at atmospheric pressure. The reactor was fed with 1% H_2O in nitrogen during hydration process and with dry helium during dehydration process. The total flow rates of gases were 200 ml/min. The reactor was fed with dry helium for 24 hrs to minimise water concentration in the solid membrane before the measurement, then the gas was switched to 1% H_2O in nitrogen. Water level was controlled with a Grant Instrument water bath by varying the temperature and the inlet tubes were heated by wrapping the lines with heated tapes in order to avoid water condensation in line during hydration process. A moisture trap was used to ensure that helium gas was dry before entering the reactor. A blank experiment was performed with an Al_2O_3 membrane following the same experimental procedure in order to verify electrical potential changes of BCY membranes.

b) Water Permeation Experiments

Water permeation experiments were conducted with 1mm thick membranes with and without catalytic surface modification shown in Figure 3.3 in the temperature range of 500–800 °C. Dry helium (BOC, UK) was fed to the permeate side as sweep gas and 3% H_2O in nitrogen (BOC, UK) was fed to the feed side of the membrane reactor. The total flow rates of the feed and permeate gas streams were 100 ml (STP)/min. Water level in the feed stream was controlled with the Grant Instrument water bath. The permeate side outlet stream water mole fraction and feed side inlet stream water mole fraction were monitored by using dew point Vaisala hygrometers, hygrometer 1 and hygrometer 2, as shown in Figure 3.2a. The water permeation fluxes as a function of temperature were measured. Measurements were taken at each temperature after the steam flux reached a stable value. The water on the feed side was kept as 3% for all membranes.

In order to make sure that the hygrometer works efficiently and calculate any possible deviation in readings, the reading of hygrometer was compared to the theoretical value of water vapour at a specific temperature and associated error in readings of hygrometers is calculated as follows:

$$\%Error = \frac{|T_v - E_v|}{T_v} \times 100\% \quad 3.1$$

Where, T_v is the theoretical value of water vapour concentration and E_v is the experimental value of water vapour concentration at a specific temperature. The calculated error percentage for hygrometers is maximum 3% of readings (See Appendix E).

The mass spectrometer was connected to the permeate side hygrometer (hygrometer 2) to check any possible leak from feed side to permeate side. The nitrogen leak (feed) to the helium side (permeate) was monitored by the mass spectrometer during the experiments. Before every experiment, a leak test was performed at the operating temperature and any possible leak was monitored during the experiments. If there was any leak, the data was corrected as shown in Equation 3.2. It was assumed that the amount of water leaking to the permeate side is similar to the amount of nitrogen leaking to the permeate side. The molar flux of water, J_x, is determined by using the mole fractions (x), on the feed and permeate side as follows:

$$J_x = [x]_{out} F \frac{1}{V_m} \frac{1}{60} \frac{1}{SA} \quad 3.2$$

where $[x]_{out} = x(H_2O)perm - x\ (N_2)perm \frac{x(H_2O)feed}{x(N_2)feed}$ with $x(H_2O)perm$ is the water mole fraction and $x\ (N_2)perm$ is the nitrogen mole fraction on the permeate side. $x(H_2O)feed$ is the mole fraction of water and $x(N_2)feed$ is the mole fraction of nitrogen on the feed side. F is the flow rate of the feed gas on the permeate side in ml (STP)/min, V_m is the molar volume (1 mole equals to 22,400 ml at STP), the 1/60 factor is to convert the rate from minutes to seconds and finally SA designates the flux area, cm^2 (the active area of the membrane surface which was exposed to water).

c) Membrane Based Water–Gas Shift Reaction Coupled with Water Permeation Experiments

Membrane based water–gas shift experiments coupled with water permeation were conducted using the membrane configurations in Figure 3.3 (*Section 3.1.3*) and the experimental set up illustrated in Figure 3.2a (*Section 3.1.2*) with a 1.2 mm thick membranes. The membrane module was placed inside the furnace which was used to heat the membranes to 900 °C with a heating rate of 1 °C/min and then hold for 30 min so as to soften the sealant. The temperature then was decreased to the operating temperature of 700 °C with ramp of 1 °C/min. Every heating up and cooling down process was performed by using helium and argon at a flow rate of 20 ml (STP)/min to protect both catalysts from undergoing any oxidation reaction.

The membrane reactor consists of two gas compartments which were separated by the BCY20 membrane; feed side and permeation side. The outlet of the permeate side was monitored by using one of the hygrometer and the mass spectrometer. The second hygrometer was used to monitor water inlet on the feed side. The leak rate was followed by checking the argon level on the permeate side. All experiments were carried out at a fixed temperature of 700 °C under atmospheric pressure on both sides of the membrane.

The membrane based water gas shift experiments coupled with water permeation experiments were carried out in three steps as shown in table 3.1. Each step was given the time period to reach a steady state mole fraction of outlet gases on the permeate side (the change in mole fraction less than 10 ppm per minute in the outlet gases on the permeate side). In step one, dry helium and dry argon were supplied to feed and permeate side of the membrane, respectively. In step two, feed side stream was switched to 3% H_2O in argon. In step three, 1% carbon monoxide in helium was introduced to (5% carbon monoxide in helium was diluted with helium to obtain about 1% carbon monoxide in helium) to the permeate side. The gases were supplied at a total flow rate of 100 ml (STP)/min.

Table 3-1: Experimental procedure for membrane based water–gas shift experiments coupled with water permeation.

	Step One	Step Two	Step Three
Permeate side stream composition	dry He	dry He	1% CO in He
Feed side stream composition	dry Ar	3% H_2O in Ar	3% H_2O in Ar

Additional experiments were also performed at the temperature of 25 °C and 700 °C to evaluate the influence of diluting 5% carbon monoxide to 1% carbon monoxide in helium and find best flow rates and operating procedure (i.e. manual valve switching) to mix the gases.

The mole fractions of outlet gases (x) are converted into the rate of product formation (nmol/cm^{2}s) by using the flow rates of gases and active membrane surface area (see Equation 3.3). It should be noted that there could be a contribution to carbon dioxide production significantly due to a reaction between the reducing gas (carbon monoxide) and sealant/membrane or carbon monoxide disproportionation. Thus, for a realistic calculation of carbon dioxide production from water gas shift reaction, these contributions should be subtracted. In order to determine this contribution to carbon dioxide rate (y), immediately after step three, 3% H_2O in argon was switched to argon in the feed side during all experiments and the obtained average carbon dioxide mole fraction was subtracted from the mole fraction of carbon dioxide in step three in order to calculate the rate of carbon dioxide formation due to water permeation coupled with water–gas shift reaction. After that these values were subtracted from the mole fractions of products in step three the rate of products was calculated using Equation 3.3 where F is the flow rate of the feed gas on the permeate side in ml (STP)/min, V_m is the molar volume (1 mole equals to 22,400 ml at STP), the 1/60 factor is to convert the rate from minutes to seconds and finally SA designates the flux area, cm^2 (see Appendix F). The mole fractions of permeate side outlet gases were recorded with the mass spectrometer. The maximum and minimum error associated with readings of mass spectrometer is 10%.

$$J_x = [x - y]F\frac{1}{V_m}\frac{1}{60}\frac{1}{SA} \qquad 3.3$$

The performances of membrane reactors were compared in terms of the rate of products formed due to water permeation. Following the experiments the membrane reactors were removed for post operation analysis. The membrane surfaces on the feed and permeate side were analysed by XRD, SEM and EDXS analysis.

d) Polarisation/ Fuel Cell Experiments

The BCY20 disc membrane was prepared with a thickness of 1.4–1.6 mm and then polished to a thickness of 0.5 mm with an abrasive grinding paper (SiC, 600 grit). Platinum was painted on both sides of the sintered membrane covering an area of 0.5 cm^2 as cathode and anode and a platinum resin was painted as a reference electrode with an area of 0.05 cm^2. The three–electrode set up was prepared as shown in Figure 3.1b. A three–electrode cell composed of an anode, cathode, and reference electrode (working and counter electrodes were deposited symmetrically to serve as cathode/anode, the reference electrode was deposited near the edge of the pellet) was used to determine the overpotentials of the electrodes. Platinum was used as the electrode materials. By using a third electrode (RE), it is possible to measure the overpotentials of anode and cathode.

The ohmic–free overpotentials of electrodes were determined by $\eta = V_{WR}$ - OCP - IR, where V_{WR} is the potential applied with respect to the reference electrode, OCP is the open circuit potential and IR is the voltage drop between the working electrode and the reference electrode. The ohmic resistance of the electrolyte was determined by current interruption technique. The electrical resistance of the electrodes is negligible since platinum is a good electronic conductor. A gold mesh connecting with a gold wire was attached to each side of the membrane as a current collector. The gold wires leading from the electrodes were connected to the potentiostat/galvanostat (Ivium Compactstat with booster). The accuracy of Ivium compactstat in measured current/potential is 0.2%. The experiments were conducted using the dual chamber reactor shown in Figure 3.1b.

The experiments were performed at a fixed temperature of 700 °C. The current–voltage characteristics were obtained by DC measurements for each cell configuration shown in

Figure 3.5. The performance of the fuel cell modules were evaluated by measuring the OCP and the current associated with the application of potentials from OCP to 0 V with 1 mV/s steps. The simultaneous transport of oxygen and water from cathode to anode for fuel cell applications was investigated by employing the oxygen electrochemical pump technique. The potential was applied between 0 V and -1 V with 100 mV steps and an acquisition time of 200 s per voltage level between working and reference electrode (counter and reference electrodes were placed at the anode side). The current density was calculated based on geometric area of cathode (0.5 cm^2). In order to obtain the overpotential of the working electrode, the contribution of the ohmic loss was subtracted. The ohmic loss was mainly due to the electrolyte since the thick electrolyte was used for experimental convenience.

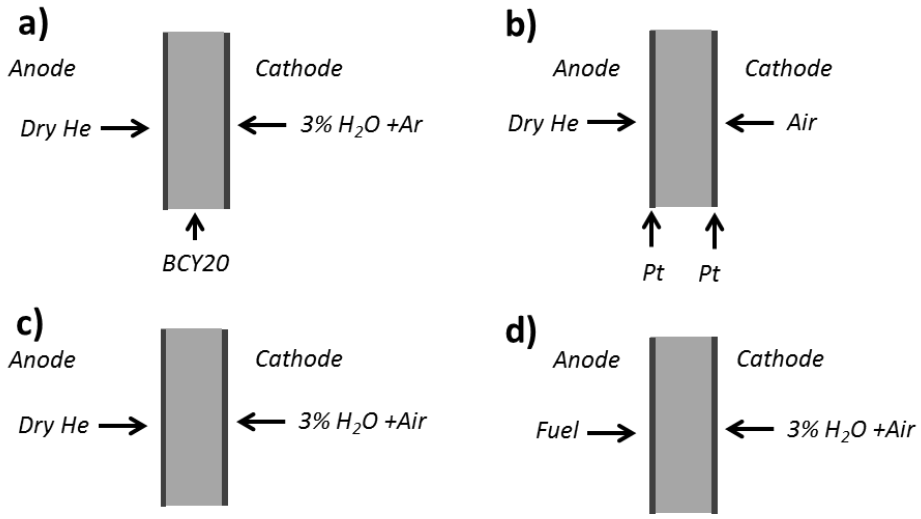

Figure 3.5: Cell configurations for dc measurements. **a)** Helium is fed to anode and 3% H_2O in argon is fed to cathode to investigate the effect of polarisation on water permeation. **b)** Helium is fed to anode and air is fed to cathode to determine oxygen evolution at the anode under polarisation. **c)** 3% H_2O and air are fed to cathode together to investigate effect of one to other and to carry out comparison with a & b. **d)** Finally, various fuels (hydrogen, carbon monoxide, methane) are individually fed to anode for fuel cell measurements.

Operation with excess current could damage the membrane. Therefore, a preliminary experiment was conducted to determine the range of the applied potential between 0 V and -2 V. However, the limiting current was not determined under these conditions since this requires the application of voltages beyond -2 V which will give a current beyond the limitation of Ivium Compactstat.

Zero grade gases (impurity less than 10 ppm) were supplied by BOC/UK with a composition of 20.5% oxygen and 79.5% nitrogen. Inlet water was controlled using the water bath and monitored with the hygrometers. Before the introduction of gases to the chambers, dry gas (helium) was passed across the membrane to remove residual water vapour at the operating temperature for 2 hrs. The hydrogen, oxygen and water concentration were evaluated by the mass spectrometer and the hygrometers (Vaisala, Finland) at the anode outlet as shown in Figure 3.2b. The anode side outlet was monitored with a hygrometer and a mass spectrometer. The outlet gas concentrations were monitored. The stable readings were taken as the concentrations at each applied potential. Similar calculation was carried out for oxygen evolution. For known gas flow rate and the gas concentration at the anode side the oxygen evolution can be obtained using Equation 3.2 given in the previous section.

3.1.5 The Analysis System

Mass spectrometry was used in order to identify the product gases leaving the membrane reactor in the permeate side in this study. For the analyses of the outlet gases, the mass spectrometry was the suitable equipment due to the suitable response time and accuracy. It can detect the change in gas composition as low as 0.5 s.

In the mass spectrometer, a sample of gas enters into the vacuum chamber, and then these neutral particles in the sample are bombarded with low energy electrons that are emitted by the filament to produce ions. The positively charged ions are accelerated in an electric field. The ions are then separated according to their mass to charge (m/e) ratio by the four rod electrodes before the detector. The separated ions are detected by the ion detector. The data recorded by the mass spectrometer can be converted into the mole fractions by the software. First step of calculating mole fraction of a specific mass is to calculate partial pressure of that

mass. Partial pressure of a specific mass shows relative amount of that mass as a fraction of total. The total pressure is measured in the total pressure plate mounted in the ion source. Finally, an algorithm is used to calculate partial pressures by taking into account the peak intensity, the ionisation probability, the fragmentation factor and a transmission factor [96].

The calibration of the mass spectrometer was carried out before every experiment. The mass spectrometer was calibrated for water permeation experiments by using a standard calibration gas mixture of; 2% nitrogen, 2% oxygen, 1% hydrogen balance in helium. For water gas shift experiments, the calibration was performed using 2% methane, 2% carbon monoxide, 2% oxygen, 2% carbon dioxide, 2% hydrogen balance in helium standard calibration gas mixture and individual 1% argon gas calibration balanced with helium. The carrier gas was helium for all membrane based experiments. The calibration was performed by using the same flow rate as the experiments (See Appendix G for calibration plots).

The water content of the feed stream leaving the water bath and the water content of permeate stream leaving the membrane reactor were monitored by a dew point hygrometer (Vaisala HMT337) which has an accuracy of ±0.2 °C of the dew point. The unit was self–calibrated and calibrated by comparing the readings of the instrument to working standards of the manufacturer (Vaisala Oyj, Finland). To ensure that the hygrometers were working efficiently and precisely; they were checked regularly with each other and send back to the manufacturer for calibration.

3.2 Analytical Techniques

This section describes the characterisation techniques that used to analyse microstructure, morphology and chemical composition of the membranes.

3.2.1 X–Ray Diffraction (XRD)

X–rays are electromagnetic radiation which has wavelengths in the Angstrom range (10^{-10}m). X–rays are generated by bombarding a metal with high energy electrons [97]. The electrons slow down as they plunge into the metal and collide with the electrons from the inner shell of an atom. This collision of incoming electrons with the electrons creates electron vacancy and an electron with high energy drops into the vacancy and emits the excess energy as an x–ray photon [98].

X–ray diffraction (XRD) is a technique used to measure approximate space between layers and rows of atoms to determine the crystal structures, orientation of the crystal structures and measure the size, shape and stress in the crystal structure. Every structure reflects the x–rays at specific angles which gives the characteristic of the sample. When the incident x–ray hits the lattice plane, the reflection happens in the same angle as shown in Figure 3.6. The spacing between two lattices is expressed by Bragg`s law.

$$n\lambda = 2d\sin\theta \qquad 3.4$$

Where d represents the distance between the planes, θ represents the incident angle, λ is the wavelength of the beam and n is an integer.

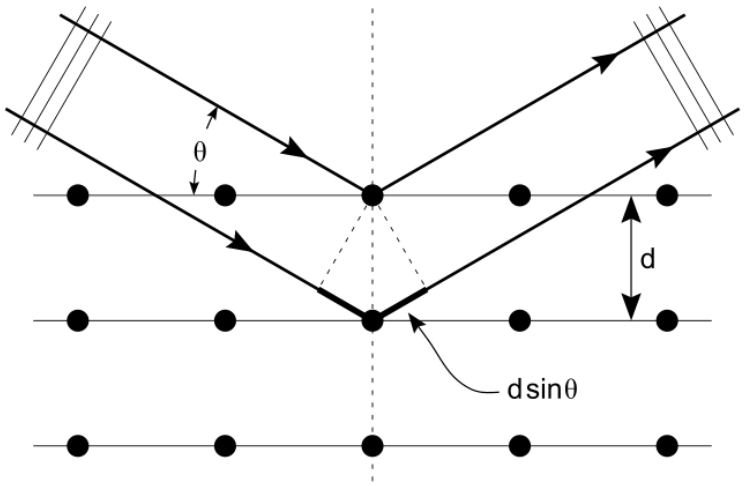

Figure 3.6: Bragg diffraction [97]

When the geometry of incoming x–rays entering the sample fits with the Bragg equation, constructive interference occurs and a peak is seen in the intensity. The lattice parameters can be estimated by using Miller indices ($h,\ l,\ k$). Miller indices are the reciprocals of intersection distances in the structure [98]. The relationship between lattice parameters and Miller indices for an orthorhombic cell such as BCY10 is given below where $a,\ b,\ c$ are the lattice parameters.

$$\frac{1}{d_{hlk}^2} = \frac{h^2}{a^2} + \frac{l^2}{b^2} + \frac{k^2}{c^2} \qquad 3.5$$

In this work, XRD characterisation technique is used to determine crystallographic structure and phase purity of the membranes before and after the experiments. A scan step size of 0.033 degrees with a scan time of 100 s per step was used to scan through $0 < \theta < 90^{\circ}$ for XRD analysis of the membranes. The results were compared with references and the International Centre for Diffraction Data (ICDD) database in order to determine crystal structure.

3.2.2 Scanning Electron Microscopy (SEM)

Scanning electron microscope (SEM) uses a beam of energetic electrons to examine samples on a very fine scale. An electron beam is generated by an electron gun (usually tungsten) and collimated by the condenser lens. The final magnetic lens corrects astigmatism and alignment and focuses the beam into the sample. When the beam (primary electrons) hits the particle in the sample, signal detection begins. The secondary electrons are detected and converted into electronic signal and finally exhibited as an image on cathode ray tube (CRT). The screen of the CRT has various spots called pixel which changes depending on the samples topography [99]. SEM gives information about topography, morphology, composition and crystallography of the samples.

In this work, SEM characterisation technique is used to determine the morphology of the membranes before and after the experiments. Density and porosity of the membranes can be easily seen from the SEM images of BCY20.

3.2.3 Energy Dispersive X–Ray Spectroscopy (EDXS)

Energy dispersive x–ray spectroscopy (EDXS) is a semi-quantitative analytical technique which is commonly applied to determine chemical characterisation of a sample such as elemental identification. In this technique, an incoming x–ray excites an electron in the inner shell of the sample and leaves a vacancy behind. A higher energy outer shell electron then fills this vacancy and emits a characteristic x–ray. These x–rays are unique for each element and named based on the name of the electron shells such as K, L, and M. The number of shells that are jumped by the electron are subscripted as α (one-shell jump), β (two-shell jump) and so on [100]. For instance, K_α x–rays are emitted by the electron jump from the L shell to the K shell. The number and the energy of the x–rays are measured by a detector in order to identify elemental composition of the sample.

EDXS has been used in this study to quantify the elemental composition of the BCY20 membranes before and after the experiments so as to investigate any structural changes on the membrane surface.

3.3 High Temperature Membrane Sealants

High temperature membrane sealants are crucial to obtain a gas tight membrane module for laboratory studies. A good sealant material should have certain properties such as good chemical compatibility with the membrane and the support tube, easy and flexible design, similar thermal expansion coefficient to the membrane module and so on [101]. The thermal mismatch between the membrane and the seal often causes damaging of membrane module. Thus, it is important to ensure the membrane and the seal has similar solidity and thermal expansion under the same operating conditions. The thermal expansion coefficient for BCY20 is reported about 14-16×10^{-6}/K in the literature [70].

The most common used sealant materials for the membrane studies so far are gold, silver O–rings and glass–based materials. The problems associated with these sealant materials are; O–rings require an external compression force and glass sealants have higher melting points to fill the gaps between the membrane and tube. In addition, it is extremely difficult to remove the membrane without damaging after the experiments. Therefore, an investigation of sealant material compatible with the membrane properties is necessary for the accuracy of the measurements.

A number of sealant materials listed in Table 3.2 are tested for the membrane based permeation/reaction experiments. The table simply displays the materials that are used to prepare the sealants along with mixing percentages of them by weight. The preparation of disc membrane and the test module are described in *Section 3.1*. All the sealants are tested using nitrogen in one chamber and helium in the other chamber. The gas tightness of each membrane is verified using the experimental temperature. The helium stream is analysed using a mass spectrometer for possible nitrogen leak. All given leak rates are based on nitrogen composition in helium. The membrane is considered gas tight if the nitrogen concentration is less than 10 ppm in helium side.

The seal 1 and 2 are purchased from Fuel Cell Materials (70 wt. % Silver, 70 wt. % Gold) and applied to the membrane module as shown in Figure 3.1a. The membrane module is kept at

the room temperature for 24 hrs to dry before placing into the reactor. After placing the membrane into the reactor, the temperature is taken to 700 °C at a ramp rate of 1 °C/min. Following the introduction of gases, approximately 1% leak rate is observed. The main problem is poor bonding of silver/gold paste to the alumina tube.

Table 3-2: List of the sealants studied for BCY membrane module

Series	Material , wt. %	Material, wt. %	Material, wt. %	Observation
1	Silver, 70	-	-	Poor
2	Gold, 70	-	-	Poor
3	Toku Ceramic, p24,50	Ceramabond 503, 50	-	Moderate
4	Waterglass,100	-	-	Poor
5	Gold, 20	Water glass,80	-	Poor
6	V4, 50	Water glass,50	-	Poor
7	V8, 50	Water glass, 50	-	Poor
8	Pyrex glass, 50	Water glass, 50	-	Poor
9	LSCF, 20	Water glass, 80	-	Poor
10	BCY20, 20	Water glass, 80	-	Poor
11	BCY20, 40	Pyrex glass, 50	$NaAlO_2$, 10	Good
12	BCY20,40	Water glass,60	-	Poor
13	BCY20, 60	Pyrex, 40	-	Very Good

The ceramic sealant pastes, seal 3 (Toku ceramic–p24, Aremco Ceramabond 503) are mixed 50 wt. % and applied to the counter of the alumina tube and dried 3 hrs at room temperature and tested again at 700 °C. This mixture displays good performance under the dry gas atmosphere, however, in the presence of steam, the leak rate increases above 1%.

The seal 4, water glass (35–45 wt. % sodium silicate (Na_2SiO_3), Aremco 571–l) separated on the membrane surface and blocked the permeation/reaction area of the membrane. The gold paste (seal 5) is applied to prevent the water glass leaking onto the membrane surface before

application of the water glass around the alumina tube as shown in Figure 3.7. The leak rate obtained with this method is below 1%, but still lower than aimed in this study which is below 20 ppm.

Two sealant materials V4 and V8 (V4; $40SiO_2\_15B_2O_3\_27BaO\_18MgO$, mol% and $40SiO_2\_15B_2O_3\_27BaO\_10MgO\_8ZnO$, mol%) provided by Instituto de Ceramica y Vidrio are also tested as the seals 6 and 7. The sealant paste is prepared by mixing with 50 wt. % water glass. The sealant material is found cracked after cooling the reactor to the room temperature and the leakage is high (above 1%) compared with the sealant materials studied previously.

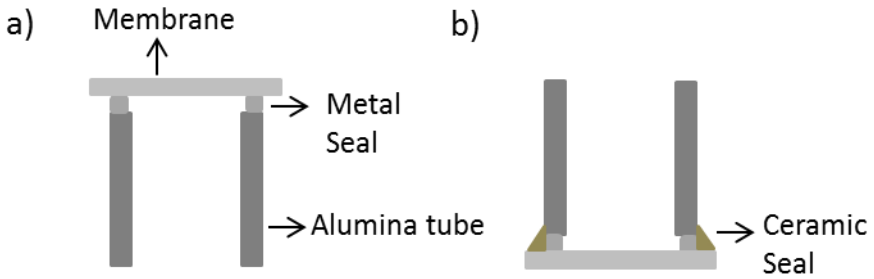

Figure 3.7: Configuration of sealant application to membrane module which is applied for the seals 9-13. **a)** Silver paste is applied around the outer diameter of the alumina tube. Then it is kept for 24 hrs at the room temperature to dry. **b)** The prepared ceramic paste is applied around the membrane as shown. Then membrane module is placed into the reactor after 3 hrs drying at the room temperature. The temperature is taken to the 900 °C at a ramp rate of 1 °C/min. It is kept at this temperature for 30 min and then the temperature is cooled down to 700 °C at a ramp rate of 1 °C/min.

The investigation of sealant material continued until a sealant recipe is found which has similar properties such as thermal expansion coefficient to the membrane. Subsequently, testing Pyrex glass which is obtained by crushing the Pyrex glass tubes (SiO_2 (80.6 wt. %), B_2O_3 (13 wt. %), Na_2O (4 wt. %), Al_2O_3 (2.3 wt. %), K_2O (0.1 wt. %)), seal 8, this approach is extended involving the membrane material. The seal 8 responded in similar way as the seal 4.

The following curing method is applied for the seals 9-13; silver paste is applied around the outer diameter of the alumina tube as shown in Figure 3.7a. Then it is kept for 24 hrs at the room temperature to dry. Subsequently, a ceramic paste is prepared using the mixture given in Table 3.2. The water glass is used as the solvent. The ceramic paste is applied around the membrane as shown in Figure 3.7b. The membrane module is placed into the reactor after 3 hrs drying at the room temperature. The temperature is taken to the 900 °C at a ramp rate of 1 °C/min. Since the Pyrex has a melting point of 820 °C. It is kept at this temperature for 30 min and then the temperature is cooled down to 700 °C at a ramp rate of 1 °C/min. Application of the silver paste prevented the Pyrex glass separating onto the membrane surface and closing the reaction area as well as increasing the performance of the ceramic sealant materials.

First attempt is carried out using the LSCF ($La_{0.6}Sr_{0.4}Co_{0.2}Fe_{0.8}O_{3-\delta}$) powder 20 wt. % and the water glass 80 wt. %. The sealant is found cracked when the temperature is cooled down. Thus, the powder is switched to BCY20 and the content of the Pyrex glass is reduced in the mixture. From the seal 10 to 13, similar procedure is followed. The seal 13 exhibited the best performance among them. The success is 100% (nitrogen composition in helium stream is less than 10 ppm). There is no crack observed in the sealant material and the membrane itself when the temperature is cooled down to the room temperature. This suggests that the thermal expansion/shrinkage of the sealant material and the membrane are close to the each other. The gas tightness and the bonding of the seal are achieved in the test 13.

Different sealing recipes are studied in order to find a compatible sealant material to the BCY20 membrane and the alumina tube. The chemical and thermal properties of the seal are significantly important to obtain a gas tight and inert sealant material under the operating conditions for the experiments. The recipe 13 resulted in the very best performance for the dense BCY20 membranes using the given procedure. The seal 13 is used for all the experiments unless the otherwise is stated.

Chapter 4
Modelling Hydration of BCY Membranes

4.1 Introduction

In this chapter, a model is developed to calculate the diffusion coefficients for the transfer of defects and simulate concentration distributions of defects within the BCY10 and BCY20 membranes. The multi–species mass transfer processes within BCY membranes can be simulated using the Nernst–Planck equation. The Nernst–Planck equation with boundary conditions is used to calculate diffusion coefficients of defects in COMSOL. All the partial differential equations are solved numerically. This also provided the information of the concentration distribution of the defects along the thickness of the membrane. Additionally, the electrical potential profiles along the thickness of the membrane can also be predicted.

The model is validated experimentally. This is done by monitoring the transient behaviour of electrical potential change during hydration of the membranes by changing the surrounding atmosphere at the membrane surface as a function of time at a fixed temperature, until equilibrium is reached. The experiment is performed in a single chamber reactor by isolating one side of the membrane from the surrounding atmosphere. The transient potential difference along the thickness of the membrane can be measured between exposed and isolated surfaces. A potential difference is established between exposed and isolated surfaces due to concentrations gradients of species having different diffusion coefficients.

4.2 Development of Model

The species mass transfer processes within BCY membranes can be simulated with the Nernst–Planck equation. The concentration profile of protonic defects and oxygen vacancies across the membrane thickness can be obtained by applying suitable boundary conditions on the gas/membrane interface.

4.2.1 Physical model

Figure 4.1 shows the schematic of the physical process of this study. The hydration of the membrane surface, the electrical potential change and diffusion of defects ($OH_O^{\bullet}$, $V_O^{\bullet\bullet}$) along the thickness of the BCY membranes are modelled and evaluated. The existence of charged species within the membrane is dependent on the molecular species (such as water vapour, oxygen etc.) in the surrounding gaseous environment. The electronic defects (electrons and holes) within the BCY membranes have been ignored, as the possibility of their existence is low because the gaseous environment in this study consists of 1% water vapour in nitrogen. Therefore, the oxygen partial pressure is assumed to be very low and constant. The model is based on solution of the Nernst–Planck equation with boundary conditions in a membrane system which is in contact with the gas phase.

The water transport involves four steps as shown in Figure 4.1 which are as follows:

1. The convection of water vapour (steam) in the gas phase.

2. The diffusion of water through the boundary layer and platinum layer.

3. The reaction of water with BCY membrane surface and its incorporation.

4. The migration of $OH_O^{\bullet}$ and $V_O^{\bullet\bullet}$ species within the BCY membrane.

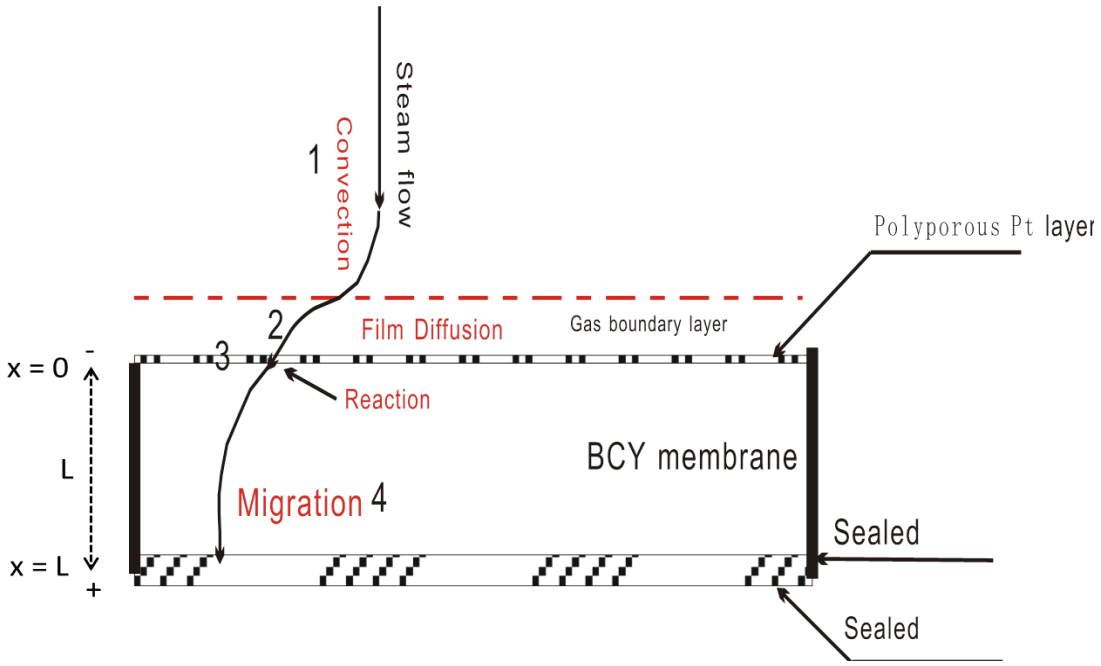

Figure 4.1: Schematic of hydration of the BCY membrane. The first process involves transport of water in the gas phase, the second process is water diffusion in the gas boundary layer, in the third process defect formation reaction takes place (water reacts with oxygen vacancy and lattice oxygen to form protonic defects) and the fourth process displays diffusion of defects within the membrane. The surface is coated with a thin platinum layer. The other surface of the membrane is sealed to isolate this surface from the surrounding atmosphere.

4.2.2 The Nernst–Planck Equation

The Nernst–Planck equation is a conservation of mass equation which describes the effect of an ionic concentration gradient and an electric field on the motion of chemical species, especially on ions. The conservation of mass equation is [102]:

$$\frac{dc_i}{dt} = -\frac{dJ_i}{dx} \qquad 4.1$$

The flux function J_i represents molar flux of ith ion species (mol/m^{2}s) and c_i represents molar concentration of ith ion species (mol/m^3).

The molar flux of ion species consists of three parts; convection, diffusion and migration.

$$J_i = J_{i,c} + J_{i,d} + J_{i,m} \quad 4.2$$

$$J_i = c_i u - D_i c_i + c_i U_i F_{i,e} \quad 4.3$$

Equation 4.3 describes movement of charged species. All species in bulk will be transported with a common velocity, u (m/s), in the absence of concentration gradient and electrical field. The mass flux of species i under these conditions is described as the convective flux and given as $c_i u$.

In the presence of concentration gradients of species, diffusion flux arises. The mass flux of species i due to diffusion is given by Fick`s first law, $D_i c_i$. The coefficient D_i (m^2/s) is referred as the diffusion coefficient of the species i. Since the diffusion mass flux takes place from high concentration to low concentration, substitution of diffusion mass flux to overall mass flux is given as $-D_i c_i$.

When charged species are transported, the movement of charged species will create an electric field. This kind of transport is referred as migration. The mass flux due to migration also contributes the overall flux equation. The created electrical field is proportional to the negative gradient of potential (V) and gives rise to a force for charged species i as follows:

$$F_{i,e} = -z_i e \nabla V \quad 4.4$$

Where z_i represents the charge number of species and e represents the elementary charge of an electron (C).

The Nernst–Planck equation is constituted as follows:

$$\frac{dc_i}{dt} = c_i u - D_i \frac{dc_i}{dx} - c_i U_i z_i e \frac{dV_i}{dx} \quad 4.5$$

Mobility of species is related to diffusion coefficients by the Nernst–Einstein relation as follows:

$$U_i = \frac{D_i}{k_B T} \quad 4.6$$

and,

$$F = eN_A \quad 4.7$$

$$k_B = \frac{R}{N} \quad 4.8$$

where F and k_B are Faraday constant (C/mole) and Boltzmann constant (J/K), R is the universal gas constant (J/K mole), N Avogadro constant (1/mole) , e is the elementary charge (C) and T is the temperature (K).

The Nernst–Planck equation can be rewritten as:

$$\frac{dc_i}{dt} = c_i u - D_i \frac{dc_i}{dx} - c_i z_i \frac{D_i F}{RT} \frac{dV_i}{dx} \quad 4.9$$

where i represents all the species that are present in the membrane and u represents gas flow rate.

4.2.3 Mathematical Model

The mathematical model includes three parts: governing equations, initial values and boundary conditions. The mathematical interpretations of the four physical steps (*Section 4.2.1*) have been described below.

1. The convection of water in the gas phase does not affect the process and thus it can be neglected. The partial pressure of water therefore, in the gas side of the boundary layer along the membrane surface is taken to be constant.

2. The film diffusion step in the gas phase boundary layer can be represented by the following driving force equation.

$$\frac{dC_{S,H_2O}(t)}{dt} = -k_f \times \left(C^*_{H_2O}(t) - C_{out}\right) - R_{e,H_2O} \qquad 4.10$$

where k_f is mass transfer coefficient, m/s; C_{S,H_2O} represents the surface concentration of H_2O, mol/m^2; R_{e,H_2O} represents surface reaction rate of H_2O with the membrane, mol/(m^2.s), $C^*_{H_2O}(t)$ represents the concentration of H_2O in equilibrium with the concentration of $OH^{\bullet}_O$ on the membrane surface, mol/m^3; C_{out} represents the bulk concentration, mol/m^3. Equation 4.10 defines the concentration of H_2O on the BCY membrane surface which is time dependent and requires initial values. The initial values that are used; P_{out} = 0.01 atm, $C_{out} = \frac{P_{out}}{RT}$, t = 0 $\mathrm{C_{s,H_2O}(L, t) = 0}$.

3. The third step represents the reaction of water with BCY on the membrane surface, represented as follows:

$$H_2O + V^{\bullet\bullet}_O + O^x_O \overset{K}{\leftrightarrow} 2OH^{\bullet}_O \qquad 4.11$$

$$K = \frac{k_1}{k_2} = \frac{C_{OH_O^\bullet}^2}{C_{V_O^{\bullet\bullet}} C_{O_O^x} \; P_{H_2O}^*/P_0} \quad 4.12$$

where K is the reaction equilibrium constant, k_1 is the forward reaction rate constant (m^2/mol.s), k_2 is the reverse reaction rate constant (m^2/mol.s), $P_{H_2O}^*$ is the partial pressure of water on the membrane surface and P_0 is the atmospheric pressure (Pa).

The equation 4.12 relates equilibrium constant (thermodynamic value) to forward and reverse rate constants. If one of the rate constants is known, the other one can be calculated by using equilibrium constant.

The concentration of reactants will be reduced by the forward reaction, but also will be increased by the reverse reaction, thus the net reaction rate of Equation 4.11 (R_a, mol/m^2.s) is given as follows:

$$R_a = (k_1 \, C_{V_O^{\bullet\bullet}} C_{O_O^x} P_{H_2O}^*/P_0) - k_2 C_{OH_O^\bullet}^2 \quad 4.13$$

$$R_a \; = k_1 \left\{ (C_{V_O^{\bullet\bullet}} C_{O_O^x} P_{H_2O}^*/P_0) - \frac{1}{K} C_{OH_O^\bullet}^2 \right\} \quad 4.14$$

The reaction rates of reactants and products can be shown with Equations 4.15 to 4.18 respectively.

$$R_{e,H_2O} = -R_a \quad 4.15$$

$$R_{e,O_O^x} = -R_a \quad 4.16$$

$$R_{e,V_O^{\bullet\bullet}} = -R_a \quad 4.17$$

$$R_{e,OH_O^{\bullet}} = 2R_a \quad 4.18$$

where, R_e represents surface reaction rate of species.

Reaction rates from Equation 4.15 to 4.18 are time dependent and require initial values. The initial values of the various species in the membranes used in this study are calculated from the stoichiometry of BCY membranes equilibrium with the given gas–phase environment at the surface and presented in Table 4.1(See Appendix H for detailed calculations). The doping concentrations of yttrium used in the analysis are 20 mol% for BCY20 and 10 mol% for BCY10.

Table 4-1: Initial concentration of species (see Appendix H for detailed calculations).

Species	**Concentration**	**Charge**
BCY20 ($BaCe_{0.8}Y_{0.2}O_{2.9}$)	1.7371×10^4 mol/m^3	0
O_O^x	5.0377×10^4 mol/m^3	0
Y_{Ce}'	3.4743×10^3 mol/m^3	-1
$V_O^{\bullet\bullet}$	1.7371×10^3 mol/m^3	2
$OH_O^{\bullet}$	0	1
Species	**Concentration**	**Charge**
BCY10 ($BaCe_{0.9}Y_{0.1}O_{2.95}$)	1.5130×10^4 mol/m^3	0
O_O^x	4.4633×10^4 mol/m^3	0
Y_{Ce}'	1.513×10^3 mol/m^3	-1
$V_O^{\bullet\bullet}$	7.565×10^2 mol/m^3	2
$OH_O^{\bullet}$	0	1

4. The fourth step includes the diffusion of two species ($OH_O^{\bullet}$ and $V_O^{\bullet\bullet}$) within the BCY membranes. This process is represented with the Nernst–Planck equation. In this study one–dimensional transport through the membranes along the thickness is considered.

The Nernst–Planck equation is derived in Equation 4.9. The first term of the equation represents convection, the second part and the third part represent diffusion (due to concentration gradient) and migration (electrical potential gradient), respectively. The convection part of the equation can be ignored as the rate of convection in the gas phase is too rapid as compared to diffusion processes. Therefore Equation 4.9 becomes:

$$J_i = -D_i \nabla c_i - c_i z_i \frac{D_i F}{RT} \nabla V \quad 4.19$$

The conservation form of mass transfer equation in one–dimension is:

$$\frac{dc_i}{dt} + \frac{d}{dx} J_i + c_i u = R_i \quad 4.20$$

By substituting Equation 4.19 into Equation 4.20, the conservation equation can be presented as:

$$\frac{dc_i}{dt} + \frac{d}{dx}\left(-D_i \nabla c_i - z_i c_i \frac{D_i F}{RT} \nabla V\right) + c_i u = R_i \quad 4.21$$

Equation 4.21 applies to all of the species within BCY membrane and represents a series of equations.

The electro neutrality condition applies throughout the membrane:

$$\sum_i z_i c_i = 0 \quad 4.22$$

The net charge throughout the membrane is zero, meaning that the number of Q-1 charged species where Q is the number of species present, can be solved using Equation 4.21. The

remaining species concentration can be calculated using Equation 4.22. The movable charges within the BCY membrane are $OH_O^{\bullet}$ and $V_O^{\bullet\bullet}$ which are both positive. Thus, a negative charge should be taken into account for the electro neutrality condition. The negative charge used is Y'_{Ce}. The diffusion coefficient of Y'_{Ce} compared to protonic defect and oxygen vacancy is very small. Therefore, the diffusion coefficient for Y'_{Ce} is considered to be very low and constant.

The electrical potential is calculated using the relations below by adding the mass transfer equation of every charged species and multiplying this sum with Fz_i. The current density (associated with defect concentration) relation is given as follows:

$$\mathrm{i}_t = F\sum_{i=1}^{n} z_i(-\mathrm{D}_i\nabla c_i - \mathrm{z}_i\mathrm{c}_i\mathrm{u}_{mi}F\nabla V) \qquad 4.23$$

Equation 4.23 displays conservation of electric charge and relates electric potential to concentration. Equations 4.21 and 4.23 are time and space dependent and require initial values and boundary conditions described in the next section. These are sufficient to describe the concentration distribution of ions, vacancies and the electric potential within the membranes as a function of time and space.

4.3 Model Boundary Condition

Discretisation of Membrane

The water diffusion in the membrane may be treated as a one–dimensional problem in order to predict defect distribution along the thickness of the membrane. This assumption could be employed only when membrane thicknesses are small compared to radial surface areas. Thus, diffusion can be assumed to happen in one direction. Equations used in this model are therefore considered to be only in one dimension. The electric potential of the isolated surface of the membrane at x= L is specified as 0 V.

The BCY membrane can be discretised into finite volumes as shown in Figure 4.2. The system can be then solved using high level software for the numerical solutions of differential equations [103].

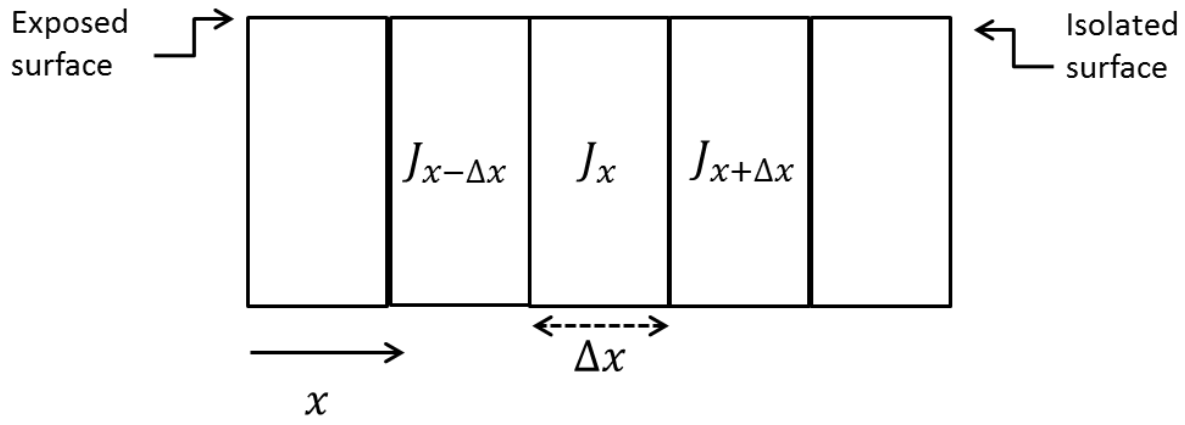

Figure 4.2: Illustration of a finite volume within BCY membrane that represents discretisation of membrane for fluxes of species. $J_{x-\Delta x}$ and $J_{x+\Delta x}$ represent neighboring volumes.

When only the diffusion is taken into consideration, based on mass balance, the relationship of the concentration of species i with time can be given as in Equation 4.24.

$$S \times [\mathrm{C}_i(x, t+\Delta t) - \mathrm{C}_i(x,t)] \times \Delta x = S \times [J_i(x,t) - J_i(x+\Delta x, t)] \times \Delta t \quad 4.24$$

Both sides of the equation can be divided by $S \times \Delta x \times \Delta t$;

$$[\mathrm{C}_i(x, t+\Delta t) - \mathrm{C}_i(x,t)]/\Delta t = -[J_i(x+\Delta x, t) - J_i(x,t)]/\Delta x \quad 4.25$$

Boundary Conditions

The water dissociation reaction occurs on the surface of BCY membrane, $OH_O^{\bullet}$ is produced on this surface and permeates into BCY membrane (in the positive direction shown in Figure 4.1) where $J_{OH_O^{\bullet}}$ represents the flux of $OH_O^{\bullet}$ at the boundary of the membrane (mol/m^{2}s).

At the boundary, the mass balance of $OH_O^{\bullet}$ can be written as following:

$$S \times \left(C_{OH_O^{\bullet}}(t+\Delta t)\big|_{x=0} - C_{OH_O^{\bullet}}(t)\big|_{x=0}\right) = -S \times \Delta t \times J_{OH_O^{\bullet}}(t)\big|_{x=0} + S \times \Delta t \times R_{OH_O^{\bullet}}\big|_{x=0} \quad 4.26$$

Where S represents the surface area (m^2), $J_{OH_O^{\bullet}}$ represents the flux of $OH_O^{\bullet}$ at the boundary of membrane (mol/m^2.s) and $R_{OH_O^{\bullet}}$ represents the surface reaction rate of $OH_O^{\bullet}$ (mol/m^2.s).

Following the same steps for $V_O^{\bullet\bullet}$, the boundary conditions for $OH_O^{\bullet}$ and $V_O^{\bullet\bullet}$ for both surfaces are:

x=0 exposed surface boundary conditions;

$$J_{OH_O^{\bullet}}(t)\big|_{x=0} = -\left.\frac{dC_{OH_O^{\bullet}}(t)}{dt}\right|_{x=0} + 2R_a|_{x=0} \quad 4.27$$

$$J_{V_O^{\bullet\bullet}}(t)\big|_{x=0} = -\left.\frac{dC_{V_O^{\bullet\bullet}}(t)}{dt}\right|_{x=0} - R_a|_{x=0} \quad 4.28$$

$$V=0 \quad 4.29$$

x=L isolated surface boundary conditions;

$$\frac{dC_i}{dx} = 0 \quad 4.30$$

$$\frac{dV}{dx} = 0 \tag{4.31}$$

The functions used in this model to regress initial values of $D_{V_O^{\bullet\bullet}}$ and $D_{OH_O^{\bullet}}$ are taken as [15]:

$$D_{V_O^{\bullet\bullet}} = 1.10 \times 10^{-6} exp\left(\frac{-52083.55}{8.314 \times T}\right) \ m^2/s \tag{4.32}$$

$$D_{OH_O^{\bullet}} = 2.03 \times 10^{-6} exp\left(\frac{-68480.23}{8.314 \times T}\right) m^2/s \tag{4.33}$$

The reaction equilibrium constant for Equation 4.12 which relates concentration of species, is calculated as follows [15]:

$$K = \frac{exp(\Delta H - \Delta ST)}{RT} = \frac{exp(162200 - 166.7T)}{8.314T} \tag{4.34}$$

where T is temperature (K).

The initial concentration of ions and vacancies taken into account in the model are given in Table 1. The partial differential equations are calculated with backward Euler method with the initial assumptions. The concentrations of species are calculated using the Nernst–Planck equation including boundary conditions. The least–square method ($error\ function = \sum_{n=1}^{N}(V_{cal} - V_{exp})^2$) is applied for regression of parameters.

4.4 Model Results and Discussion

4.4.1 Electrical Potential of Membranes

The hydration process of BCY membranes involves two significant processes; the mass transfer process and the formation of electric field within the membrane to maintain electro neutrality. The multi–species mass transfer processes within BCY membranes that are affected by electric field, can be simulated using the Nernst – Planck equation.

Figure 4.3 shows the experimental results for the electrical potential change during hydration and dehydration of Al_2O_3, BCY20 and BCY10 membranes, respectively. The graph presented in Figure 4.3.a is obtained from a blank experiment that performed with an Al_2O_3 membrane. Al_2O_3 membrane is operated at the same conditions as BCY20 and BCY10 membranes in order to confirm whether the potential change occurs due to hydration/dehydration of BCY20 and BCY10 membranes. Al_2O_3 membrane is chosen since hydration of this material does not involve defect formation and diffusion [104]. During this experiment, dry helium is fed to the reaction chamber which is then switched to 1% H_2O in nitrogen at 500 s and kept the same until it is switched back to dry helium again after 2500 s. As seen from Figure 4.3a that no potential change is observed by the change in surrounding environment. Therefore, the potential changes observed in Figure 4.3b and Figure 4.3c can be attributed to potential changes of BCY20 and BCY10 membranes during hydration and dehydration due to formation and conduction of charged defects.

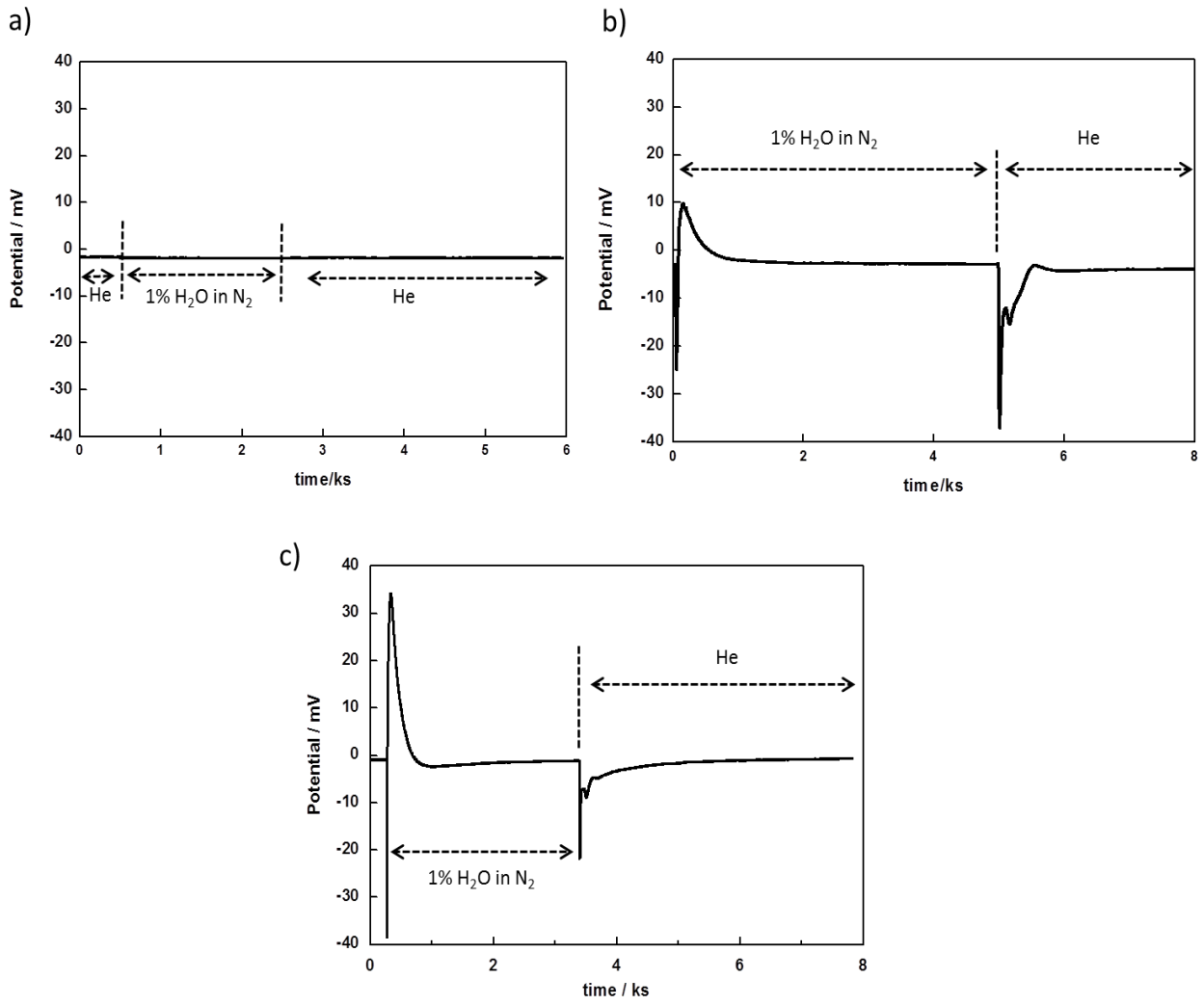

Figure 4.3: The electrical potential change of BCY membranes upon hydration and dehydration measured under open circuit conditions at 700 °C. **a)** Al_2O_3 (no signal is observed, only background signal is seen), **b)** BCY20, **c)** BCY10. (The membrane reactor is fed with dry helium for 24 hrs before the experiments, and then 1% H_2O in nitrogen is introduced to the reactor chamber which corresponds to first peaks in the graphs. The second peak appears when 1% H_2O in nitrogen is switched back to dry helium. The flow rates of gases are 200 ml/min)

The time necessary to change the surrounding atmosphere of the membranes and obtain a stable water concentration inside the reactor chamber is very short (~17 s) compared to the equilibration time (>500 s). Therefore, the partial pressure of water is assumed constant during hydration of membranes.

The electrical potential change is associated with concentration gradients of the mobile charges $OH_O^{\bullet}$ and $V_O^{\bullet\bullet}$ during hydration and dehydration within the membranes. The water incorporation within the membrane does not affect its electro neutrality. When no external electrical driving force is applied; the chemical potential difference (concentration gradient) of water between the surrounding atmosphere and the membrane is the driving force for water incorporation.

The first peaks in Figure 4.3b and 4.3c are related to a potential change during hydration in both cases; the second peaks correspond to potential change during dehydration. Water concentration in the gas phase for hydration of the membranes is kept as 1% for both membranes. The experiments are repeated for both membranes to see if they are reproducible. The transient behaviour of the membranes are reproduced (see Appendix I). Following the introduction of 1% H_2O in nitrogen to the reactor chamber, an electrical potential difference is observed due to sudden increase in the water partial pressure and a quick change in the ratio of oxygen vacancy and protonic defect at the exposed surface compared to the bulk. The electrical potential overshoots (~2 s) and then it slowly decays toward final initial state (~500 s). This demonstrates that electrical potential increases quickly when water incorporates into the membrane and decreases with the diffusion of species. When 1% H_2O in nitrogen is subsequently switched to the dry helium, the electrical potential changes in exactly the opposite trend; dehydration occurs fast at first then extends over many seconds and eventually approaches the initial state. The hydration of membranes is enough to extract diffusion coefficient of defects within the membranes. Thus further discussion will continue based on hydration of membranes.

The approximate potential difference values for BCY20 and BCY10 are 10 mV and 35 mV, respectively. As seen from Figure 4.3b and Figure 4.3c that BCY10 displayed higher potential difference and shorter charge redistribution period than BCY20. This divergence may be associated with the difference in concentration of charge carriers, surface kinetics and diffusion coefficients of protonic defects and oxygen vacancies. For every mole of dopant, half mole of oxygen vacancy is formed. Thus, BCY10 has lower oxygen vacancy concentration than BCY20. By assuming that both membranes have similar surface kinetics (since temperature, electrode and water concentration are the same for both membranes), it

may be said that charge separation and redistribution happen quicker when charge carrier concentration is less.

The potential difference between the surfaces increases fast at the beginning and then slowly diminishes. The sudden change in electrical potential could be due to the fast kinetic process of the adsorption, dissociation and incorporation of water on to the surface/bulk or/and fast defect formation. This fast hydration was also observed by Schober *et al* [105]. Their dilatometry results showed rapid expansion with the injection of water into the dilatometer (water concentration ~ 0.03%) followed by slow expansion.

Additionally, the diffusion coefficients of protonic defects are reported as greater value than that of oxygen vacancies in literature [14, 91]. Similarly, Yoo *et al* [106-108] studied mass relaxation of $BaCe_{0.95}Yb_{0.05}O_{2.975}$ and $SrCe_{0.95}Yb_{0.05}O_{2.975}$ proton conductors upon hydration and dehydration. They also reported fast diffusion of H followed by sluggish diffusion of O. Therefore, it may be speculated that protons incorporate into the membrane fast and diffuse quickly by leaving oxide ions behind. This can create an unbalanced charge distribution due to the distribution of fixed negatively charged species within the membranes. As the oxide ions catch up the protons, the electrical potential difference returns to its initial level and the concentrations gradients of species disappear within the membrane. The uniform charge distribution is restored and the potential becomes uniform again.

The overshoot period (~2 s) in electrical potential is short compared to the period to establish uniform concentration distribution (400–500 s) as seen from Figure 4.3b and 4.3c, implying that bulk diffusion period is two orders magnitude higher than the surface processes (i.e. adsorption, protonic defect formation). Additionally, this period is higher for BCY20 membrane than BCY10 membrane (BCY10, ~550 s and BCY 20, ~650, see Figure 4.3). These differences may be related to the difference in membrane thicknesses (diffusion length for re–equilibration) or dopant concentrations.

The experimental data and model fit for potential change during hydration is shown in Figure 4.4. The optimisation module in Comsol is used to find best match to the experimental data.

This option allows finding the optimum parameters to minimise difference between estimated and experimental data after many iterations of calculations (least–square type). Figure 4.4 shows a satisfactory fit between model and experimental data (R^2 = 0.997 for BCY20 and R^2 = 0.986 for BCY10). However, some deviation is observed when the potential difference decreases. The fitting process for a straight line can be managed easily, on the other hand a curve fitting process is much complex. The least square optimisation which is a well-established and simple method was used in this study and showed a reasonable fit with the experimental data. One limitation with this method is that the data points which are differ from the majority of the data can skew the regression [109]. This may be the reason for the deviation is seen in Figure 4.4.

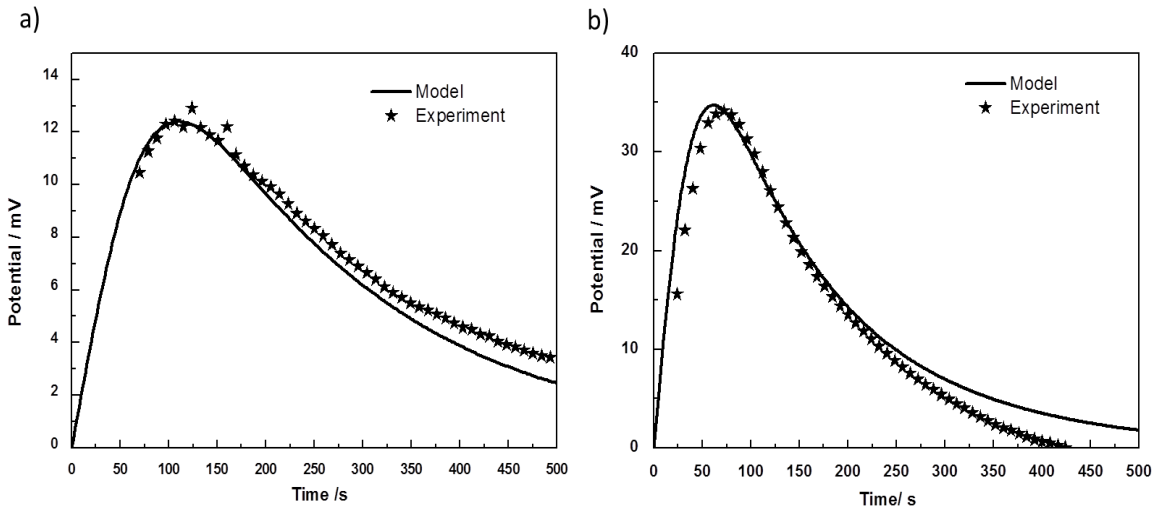

Figure 4.4: The comparison of experimental and modelled electrical potentials upon hydration. Lines = modelled results, stars= experimental results. **a)** BCY20, **b)** BCY10

The electrical potential profiles within the BCY20 and BCY10 membranes during hydration are shown in Figure 4.5. The profiles are predicted as a function of time by using Equations 4.21 and 4.23 which relate the concentration distribution of species to the electrical potential. The electrical potential increases rapidly with a decreasing rate for both membranes. This rapid increase is associated with adsorption of water at the membrane surface, increasing protonic defect concentration and diffusion of protonic defects into the membrane down its

concentration gradient, as the concentration gradient approaches the balance, the potential difference decreases.

The electrical potential of BCY10 reaches its maximum level faster than the electrical potential of BCY20 (~100 s for BCY20 and ~75 s for BCY10, see Figure 4.4). This might be due to faster protonic defect formation on the BCY10 membrane surface or faster diffusion coefficients. The difference in the magnitude of measured electrical potentials might be attributed to the difference in concentration of protonic defects at the membrane surfaces, physical properties of membranes (e.g. thickness) and water concentration in the feed gas as it was also observed by Kee *et al* [110]. Kee *et al* [110] increased water concentration from 1% to 2% in hydrogen containing environment and observed an increase in electrical potential from 25 mV to 50 mV. Similar study is also done by Vollestad *et al* [111]. They obtained electrical potential profile within the 20 mole% yttrium–doped barium zirconate membrane and predicted the electrical potential using Gauss law instead of the electro neutrality condition. They used 2% water concentration in the feed side and obtained about 20 mV potential difference relative to the permeate side by using a two chamber reactor (they used inert gas in the permeate side). The magnitudes of electrical potential obtained in this study are in similar range with those reported in literature.

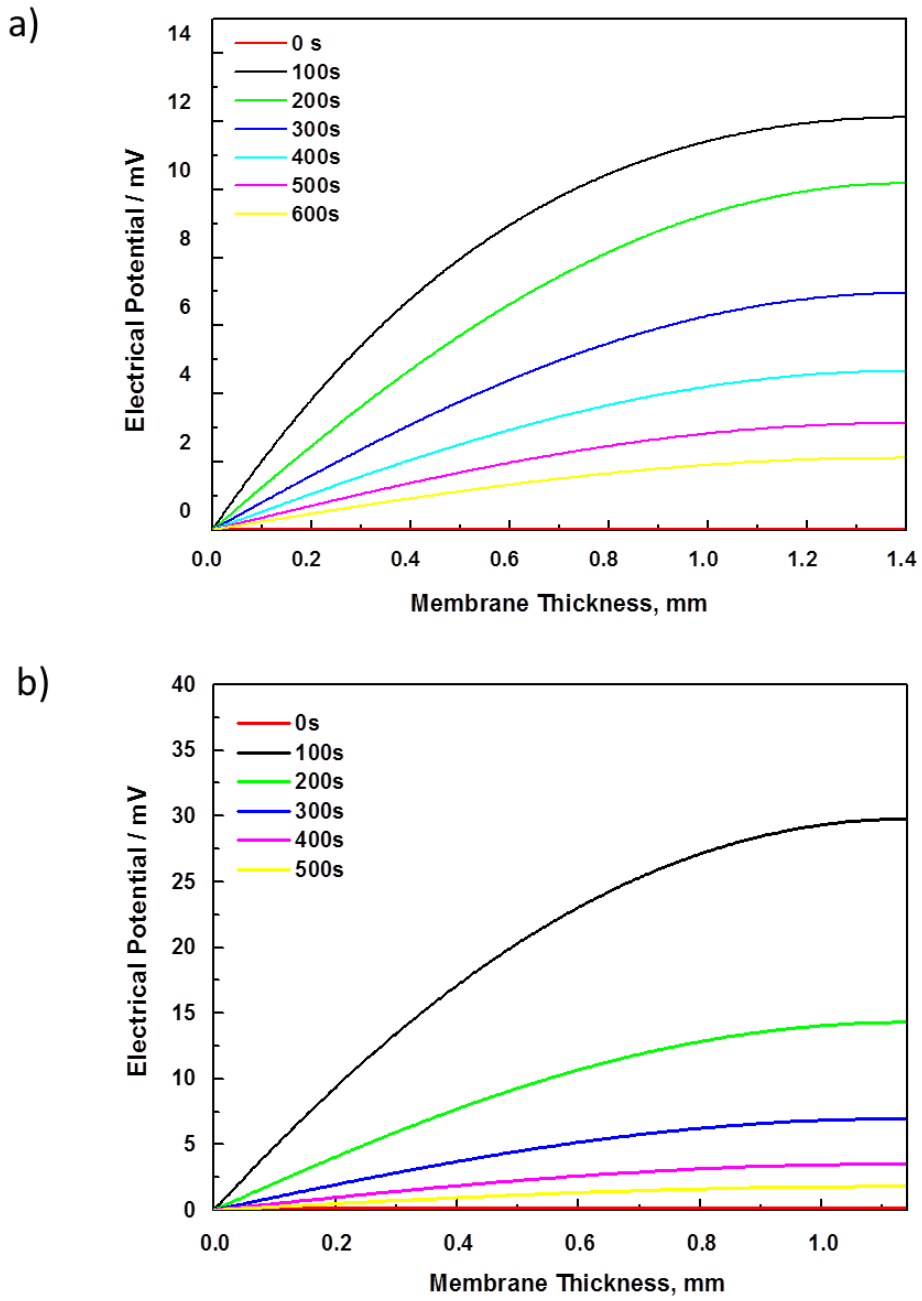

Figure 4.5: The electrical potential difference profiles upon hydration for different periods within the membranes. (X=0 represents "exposed side of the membrane", x=L mm represents, "isolated side of the membrane", L=membrane thickness.) **a)** BCY20. **b)** BCY10. The profiles are obtained as a function of time by solving Equations 4.21 and 4.23 which relate the concentration distribution of species to the electric potential.

4.4.2 The Diffusion Coefficients of Defects

The model mentioned above is used to predict chemical diffusion coefficients of $OH_O^{\bullet}$ and $V_O^{\bullet\bullet}$. The predicted values of chemical diffusion coefficients are presented in Table 4.2. The initial values are assumed based on the work by Kreuer *et al* [15] and set the same for both BCY20 and BCY10. The diffusion coefficients of $OH_O^{\bullet}$ and $V_O^{\bullet\bullet}$ are calculated using the Nernst–Planck equation with the boundary conditions, the remaining species concentration gradient is calculated using the electro neutrality condition. As previously discussed in *Section 4.4.*1 the amount of protonic defects at the interface increases and diffuses rapidly at the beginning when the membrane is exposed to humid atmosphere by water dissolution and occupation of oxygen vacancies. The diffusion coefficients of protonic defects are found to be greater than diffusion coefficients of oxygen vacancies for both membranes which is in agreement with Oishi *et al* [91] and Kreuer *et al* [14]. Oishi *et al* [91] found protonic diffusion coefficient value higher than oxygen vacancy diffusion coefficient from their conductivity measurements for BCY10 membrane.

Table 4-2: Fitted chemical diffusion coefficients calculated from the model at 700°C.

Parameter	**BCY20** (cm^2/s)	**BCY10** (cm^2/s)
$D_{V_O^{\bullet\bullet}}$	1.58×10^{-5}	1.27×10^{-5}
$D_{OH_O^{\bullet}}$	3.83×10^{-5}	6.2×10^{-5}

The diffusion coefficient of protonic defects for BCY20 membrane at low temperatures, between 50 °C and 350 °C was experimentally determined by Kreuer *et al* [15]. Their result depicted an increase in diffusion coefficient of protonic defects from 10^{-10} to 10^{-8} cm^2/s as the temperature rose from 50 °C to 350 °C. Additionally, the diffusion coefficient of oxygen vacancy for BCY10 at 700 °C has been reported [92] as $D_{V_O^{\bullet\bullet}} = 5 \times 10^{-5} cm^2/s$ which is in agreement with the findings in this study. The diffusion coefficients are compared with literature as shown in Figure 4.6 which is mainly obtained from electrical conductivity measurements [86, 91-93]. Although, the data presented in Figure 4.6 is for BCY10 (due to the fact that BCY10 has been commonly studied in the literature), the diffusion coefficients of defects for BCY20 is close to literature values of BCY10. Also, the diffusion coefficients of

defects for BCY10 are in good agreement with literature within the accuracy of data. The small scatter in data in Figure 4.6 could be due to the techniques that are used to obtain diffusion coefficients.

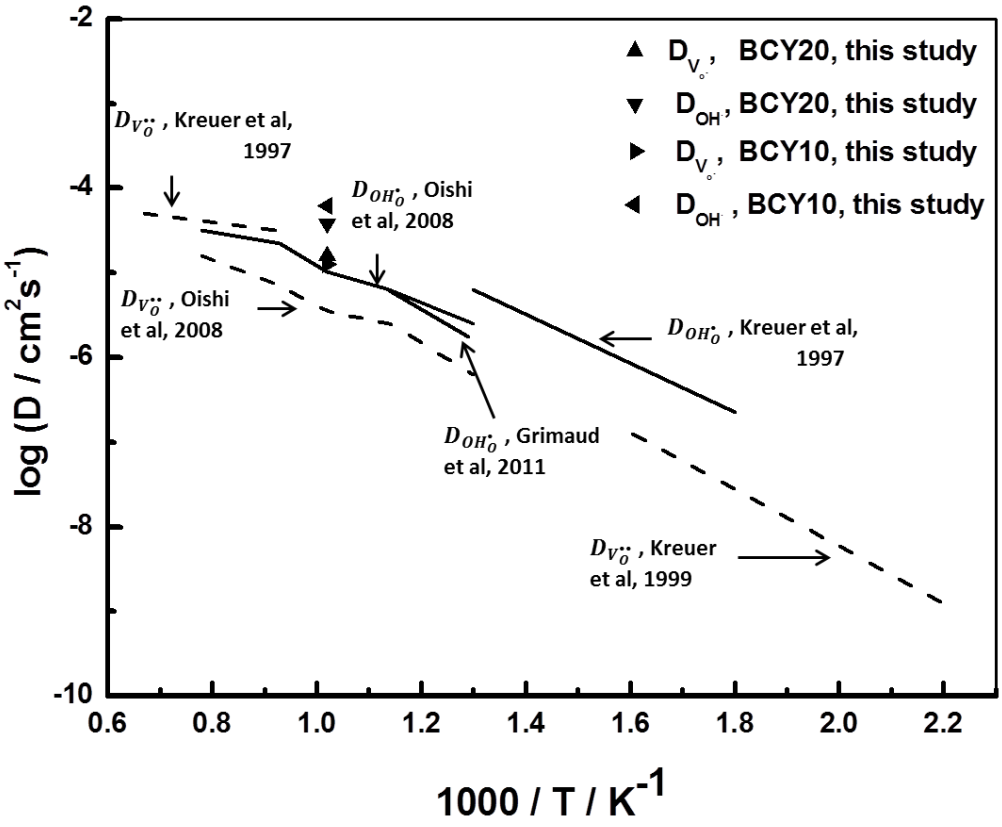

Figure 4.6: The comparison of diffusion coefficients of protonic defects and oxygen vacancies with the literature. All the literature data presents diffusion coefficients for $BaCe_{0.9}Y_{0.1}O_{3-\delta}$ (BCY10), the diffusion coefficients determined in this study are for both $BaCe_{0.8}Y_{0.2}O_{3-\delta}$ (BCY20) and BCY10.

Coors and Swartzlander [20] measured partial conductivities of two species ($OH_O^{\bullet}$ and $V_O^{\bullet\bullet}$) derived from total conductivity and used Kreuer`s ambipolar steam diffusivity model which relates partial ionic conductivities and diffusion coefficients. Their results suggest that the diffusion coefficients of $OH_O^{\bullet}$ and $V_O^{\bullet\bullet}$ for BCY10 can be calculated using $D_{V_O^{\bullet\bullet}}=3.628\times10^{-3}\exp\left(\frac{-0.552\ eV}{k_B\times T}\right)$ cm^2/s and $D_{OH_O^{\bullet}} = 7.74\times10^{-4}exp\left(\frac{-0.332\ eV}{k_B\times T}\right)$ cm^2/s. The exponential factor for 700 °C is 1.38×10^{-3}. Thus, the diffusion coefficient values at 700 °C can

be calculated as $D_{V_O^{\bullet\bullet}} = 5 \times 10^{-6}\, cm^2/s$ and $D_{OH_O^{\bullet}} = 1.7 \times 10^{-6}\, cm^2/s$, respectively. They found oxygen vacancy diffusion coefficient higher than protonic defect diffusion coefficient. The diffusion coefficients calculated in the current study shows that protonic defects diffuse faster than oxygen vacancies contradictory to the results of Coors and Swartzlander [20]. This difference could be owing to the techniques. They used dilatometry (to determine degree of hydration) and impedance spectroscopy (i.e. total conductivity can vary with time in wet atmosphere due to water adsorption, deconvolution of impedance spectra).

The diffusion coefficients of oxygen vacancy and protonic defect in this study are slightly higher than the values observed in literature (Figure 4.6). This difference might be owing to grain boundaries. It was reported that water diffuse faster in the grain boundaries than bulk [112]. However, the presence of grain boundaries in the conductivity measurements tends to decrease the conductivity of the membrane. During hydration, the bulk conductivity remains unchanged; but the grain boundary conductivity decreases due to an increase in grain boundary resistance (Grain boundary resistance increases due to depletion in oxygen vacancy concentration in that region. Oxygen vacancy concentration depletion is more severe than protonic defect concentration depletion due to the difference in the effective charges). Therefore, the total conductivity decreases (total conductivity = bulk + grain boundary).

The report on the role on grain boundaries on the diffusivity of water [112] which in turn relates to conductivity is quite recent, this explanation may not be considered by some of the studies reported in Figure 4.6 [86, 91, 93, 113]. Most of those values in literature were derived from the conductivity data (no correction for grain boundary resistance in the total resistance) which were measured as a function of temperature and partial pressure of oxygen and water, thus it is possible that they could underestimate diffusion coefficients of defects.

In addition, the assumptions associated with the model (e.g. strict electro neutrality condition, fast surface reaction kinetics) in the current study and errors in mathematical calculations can play a role in the deviation between diffusion coefficients obtained in this study compared with literature. However, another possibility might be that, the thermodynamic values (hydration enthalpy and entropy) are taken from literature measured and given for BCY10 membrane used for determination of the equilibrium constant. The same thermodynamic

values were used for BCY20 based on the study by Kreuer [86] that reported that doping level has a weak effect on hydration thermodynamics.

The model in this study considered only ambipolar transport of water (protons and oxygen vacancies). In reality, this may not be the case, especially under fuel cell operating conditions. In hydrogen/oxygen containing environment, there will be contribution of holes and electrons along with defect transport. Moreover, the counter and/or simultaneous diffusion defects could affect the apparent water flux, thus diffusion coefficients of defects. The data in this study and literature does not account for third defect species.

4.4.3 The Concentration Distributions of Defects within the Membranes

Figure 4.7 displays concentration distributions of $OH_O^{\bullet}$ and $V_O^{\bullet\bullet}$ during hydration for different periods across the membranes predicted using the model by solving mass conservation equations computationally. Defect concentrations vary non–linearly along the membrane thicknesses with time. The concentration profiles of $OH_O^{\bullet}$ and $V_O^{\bullet\bullet}$ have an opposite trend at the surface of both the membranes. The $V_O^{\bullet\bullet}$ concentration decreases at the hydration surface as the concentration of $OH_O^{\bullet}$ increases at this surface. This is expected since oxygen vacancies are filled with protons at the surface.

As can be seen from both the calculated data and schematic that the concentration changes of oxygen vacancy and protonic defect is asymmetric. This could be also easily seen from lines next to the schematic. The schematic represents the concentration of protonic defects and oxygen vacancies change with time and thickness through the membranes. The lines on the edges present increase or decrease in concentrations, both defects are transported down their concentration gradients.

In addition, the oxygen vacancy concentration distribution does not show a large concentration gradient between surfaces and bulk unlike protonic defect concentration. This could be because of the stoichiometric ratios. The concentration of $OH_O^{\bullet}$ exhibits a rapid increase at the hydration surface with the introduction of water into the reactor chamber

asserting that the formation of protonic defects is a very fast process. This is confirmed with a concentration versus time analysis. As seen from Figure 4.7 that protonic defect concentration increases fast on the exposed surface at 50 s and then continues increasing with a slowing rate. The concentration gradients disappear with time, which indicates that the membrane is completely hydrated. BCY20 has higher protonic defect concentration on the exposed surface than BCY10. This is due to higher availability of oxygen vacancy on the BCY20 surface than BCY10.

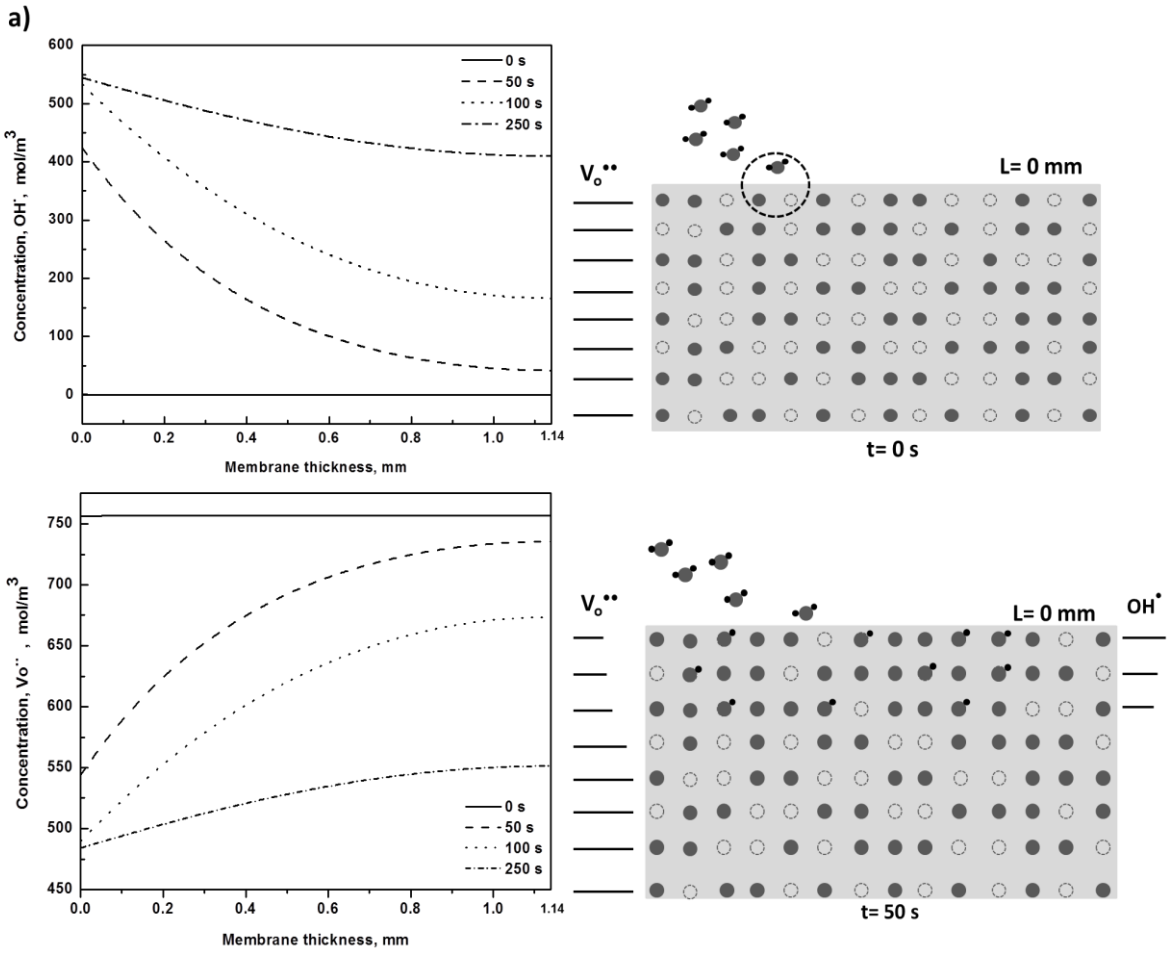

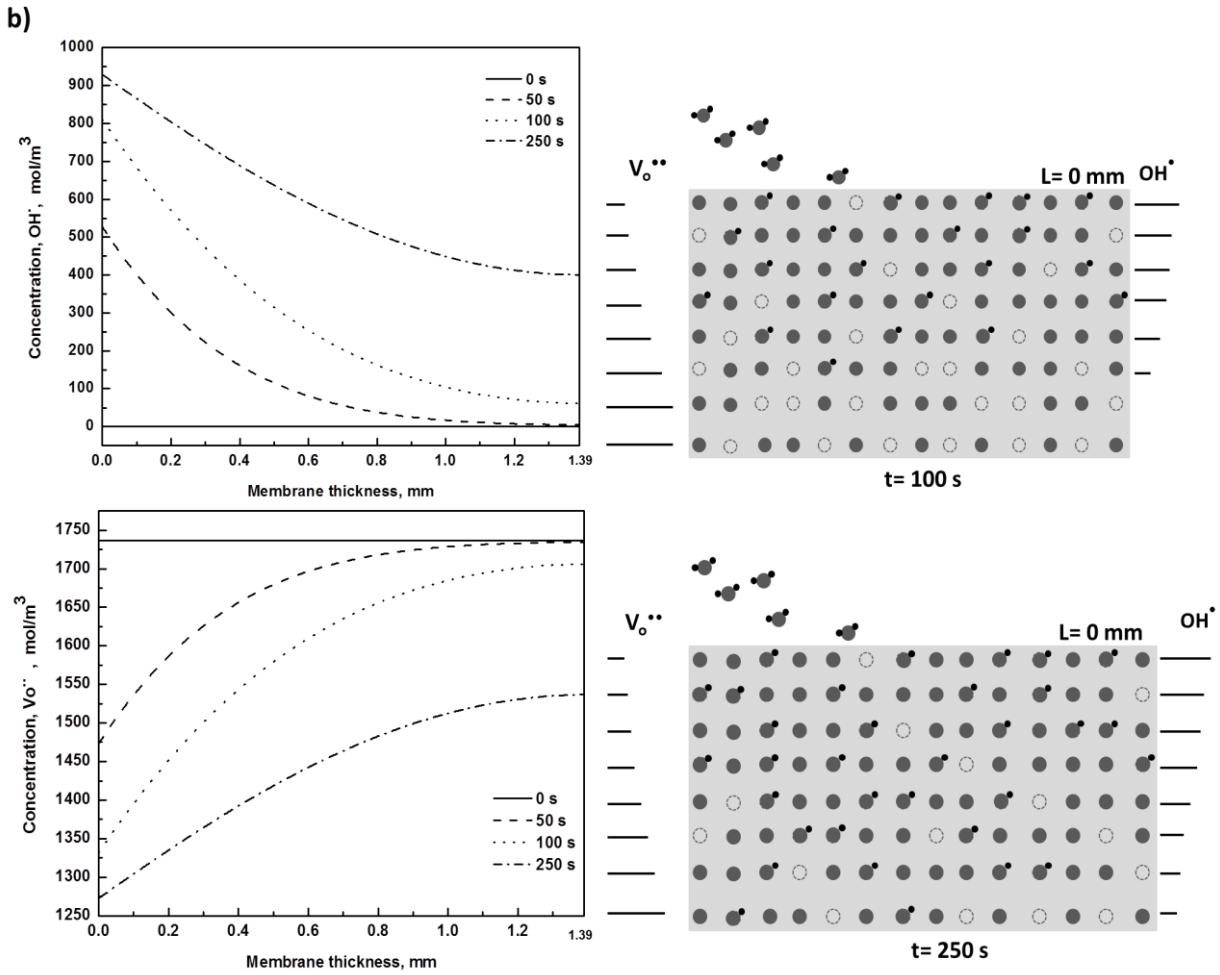

Figure 4.7: Concentration distributions of protonic defects and oxygen vacancies within the BCY membranes for different periods upon hydration, **a)** BCY10 and **b)** BCY20, respectively. The schematic on the right represent the distribution of defects within the membranes to aid visualisation of graphs. The lines on the edges represent the concentration changes of defects. (•) represents protons, (◌) represents oxygen vacancy, and (●) represents lattice oxygen. Water (•●•) incorporates into the membrane from the exposed surface, then protons diffuse towards to isolated surface and the oxygen vacancies diffuse towards to exposed surface.

4.5 Summary

A direct simple method is developed to calculate concentration distributions of $V_O^{\bullet\bullet}$ and $OH_O^{\bullet}$ within the BCY membranes and extract the diffusion coefficients of defects from behaviour of the membrane during hydration. The protonic defect diffusion coefficient shows higher value

than oxygen vacancy diffusion coefficient which is in agreement with the literature showing that the model for hydration of the membrane is valid. However, the values are one order of magnitude higher than those reported in the literature which might be due to using different paths to extract diffusion coefficients. This study introduces a novel approach and groundwork to develop more complex models to those in literature. It also presents new data for the BCY membrane materials used during hydration/dehydration at an elevated temperature and may be useful for different physical membrane configurations for future applications.

Chapter 5
Water Permeation and Water Gas Shift Reaction through BCY20 Membrane Modified with Platinum

5.1 Introduction

The water permeation behaviour of BCY20 membrane which is modified with platinum (as catalyst/electrode) is studied in the temperature range of 500–800 °C. For practical applications, it is important to understand the mechanism of water incorporation and water evolution from the membrane. Both these phenomena depend on the active surface sites that are required for water disassociation/incorporation into the membrane. Therefore, the membrane surfaces are modified in different configurations. This may be beneficial in terms of designing electrode structures for fuel cells to be operated with simultaneous water permeation.

The feasibility of utilising permeated water in water gas shift reaction is further investigated in mono–membrane reactor. This process involves water splitting on the feed side followed by water transport across the membrane to react with carbon monoxide on the permeate side. Water permeation coupled with water–gas shift reaction is carried out by using carbon monoxide on one side and water vapour on another side of membrane as shown in Figure 5.1. Permeated water reacts with carbon monoxide to generate carbon dioxide and hydrogen given by the equation:

Water gas shift reaction: $CO + H_2O \leftrightarrow CO_2 + H_2$ $\Delta H_{298K} = -41\ kJ/mol$ 5. 1

The feasibility of water–gas shift reaction through water permeation has not been reported in literature. Therefore, water permeation coupled with water–gas shift reaction is studied in this chapter. The role of catalytic surface modification on water–gas shift reaction in the membrane reactor is investigated along with the influence of reducing gas (i.e. carbon monoxide) on the permeate side as a driving force for water permeation.

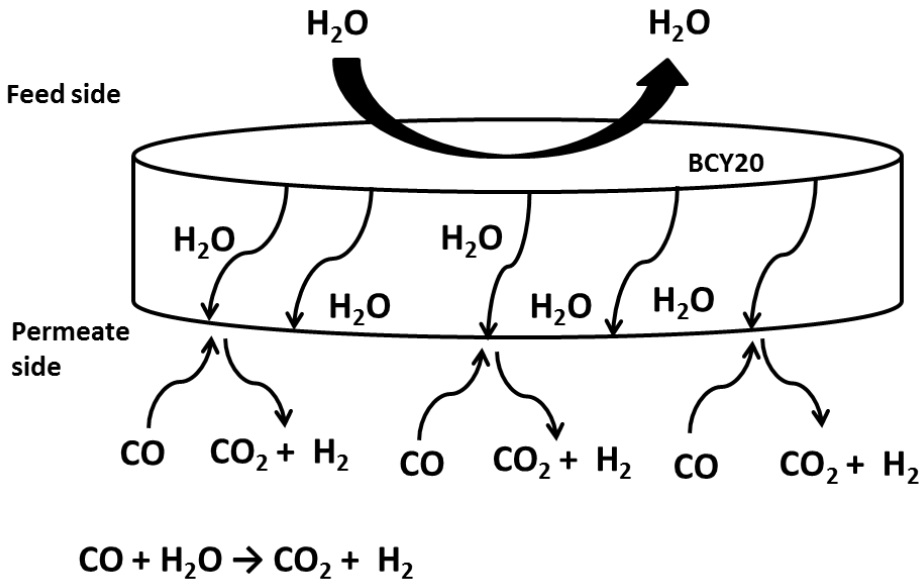

Figure 5.1: Schematic diagram of membrane based water permeation coupled with water–gas shift reaction. Water permeates from feed side to permeate side and reacts with carbon monoxide to generate hydrogen and carbon dioxide.

The stability of the BCY20 membranes after their use in water permeation coupled with water–gas shift reaction is examined by post operation analysis. This will suggest whether the membrane is stable under harsh environment (i.e. carbon dioxide and water) and water permeation could facilitate carbon removal formed by carbon monoxide disproportionation. The water permeation coupled with water–gas shift reaction experiments are typically carried

out for more than 45 hrs. The membranes are characterised using different analytical techniques such as x–ray diffraction (XRD), scanning electron microscopy (SEM) and energy dispersive x–ray spectroscopy (EDXS).

5.2 Characterisation of BCY20 Membrane and Platinum Layer

5.2.1 X–Ray Diffraction (XRD)

XRD technique is used to identify the formation of the perovskite structure in BCY20 membrane by comparing the data with the references and the International Centre for Diffraction Data (ICDD) database. The x–ray diffraction pattern (CuKα, 1.5406 A°) of the sintered BCY20 pellets is shown in Figure 5.2. The match with the standard BCY20 rhombohedral structure is excellent (ICDD-01-070-6750) [19, 72, 114].

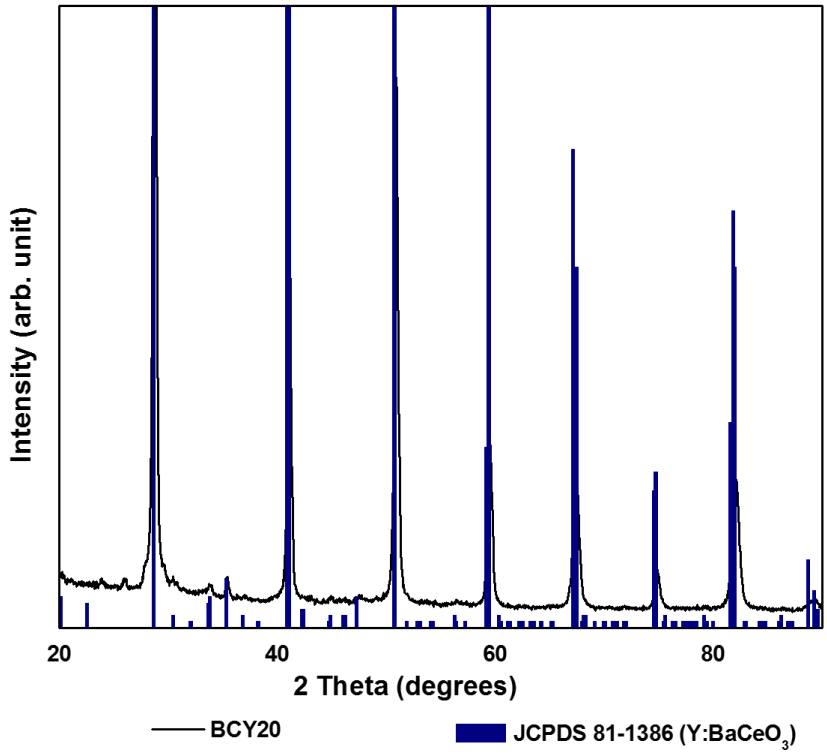

Figure 5.2: XRD patterns of BCY20 pellets in comparison with the reference data.

The peaks in Figure 5.2 indicate a single phase perovskite structure. According to the XRD results, the configuration determined in this work is rhombohedral. In the case of doping more than 20 mole % Y^{3+} , the main perovskite XRD peaks could split and Y_2O_3 peaks would appear indicating that the sample has a single phase tetragonal perovskite–type structure [115]. However, no Y_2O_3 peaks are observed as secondary phases in this study indicating that the sample contains 20 mol% or less Y–dopant concentration. Figure 5.2 clearly demonstrates that the sample has peaks with low intensity at 2θ values: 24 and 27°. The search in crystallographic database revealed that the peaks can be attributed to $BaCO_3$ impurity in the sample. $BaCO_3$ decomposes into BaO and CO_2 at 1300°C. The sample was sintered at 1450°C for 12 hrs, thus it is expected that BaO enters the perovskite structure and forms XRD patters of BCY20. Similar low intensity $BaCO_3$ peaks in the diffraction pattern of BCY10 was also reported in literature[116]. Figure 5.2 displays that the intense peaks of Y_2O_3 and CeO_2 are not present.

5.2.2 Scanning Electron Microscopy (SEM)

The SEM analysis is carried out for further characterisation of the BCY20 membrane morphology in terms of microstructure, sintering conditions, density and pore sizes. The SEM analysis is employed under a vacuum atmosphere with various magnifications.

Figure 5.3a and Figure 5.3b illustrates the surface and cross section SEM images of the BCY20 membrane sintered at 1450 °C for 12 hrs. As can be seen the microstructure of the surface is clear, dense (shows very few pores) and crack free. This is consistent with the high relative density which is 95% of theoretical density (6.154 g/cm^3 [72]). The geometric dimensions and mass are used to estimate the relative density of the membrane. The dense layer is connected with grain boundaries which can clearly be seen from the image in Figure 5.3a. The grain sizes are in the range of ca 1 µm to *ca* 2 µm. As shown in Figure 5.3b the membrane is completely dense. BaO evaporation and small $Ce_{1-x}Y_xO_2$ peaks are reported in the literature [117] due to the high sintering temperature above 1500 °C. This phenomenon is not observed in this study (in the XRD and SEM analysis) even though the membrane is sintered at 1450 °C.

The platinum layer deposited on the BCY20 membrane surface (after sintering) is illustrated in Figure 5.3c. It can be observed that platinum is well distributed with homogen pores on the membrane surface. There is no uncovered membrane surface observed. Figure 5.3d exhibits the cross section image of BCY20 and platinum layer. The BCY20 and platinum seems to be well connected. The thickness of porous platinum layer is found about 5 μm which is determined using the SEM analysis is shown in Figure 5.3d. The average surface loading for catalytically modified membrane surfaces is approximately 4.1 mg/cm^{-2}. The loading amount is obtained by measuring the mass of unmodified BCY20 membrane and modified BCY20 membrane with platinum to find the amount of platinum deposited on the membrane. This value is divided by the surface area of catalyst coated on the membrane surface. The porosity of platinum layer is also estimated. The platinum layer is about %61 porous under the current condition of the study. (See Appendix J for detailed calculation for the amount of deposited platinum onto membrane and estimation of the porosity of platinum layer.) The porosity calculation is done by assuming that platinum is pure and dense. Figure 5.3c shows distribution of lots of small voids. It is difficult to compare calculated porosity value with Figure 5.3c due to high magnification of SEM image and approximations in calculation.

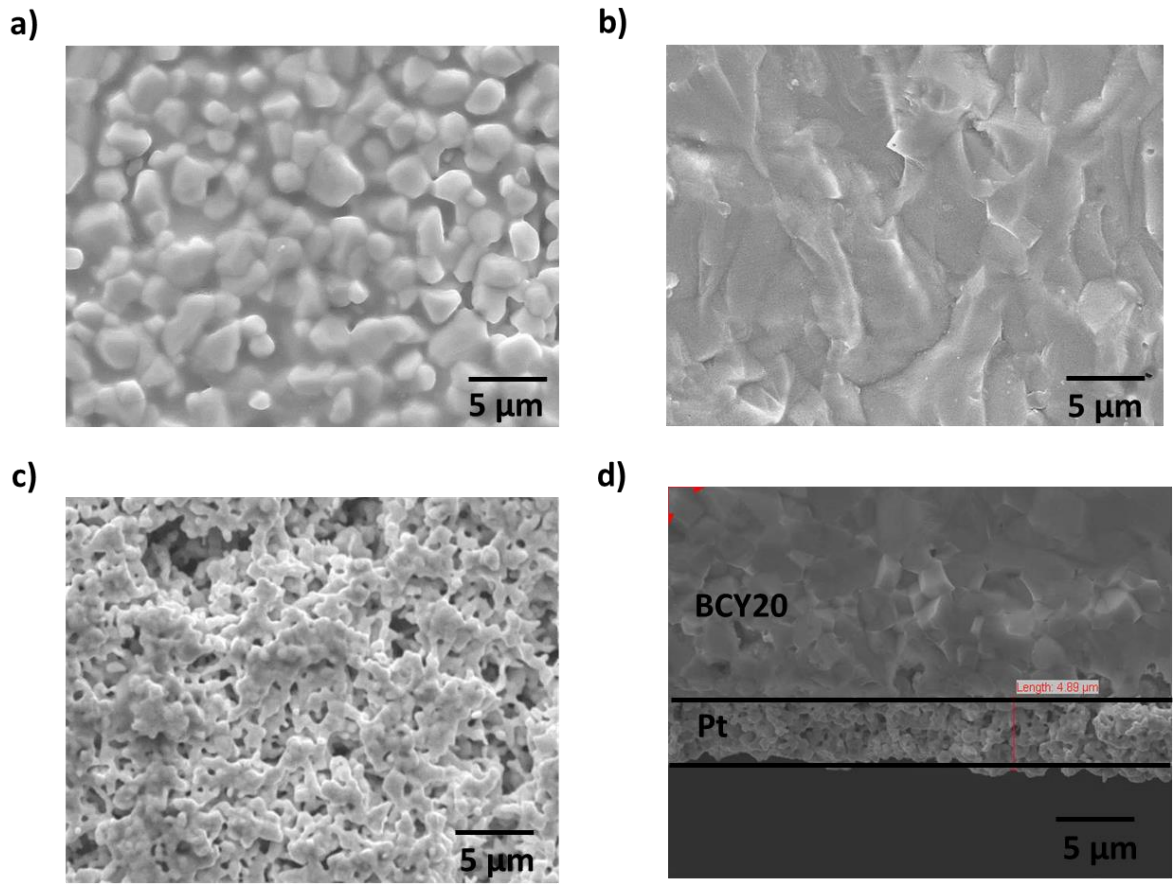

Figure 5.3: a) The surface of fresh BCY20 membrane (after sintering at 1450 °C for 12 hrs), **b)** cross section SEM image of BCY20. **c)** The surface image of platinum layer (after sintering at 980 °C for 10 min) and **d)** cross section of SEM image of the porous platinum layer. Platinum layer thickness is about 5 µm.

5.2.3 Energy Dispersive X–Ray Spectroscopy (EDXS)

The semi–quantitative EDXS technique is employed in order to investigate the composition of the BCY20 membrane in addition to other characterisation techniques. The data is collected in the form of weight and atomic percentages of each element for three times randomly and the result is presented in Figure 5.4. The detected weight percentages are about 22.07 ± 4.34% Oxygen, 5.53 ± 1.91% Yttrium, 40.21 ± 4.96% Barium and 32.19 ± 4.63% Cerium.

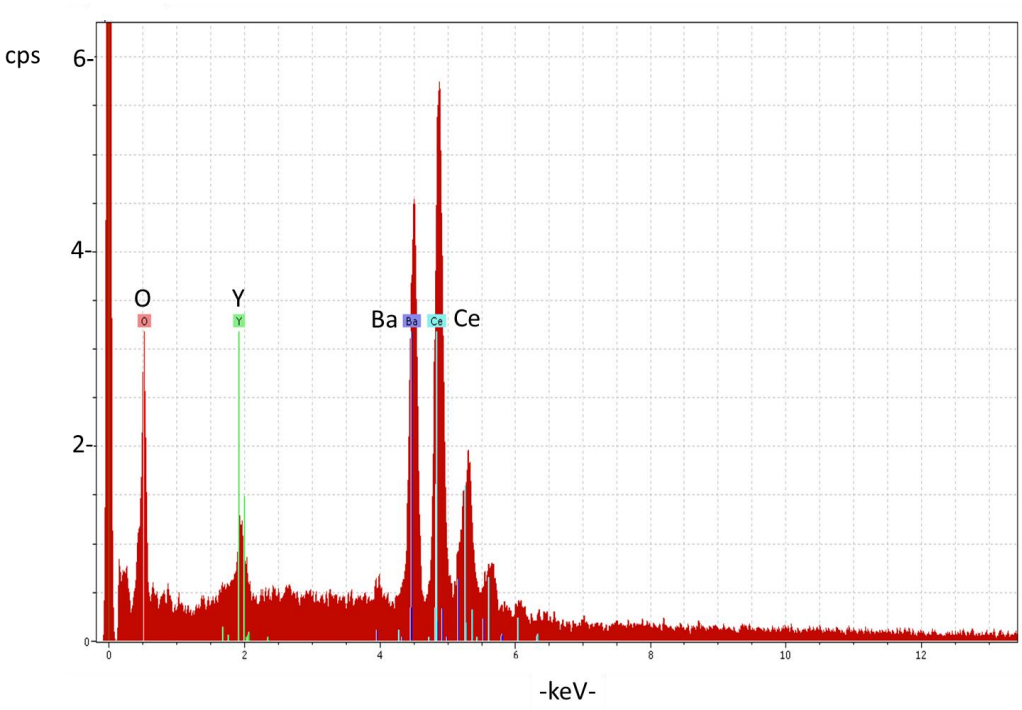

Figure 5.4: The EDXS scan of BCY20 pellet surface

In order to obtain the stoichiometric ratios from the EDXS data, the moles of each element should be calculated. The mole of each element in the membrane is obtained by dividing the weight percent of each element by its molecular weight. By choosing barium as a basis element, the amounts of elements are divided by the amount of moles of barium present and the calculated stoichiometric ratios are presented in Table 5.1.

Table 5-1: Calculated stoichiometric ratios for BCY20 from the EDXS results.

Membrane	**Condition**	**Approximate atom (%)**			
		Ba	**Ce**	**Y**	**O**
BCY20	bare	14.9 ± 1.8	11.7 ± 1.7	3.2 ± 0.9	70.2 ± 13.9
BCY20	bare	**Stoichiometric ratio**			
		Ba	**Ce**	**Y**	
		1	0.78	0.21	

The calculated and the theoretical stoichiometric ratios are similar. This also confirms that the BCY20 membranes used in this study have no impurities.

5.3 Water Permeation through BCY20 Membrane Modified with Platinum

The water permeation behaviour of the BCY20 membrane modified with platinum in different membrane configurations (no platinum, one or both surfaces modified with platinum) is studied as a function of temperature is described in *Section 3.1.3*. The main focus is to investigate the effect of surface modification on surface reactions and water permeation. Under the current experimental conditions, only ambipolar diffusion of protonic defects and oxygen vacancies prevail, therefore the electronic defects are not considered. The feed side inlet of the membrane is fed with 3% H_2O in nitrogen and the permeate side inlet is fed with dry helium.

In the membrane, the water permeation process can be assumed to take place in the following successive steps; adsorption of water from the gas phase to the membrane surface (Equation 5.2), water disassociation (Equation 5.3), diffusion of protonic defects within the membrane (Equation 5.4), water recombination (incorporation of hydroxide groups, Equation 5.5) and desorption of water (Equation 5.6) from the surface of the membrane.

$$H_2O_{(g)} \leftrightarrow H_2O_{(ads)} \quad 5.2$$

$$H_2O_{(ads)} + V_o^{\bullet\bullet} + O_o^x \leftrightarrow 2OH_o^{\bullet} \quad 5.3$$

$$OH_o^{\bullet} + O_o^x \leftrightarrow O_o^x + OH_o^{\bullet} \quad 5.4$$

$$2OH_o^{\bullet} \leftrightarrow O_o^x + V_o^{\bullet\bullet} + H_2O_{(ads)} \quad 5.5$$

$$H_2O_{(ads)} \leftrightarrow H_2O_{(g)} \quad 5.6$$

Figure 5.5 shows the leakage corrected water permeation flux for membrane surfaces modified with platinum. Pt|BCY20 represents the membrane configuration where the feed side of the membrane is modified with platinum and the permeate side is bare. Similarly, Pt|BCY20|Pt represents the membrane configuration where the both sides of the membrane are modified with platinum. BCY20 represents the membrane configuration of bare membrane with no modification while BCY20|Pt represents the membrane configuration where only permeate side of the membrane is modified with platinum. Figure 5.5 exhibits that surface kinetics have an effect on water permeation.

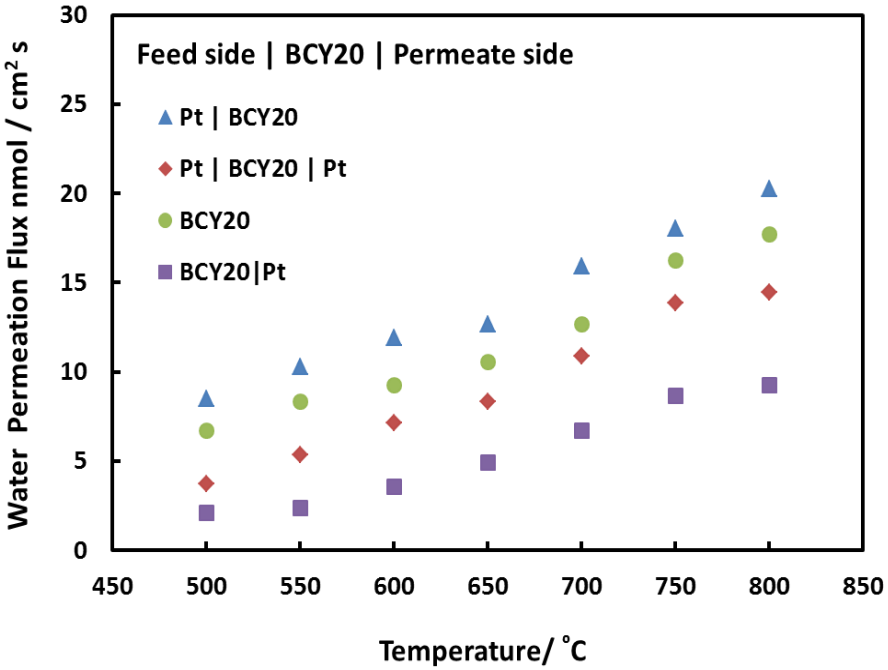

Figure 5.5: Molar fluxes of water permeated across the BCY20 membrane for four different membrane configurations (platinum is only on the feed side, platinum on both sides, without any platinum and platinum is only on the permeate side) at the temperature range from 500 °C to 800 °C. (Feed side inlet gas concentration: 3% H_2O in nitrogen; permeate side inlet gas concentration: dry helium, flow rates of gases are 100 ml/min). Platinum surfaces are sintered at 980 °C for 10 min, is ~5 µm thick and ~61% porous.

The influence of platinum on the surface offers an important starting point to the understanding of surface mechanism of water permeation through the membrane. It can be

observed from Figure 5.5 that the water permeation increases as the temperature rises from 500 °C to 800 °C. This suggests that the process is thermally activated and temperature plays an important role on surface reaction rates and/or bulk diffusion of protons and oxygen vacancies possibly through an increase in diffusion coefficients. 700 °C is an optimum temperature for operation of intermediate temperature solid oxide fuel cell and water permeation [3, 51].

The application of platinum on the feed side surface of the membrane slightly increases water permeation (Figure 5.5). A water permeation flux of *ca* 13 nmol/cm^{2}s is obtained at 700 °C for unmodified BCY20 membrane whereas a water permeation flux of *ca* 17 nmol/cm^{2}s is obtained for Pt|BCY20 membrane under similar operating conditions. The surface reaction on the feed side of the membrane composes of multiple steps such as adsorption of water onto the membrane surface, dissociation of water and incorporation of hydroxyl groups and proton into the membrane (Equation 5.3). All these steps contribute to the permeation in the same direction. This implies that platinum coating on the feed side surface of the membrane enhances the combined rate of water adsorption, dissociation and incorporation into the membrane.

It is known that [118, 119] surface coatings such as platinum and silver accelerates oxygen exchange kinetics strongly and lowers the activation energy of oxygen dissociation on its surface compared to membrane surface without metallic coating. Similarly, another study by Yu *et al* [120] showed that platinum is highly catalytic for incorporation of protons into the bulk of Fe–doped $SrTiO_3$ membrane and Mather *et al* [121] reported an increase in hydrogen permeation for feed side platinum coated SCYb ($Sr_{0.97}Ce_{0.9}Yb_{0.1}O_{3-\delta}$) membrane. Also, Hancke *et al* [122] investigated the effect of platinum on the surface exchange rate of hydrogen. Their result showed that platinum slightly decreased activation energy for surface exchange of hydrogen and the authors suggested that either hydrogen dissociation or charge transfer is rate limiting for platinum coated BCY10 surface. Platinum (Pt[110]) dissociates water on its surface with an activation energy of 0.44 eV [123] whereas the BCY membrane dissociates water on its surface with an activation energy of ~ 0.54 eV [15]. Therefore it is speculated that, similar to the reports of oxygen and hydrogen dissociation and incorporation into membranes, in this study platinum can also accelerate the dissociation and incorporation of water (as hydroxyl groups) into the membrane. As a result of that there is an increase in

concentration of hydroxyl groups on the feed side surface of the membrane. This would increase the concentration gradient of hydroxyl groups across the membrane, leading to high water permeation rate across the membrane.

This study (see *Section 4.4.2*) and literature suggests that the diffusion of protons across the membrane is faster than that of the oxygen vacancies [14, 91]. Increasing the concentration of hydroxide groups on the feed side membrane surface increases the protonic defects within the bulk of the membrane. This increases the rate of transport of protonic defects across the membrane which in turn increases the rate of transport of oxygen vacancies in the bulk of the membrane to maintain electro–neutrality. This is another speculation for the enhancement of water permeation rate observed in Figure 5.5 in the presence of platinum on the feed side surface.

The activation energy for the process of water permeation through Pt|BCY20 and BCY20 is calculated from Arrhenius plot (Figure 5.6). The calculated activation energies are 19.8±0.6 kJ/mol for Pt|BCY20 and 22.3±0.7 kJ/mol for bare BCY20. This indicates that platinum coating decreased the activation energy as compared to bare surface. As previously discussed the low activation energy of water dissociation on platinum surface enhances the water permeation rate through the membrane.

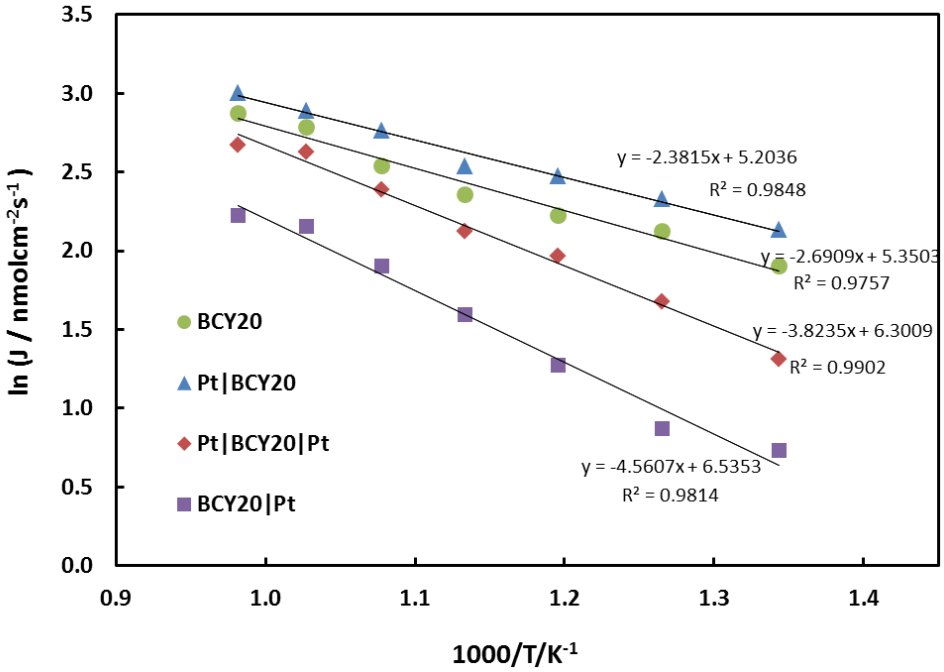

Figure 5.6: Arrhenius representation of water permeation for catalytically modified membrane surfaces. Water concentration is 3% in nitrogen on the feed side, helium is used on the permeate side.

Conversely, it is observed from Figure 5.5 that the rate of water permeation decreases when platinum is applied on the permeate side surface of the membrane and both the sides of the membrane as compared with the bare membrane. The water permeation flux is *ca* 11 nmol/cm^{2}s for Pt|BCY20|Pt and *ca* 7 nmol/cm^{2}s for BCY20|Pt membrane at 700 °C. This leads to the assumption that platinum is not catalytically active for water recombination or water desorption. The obtained activation energies (from Figure 5.6) for both membrane configurations were 31.8±1 kJ/mol and 37.9±1.1 kJ/mol, respectively.

Recombination of water is a reaction between proton and oxygen on the permeate side which may follow a different path than feed side. This is based on the observations in Figure 5.5 where the overall water permeation flux is decreased by the surface modifications on the permeate side. By assuming that surface morphology of the platinum layer is similar to the bare surface on the permeate side (since surface morphology affects active catalytic area), it can be speculated that platinum on the permeate side has a lower number of active sites for water recombination due to some site–blocking mechanism as compared to the bare membrane surface.

The formation of one O−H bond depends upon breaking another O−H bond and protons could exchange with partner hydroxyl atoms to form water on the permeate platinum surface. Thus, evolution of water on the permeate side relies on instantaneous recombination of protons and oxygen. The combination energy of water on the platinum surface has the same activation energy as water dissociation. But the recombination of two hydroxyl groups on the platinum surface with evolution of water can lead to the formation of adsorbed oxygen on the platinum surface. This adsorbed oxygen may limit the recombination of other hydroxyl groups to form water and as a consequence reduce the water evolution from the surface. This is not the case with bare membrane surface. It has been reported that [124] water desorption from platinum surface does not have simple kinetics, but rather have several paths, including OH recombination and O–surface coverage. However, it is not clear which step is the rate determining step.

Another possible explanation would be the slow kinetics of hydroxyl group desorption from the membrane surface to the platinum surface on the permeate side and low ionic conductivity of platinum. Hence, the effective electrochemical active area is reduced by dense part of platinum on the permeate side for water recombination. The water permeation rate will therefore be limited by surface recombination of hydroxyl groups in the case of platinum coated permeate side surface.

Alternatively there might be the existence of counter reaction which could give the impression of a decrease in water permeation. Instead of water permeation, platinum may catalyse hydrogen evolution from the system ($H_2O + V_o^{\bullet\bullet} + 2e' \rightarrow O_o^x + H_2$) [125]. However, it was difficult to determine the hydrogen leaving the membrane under the current experimental conditions since the difference in water flux should correspond to hydrogen evolution which is below the accuracy of mass spectrometer. Also, this reaction will lead to a decrease in the concentration of oxygen vacancies within the membrane, and hence the water permeation. Nonetheless, there was no reduction observed in water permeation over many hours.

The difference in the mechanism of water permeation between Pt|BCY20|Pt and BCY20|Pt membrane configurations cannot be distinguished easily. The difference in two cases may be

attributed to different amount, distribution and morphology of platinum deposited on the permeate side membrane surface.

The blocking effect is further investigated by using a dense platinum layer on the permeate side (Figure 5.7a) produced via pulsed laser deposition technique (Giessen, Germany). However, no conclusive result is obtained from these experiments due to the fact that the surface coverage area of platinum is smaller than the alumina tube diameter facing the membrane surface. In addition, examination of the membranes after the experiment exhibits that the dense platinum layer is deformed (Figure 5.7b and Figure 5.7c).

Platinum layer seems cracked in Figure 5.7b and 5.7c. This deformation of platinum layer could be attributed two reasons: water permeation or different thermal expansion coefficients of materials. In the case of water permeation, the amount of water that incorporated into the membrane on the feed side needs to come out on the permeate side due to chemical potential difference of water between surfaces. If dense platinum layer blocks water evolution, water may create a path by deforming platinum layer to evolve. In the second case, platinum and BCY20 have different thermal expansion coefficients: 9×10^{-6} K and $14\text{-}16\times10^{-6}$ K, respectively. Platinum may crack during temperature increase from room temperature to 700°C since it has lower thermal expansion coefficient than BCY20.

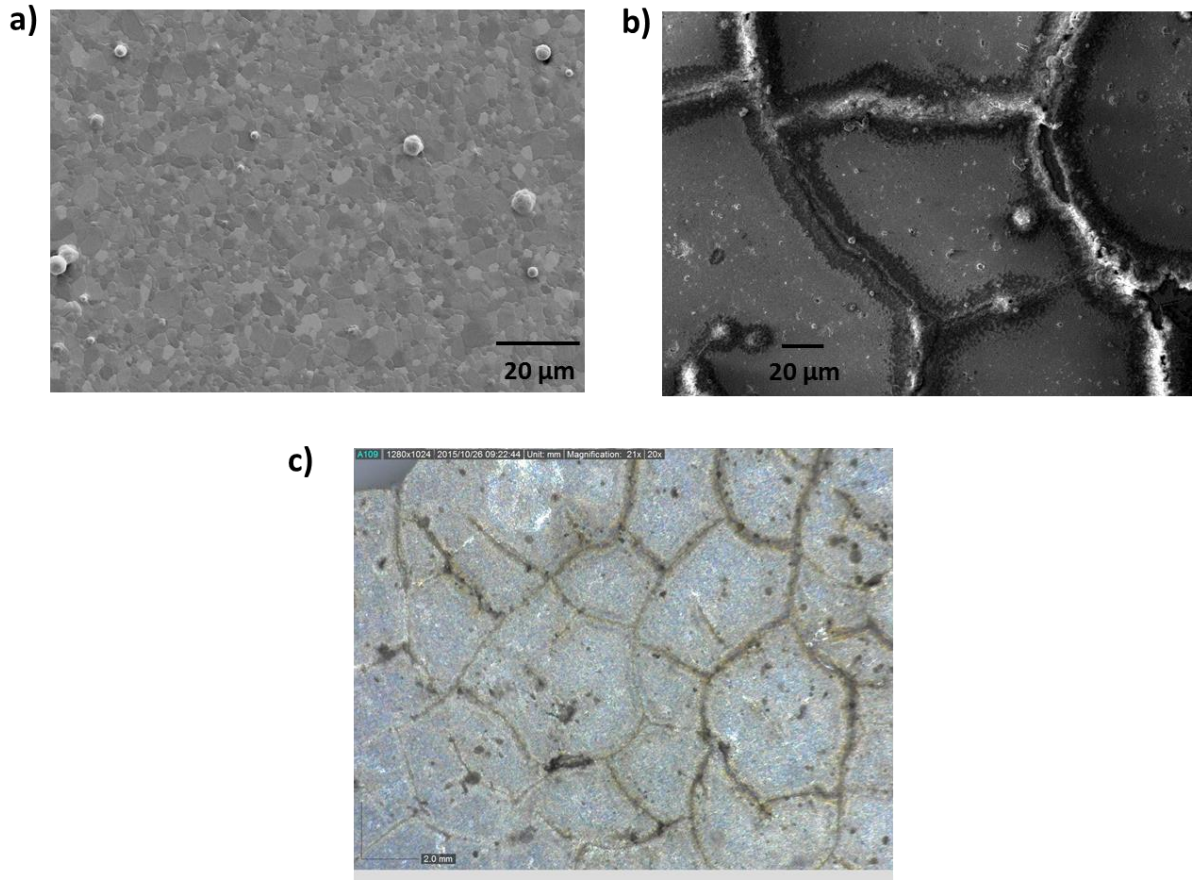

Figure 5.7: a) SEM image of dense platinum layer before the experiment. **b)** SEM image of platinum layer after the experiment. **c)** A photo of platinum layer after the experiment taken with the Dino-lite digital microscopy.

5.4 Membrane Based Water Gas Shift Reaction Coupled with Water Permeation through BCY20 Membrane Modified with Platinum

In order to determine the possibility for the use of BCY20 perovskite material (with and without catalytic surface modification, similar to *Section 5.3*) as a membrane in a reforming membrane reactor the following study is intended. The experimental design is done in a way that water splitting reaction takes place on one side of the membrane while water gas shift reaction takes place on the other side. The results are intended to provide information about the possibility of coupling these reactions together in a membrane reactor using BCY20 perovskite material. Additionally the stability of the membrane is studied before introducing it in the exothermic fuel cell with charge transfer reactions.

All the experiments are performed in three steps at 700 °C for over 45 hrs. The experimental details are given in *Section 3.1.4c*. In step one, helium and argon are introduced to permeate and feed side, respectively to flush the system of any residual and entrapped air. In step two, 3% H_2O in argon is introduced to the feed side and helium is fed to the permeate side to monitor water permeation. The carrier gas is switched from nitrogen to argon in this step (as compared with *Section 5.3*) as nitrogen and carbon monoxide have the same mass/charge ratio (m/z=28) which generates a problem of differentiating these gases in the mass spectroscopy i.e. if there are any leaks/bypass in the system. Finally, in step three, helium is switched to about 1% carbon monoxide in helium in the permeate side while the feed side gas is kept the same as 3% H_2O in argon.

The results are obtained by plotting the mole fraction of gases in the permeate side (ordinate) against time (abscissa), exemplified in Figure 5.8. To aid the discussion, these mole fractions are converted to production rates (nmol/cm^{2}s) using Equation 3.2. The performances of the membranes are compared in terms of the rate of product formation, particularly hydrogen. The rate of hydrogen formation is taken as a basis for water permeation in step three, since the only source for hydrogen is water in the system.

One limitation in the analysis could be an error in evaluation of carbon dioxide mole fractions on the permeate side. This error can arise due to a reaction between feed gas and membrane/sealant and/or carbon monoxide disproportionation (Equation 2.29). The limitation in the evaluation of carbon dioxide mole fraction is overcome by, subtracting the mole fraction of the lean carbon dioxide emission obtained in the absence of water–gas shift reaction, from the mole fraction of carbon dioxide obtained in the presence of water–gas shift reaction. This is given by the Equation 3.3 (*Section 3.1.4c*).

a) BCY20 Membrane

The mole fractions of outlet gas, including carbon monoxide, carbon dioxide, hydrogen, oxygen, water, argon and helium, on the permeate side of the bare BCY20 membrane are illustrated in Figure 5.8. As explained previously, during step one, helium is supplied to the permeate side whereas argon is supplied to the feed side so as to totally purge out any entrapped/adsorbed air from the membrane. An insignificant trace of argon detected in permeate side (<0.002 %) indicates that the membrane is well sealed.

In step two, 3% H_2O in argon is supplied to the feed side for water permeation studies. As seen in Figure 5.8b (step two) that after an initial increase water permeation reached a steady state of *ca* 9 nmol/cm^{2}s. The initial increase is attributed to the hydration of membrane for water permeation. The driving force for water permeation is the partial pressure difference between the surfaces.

In step three, about 1% carbon monoxide in helium is introduced to the permeate side of the membrane. An increase in oxygen and mass 28 peaks suggests that there is some residual air purged into the permeate side possible from the dead volume of the switching valve. The direct analysis of the results for water permeation coupled with water–gas shift reaction within the first 3 hrs of step three is difficult. This is due to the fact that wide possibilities of side reactions are envisioned within these 3 hrs. These involve reactions such as water–gas shift reaction, carbon monoxide oxidation and carbon monoxide disproportionation reaction.

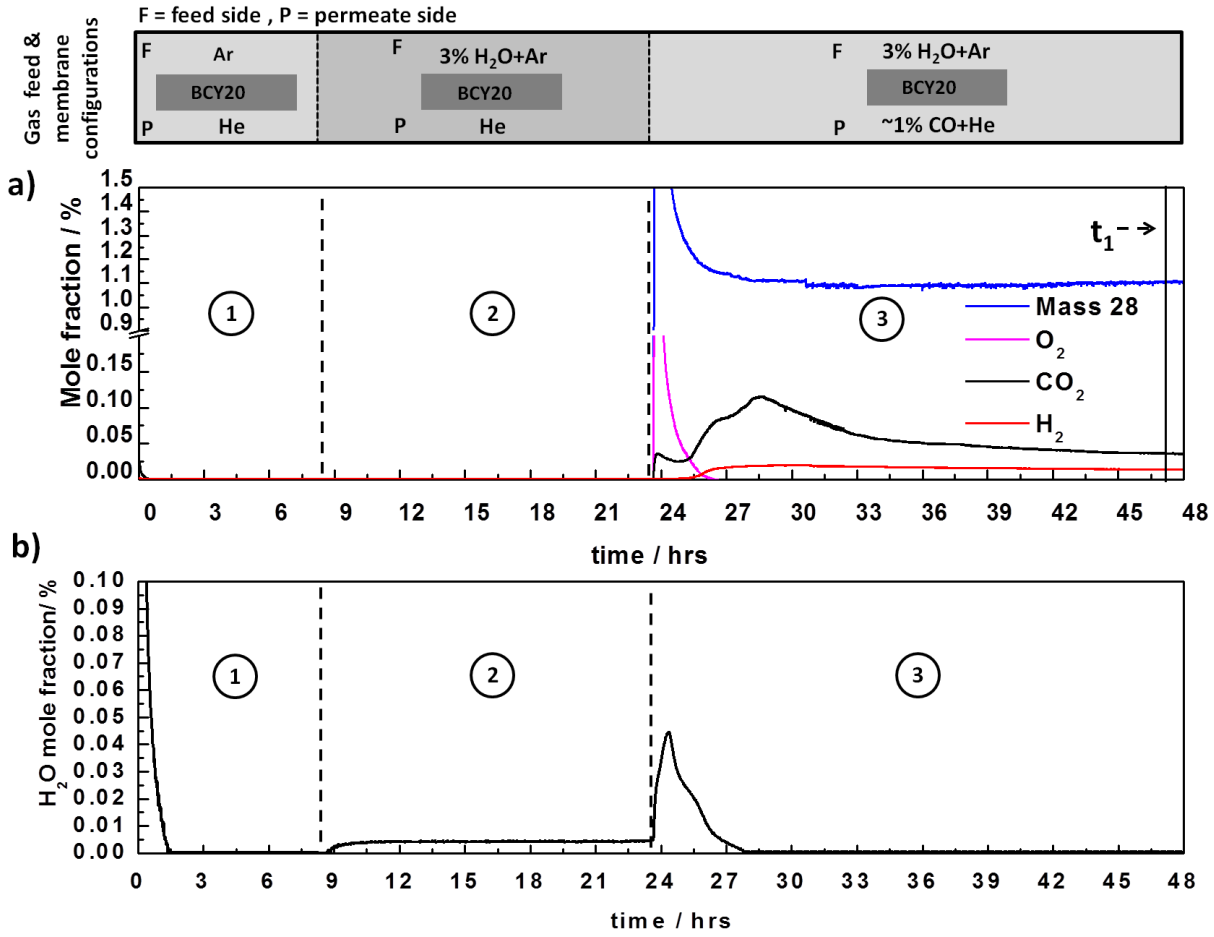

Figure 5.8: Permeate side outlet gas compositions for bare BCY20 membrane configuration at 700 °C (mass 28, oxygen, hydrogen and carbon dioxide). The flow rates of gases are 100 ml (STP)/min. During **step one:** permeate side inlet: He; feed side inlet: Ar. During **step two:** permeate side inlet: He; feed side inlet: 3% H_2O in Ar. During **step three:** permeate side inlet: 1% CO in He; feed side inlet: 3% H_2O in Ar. **a)** mass spectrometer data **b)** hygrometer data (water)

It is also observed from Figure 5.8a step three that there is a delay followed by a slow increase in hydrogen formation after the introduction of 1% carbon monoxide in helium on the permeate side of the membrane. Carbon dioxide formation is observed as soon as helium is switched to 1% carbon monoxide, however hydrogen is not observed for about one and half an hour in step three. In addition, a rapid increase in water evolution is observed simultaneously during the first three hours of introduction of 1% carbon monoxide in helium on the permeate side of the membrane. One reason for this observed delay in hydrogen formation and the rapid increase in water permeation could be that the hydrogen formed in the water–gas shift reaction is oxidised by the oxygen from the residual air (Equation 5.7). There is also a possibility that there is some water vapour contained in the residual air.

Hydrogen oxidation: $H_2 + ½ O_2 \leftrightarrow H_2O$ 5.7

After these three hours steady state values of carbon dioxide and hydrogen are obtained at *ca* 16 nmol/cm^{2}s and 13 nmol/cm^{2}s (t_1), respectively. The stoichiometry of equation 5.1 suggests that for *ca* 9 nmol/cm^{2}s water permeation observed in step two, *ca* 9 nmol/cm^{2}s of hydrogen needs to be produced. Since the only source for hydrogen is water. However it is observed that the outlet gas in step three contains *ca* 13 nmol/cm^{2}s of hydrogen, which is greater than the estimated value. This increase could be attributed to two possibilities. The first possibility is that carbon monoxide being a strong reducing gas increases the rate of water permeation across the membrane as compared with 100% helium flow on the permeate side. Another possibility is systematic errors during experimentation.

The stoichiometric ratio of carbon dioxide to hydrogen in Equation 5.1 is 1. However the average ratio of carbon dioxide to hydrogen is about 1.2 in this study. This could be attributed to carbon monoxide disproportionation (Equation 5.8) which is a common side reaction observed in these types of studies when water to carbon monoxide ratio is less than one [126] or owing to the reaction between carbon monoxide and the membrane.

CO disproportionation (Boudouard Reaction): $2CO \leftrightarrow CO_2 + C$ 5.8

Carbon monoxide can react with lattice oxygen to produce carbon dioxide and oxygen vacancy in this type of perovskite material [127, 128]. The post operation analysis (discussed later in *Section 5.5*) revealed the presence of carbon deposition on this surface on the permeate side and a change in surface morphology. Thus this confirms that carbon monoxide disproportionation reaction occurs during the process.

The reaction mechanism for water permeation coupled with water–gas shift reaction is not clearly known. There are two possible mechanisms that can be speculated. In the first possibility, it is assumed that the water recombination reaction occurs on the membrane surface on the permeate side before reaction with carbon monoxide to form carbon dioxide and hydrogen. Another possibility is that the carbon monoxide reacts with the hydroxyl

groups on the membrane surface, that are formed during water permeation (Equation 5.3), to liberate carbon dioxide and hydrogen.

It is to be noted that the first 3 hrs have similar results for the next set of studies involving platinum coating on membranes and it is expected that the reasons for this observation is same as in the study of bare membrane. Thus the discussion for the first 3 hr analysis has been omitted from the next sections.

b) Pt|BCY20|Pt Membrane

The permeate side outlet gas composition for Pt|BCY|Pt membrane reactor is given in Figure 5.9. The same experimental steps are followed as the previous membrane system as explained in *Section 3.1.4c*. The results of step one and two are similar to that observed in the case of bare membrane. The Pt|BCY20|Pt membrane exhibits a water permeation of *ca* 7 nmol/cm^{2}s which is expected based on the observations of water permeation studies (*Section 5.3*). The membrane displays similar behaviour as bare BCY membrane when carbon monoxide was introduced to the permeate side. Carbon dioxide level increases quickly due to water–gas shift reaction (Equation 5.1), carbon monoxide disproportionation reaction (Equation 5.8) and carbon monoxide oxidation (Equation 5.9) (due to some oxygen purge from dead volume of gas lines). Finally, hydrogen and carbon dioxide rate reach a steady state values of *ca* 9 nmol/cm^{2}s and *ca* 13 nmol/cm^{2}s (at t_2), respectively. As compared with bare membrane there is reduction in the hydrogen and carbon dioxide rate. This could be associated to the low water permeation observed in *Section 5.3* for Pt|BCY20|Pt membrane.

Carbon monoxide oxidation: $CO + \frac{1}{2}O_2 \leftrightarrow CO_2$ 5.9

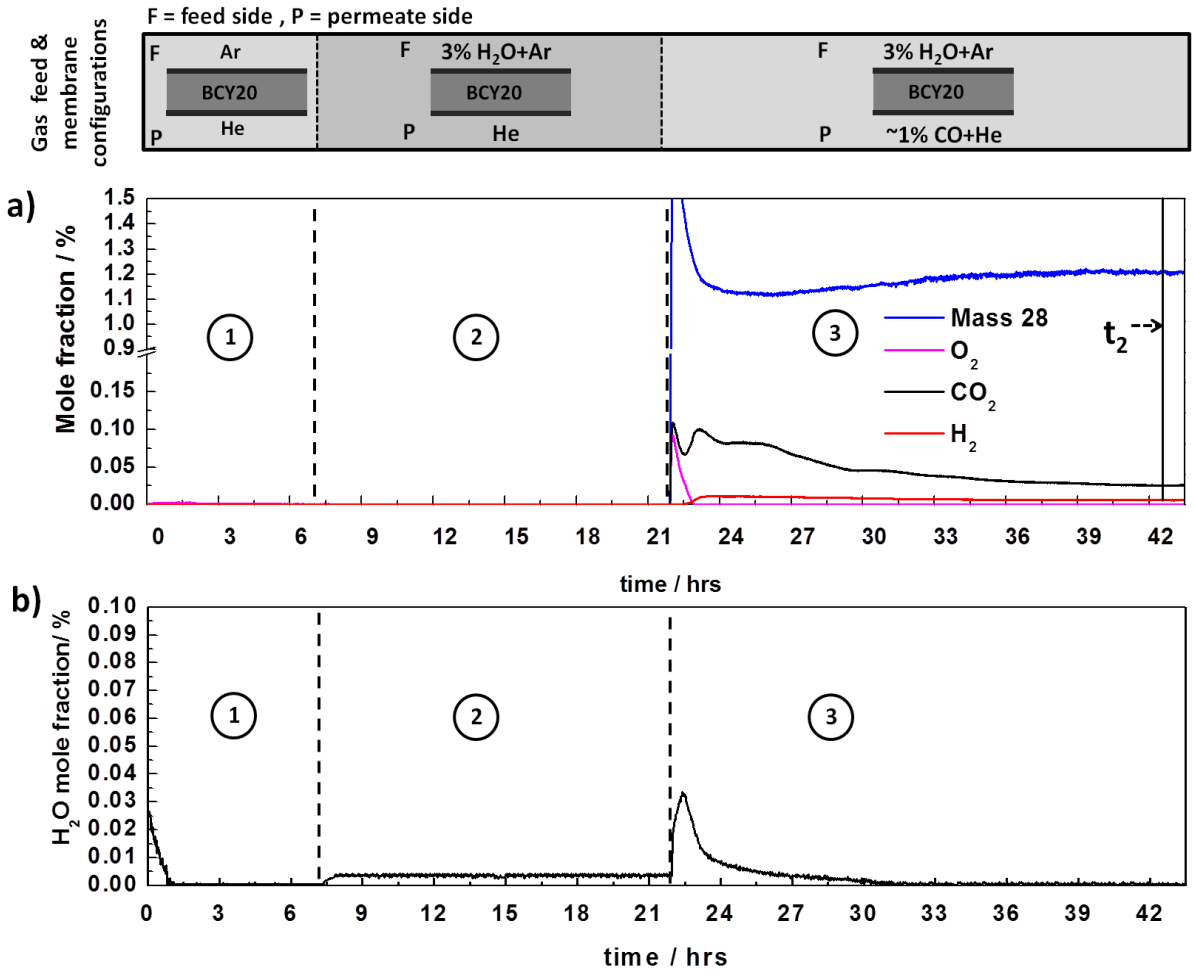

Figure 5.9: Permeate side outlet gas compositions for feed side_Pt|BCY|Pt_permeate side membrane configuration at 700 °C (mass 28, oxygen, hydrogen and carbon dioxide), The flow rates of gases are 100 ml (STP)/min. During **step one:** permeate side inlet: He; feed side inlet: Ar. During **step two:** permeate side inlet: He; feed side inlet: 3% H_2O in Ar. During **step three:** permeate side inlet: 1% CO in He; feed side inlet: 3% H_2O in Ar. **a)** mass spectrometer data **b)** hygrometer data (water)

c) BCY20|Pt Membrane

The result plot for BCY20|Pt membrane displays similar trend as bare membrane seen from Figure 5.10. A final steady state value for water permeation of *ca* 7 nmol/cm^{2}s is observed in step two. The water permeation of Pt|BCY20|Pt membrane and BCY20|Pt membrane are similar, this is similar to the conclusion of *Section 5.3*. This result is expected as compared to the bare membrane (*Section 5.3*). The steady state amount of carbon dioxide and hydrogen were *ca* 14 nmol/cm^{2}s and *ca* 13 nmol/cm^{2}s (at t_3), respectively. It has been observed that a

trend of higher rates of carbon dioxide to hydrogen exists in all catalytic/non–catalytic membrane configurations studied so far.

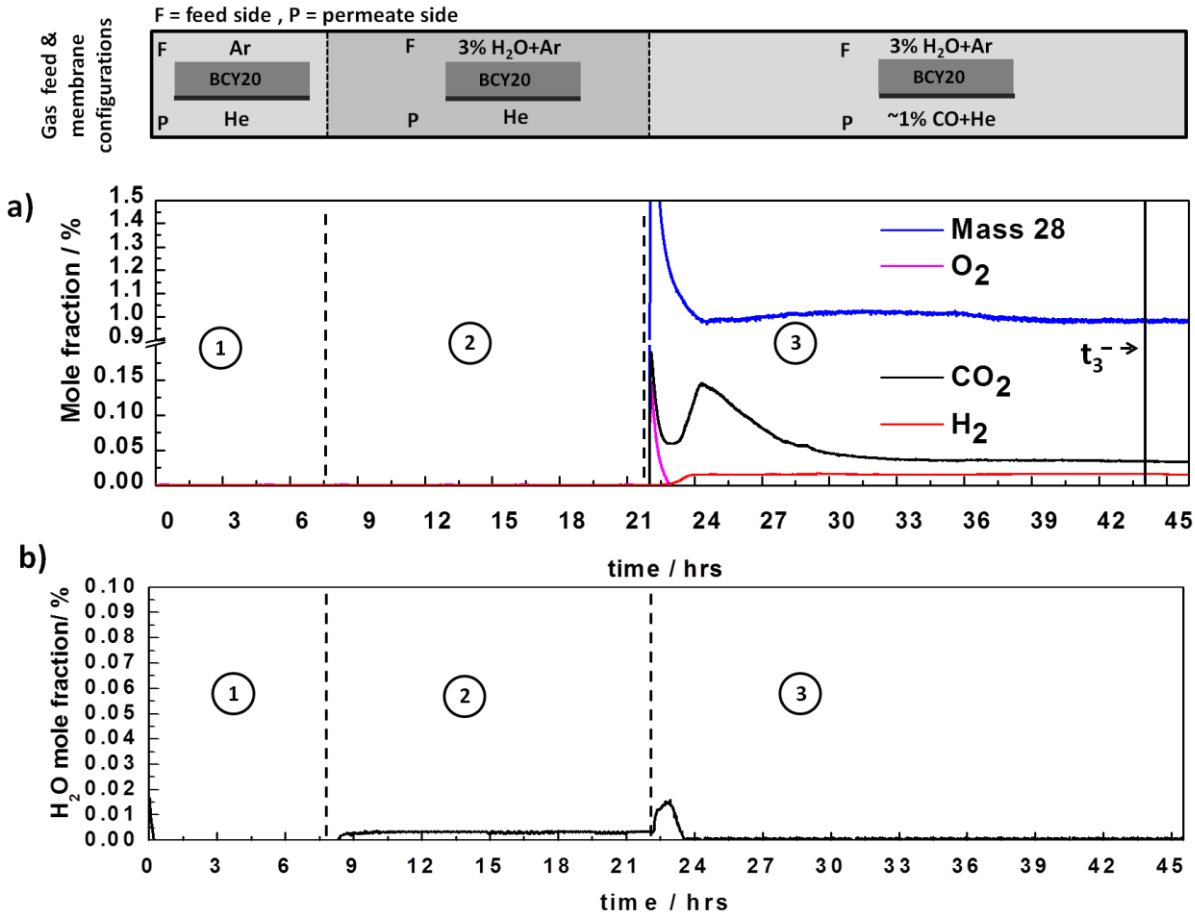

Figure 5.10: Permeate side outlet gas compositions for feed side_BCY|Pt_feed side membrane configuration at 700 °C (mass 28, oxygen, hydrogen and carbon dioxide), The flow rates of gases are 100 ml (STP)/min. During **step one:** permeate side inlet: He; feed side inlet: Ar. During **step two:** permeate side inlet: He; feed side inlet: 3% H_2O in Ar. During **step three:** permeate side inlet: 1% CO in He; feed side inlet: 3% H_2O in Ar. **a)** mass spectrometer data **b)** hygrometer data (water).

d) Pt|BCY20 Membrane

The Pt|BCY20 membrane demonstrated the best performance compared to other membrane configurations in terms of water permeation (*Section 5.3*). The water permeation rate is *ca* 12 nmol/cm^{2}s was obtained in step two. Similarly the steady state rate of carbon dioxide and hydrogen are *ca* 20 nmol/cm^{2}s and *ca* 18 nmol/cm^{2}s (at t_4) as shown in Figure 5.11. The water permeation rate is found to have increased by a factor of *ca* 1.5 when 1% carbon monoxide in helium is used on the permeate side instead of an inert gas alone in Pt|BCY20 membrane calculated from hydrogen rate. This increase in water permeation is higher than other membrane configurations. It can therefore be concluded that Pt|BCY20 membrane is the best candidate for water permeation coupled with water–gas shift reaction.

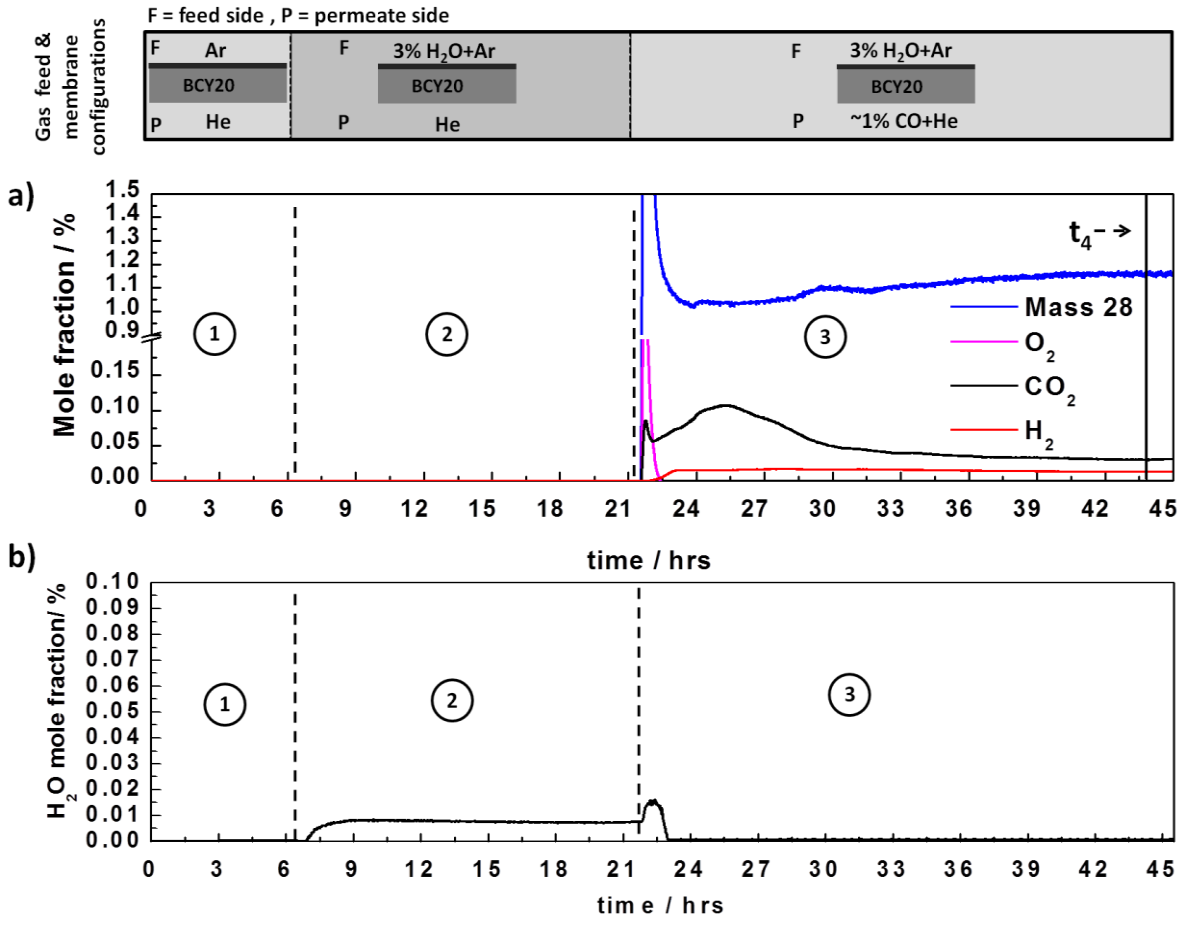

Figure 5.11: Permeate side outlet gas compositions for feed side_Pt|BCY_permeate side membrane configuration at 700 °C (mass 28, oxygen, hydrogen and carbon dioxide), The flow rates of gases are 100 ml (STP)/min. During **step one:** permeate side inlet: He; feed side inlet: Ar. During **step two:** permeate side inlet: He; feed side inlet: 3% H_2O in Ar. During **step three:** permeate side inlet: 1% CO in He; feed side inlet: 3% H_2O in Ar. **a)** mass spectrometer data **b)** hygrometer data (water)

The ratio of carbon dioxide to hydrogen is varied from 1.1 to 1.4 for all membrane configurations. However, the rate of carbon dioxide formation is higher than the rate of hydrogen formation for all membranes. By comparing the membrane performances in terms of the rate of products, it can be suggested that platinum is not a good candidate for water permeation coupled with water–gas shift reaction on the permeate side. However, it has a positive role on the feed side of the membrane and could be used as a catalyst/electrode on the feed side.

5.5 Post Operation Analysis

After simultaneous water permeation and water–gas shift experiments, the membranes are characterised by XRD, SEM and EDXS analyses in order to check any possible change in the structure, phase and chemical compositions of the membranes. The analysis will reveal the chemical stability of the membranes directly under actual operating conditions including the effects of multi–species transport, mass transport, and electrodes. The results from XRD analysis are presented in Figure 5.12 and compared with fresh BCY20 membrane (Figure 5.12a).

Figure 5.12b displays the XRD result of feed side of the BCY20 membrane that is subjected to 3% H_2O in argon for about 45 hrs at 700 °C during water permeation and coupled with water–gas shift experiment. Figure 5.12b indicates decomposition to CeO_2 and $BaCO_3$. This instability in water containing environment is reported previously [129-131]. $BaCeO_3$ reacts with H_2O and CO_2 according to Equations below [132];

$$BaCeO_3 + H_2O \rightarrow Ba(OH)_2 + CeO_2 \quad 5.10$$

$$BaCeO_3 + CO_2 \rightarrow BaCO_3 + CeO_2 \quad 5.11$$

XRD analysis of feed side (where water is introduced) in Figure 5.12b depicts no peaks of $Ba(OH)_2$ due to a reaction between barium cerate and water. This might be due to loss of Ba at high temperature which will result in Ba–deficient phases. Another possible explanation might be the amorphous nature of $Ba(OH)_2$ [133]. Also, the peak at 26° 2θ might be CeO_2 or crystallised silicate in Figure 5.12b.

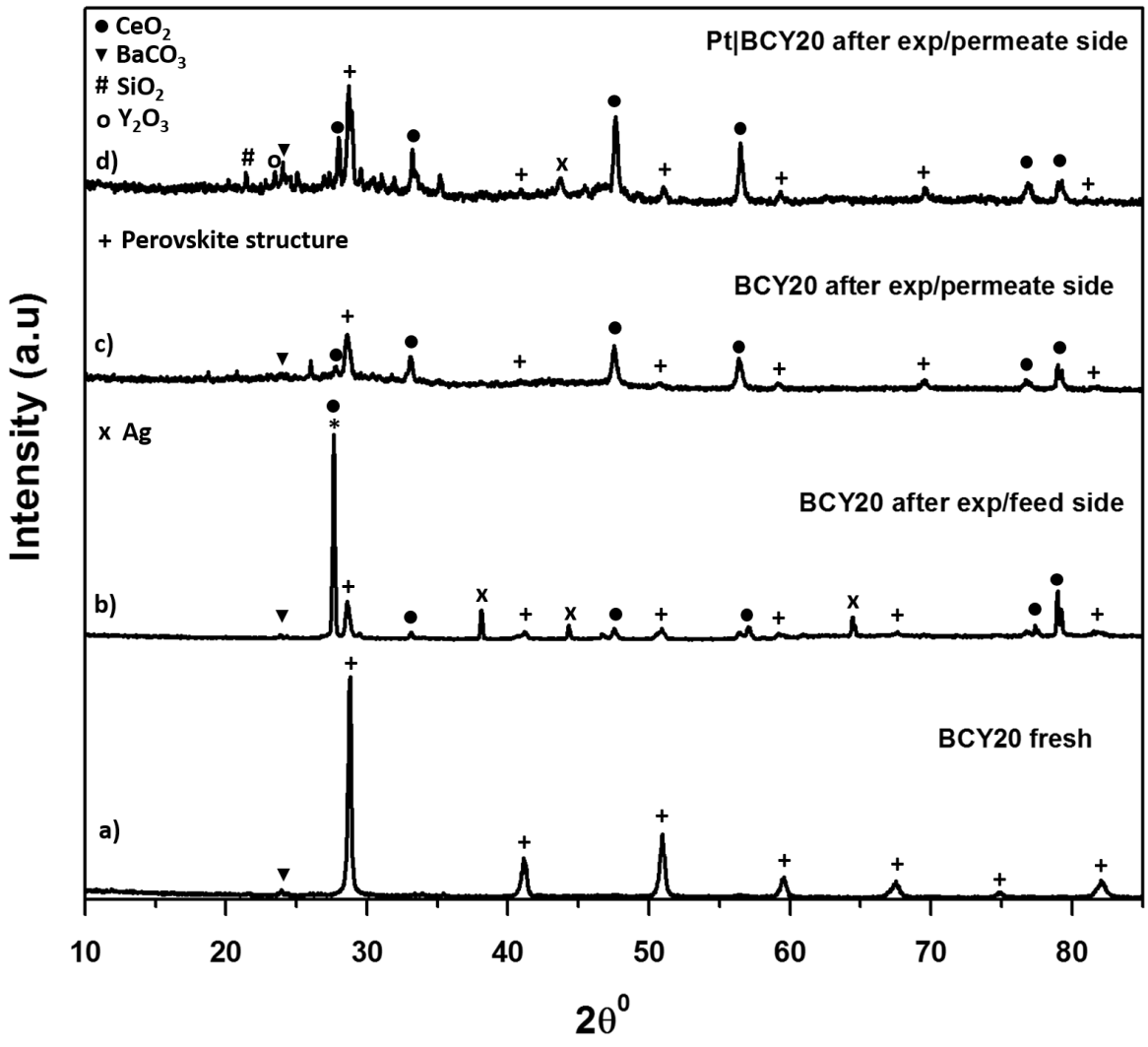

Figure 5.12: XRD patterns of the fresh and used BCY20 membranes. **a)** Fresh BCY20 membrane, **b)** Feed side of the bare BCY20 membrane after the experiment, **c)** Permeate side of the bare BCY20 membrane after the experiment, **d)** Permeate side of the "feed_ Pt|BCY20_permeate" membrane after the experiment. The perovskite structure is indicated by +, the peaks indicative of $BaCO_3$, CeO_2 and Y_2O_3 are indicated by ▼,● and **o**, respectively.

Figure 5.12c and Figure 5.12d demonstrates the permeate side of the membrane that is subjected to 1% carbon monoxide in helium about 30 hrs at 700 °C during the experiments. It is seen that BCY20 lost most of its crystal structure and perovskite phase was no longer recognisable. Both membranes decomposed to $BaCO_3$ and CeO_2. Also, multiple minor phases are observed. The presence of SiO_2 and Ag can be attributed to the sealant material that used in the experiments. By taking into account the partial pressures of water (3%) in argon on the feed side and carbon dioxide (about 0.02%) in helium on the permeate side, and the change in phases (comparing the XRD traces), it can be said that barium cerate reacts easily with carbon dioxide than water. However, in the presence of porous platinum electrode on both sides the instability would be expected to be lower than the bare membrane surface. Due to the fact that platinum covers the membrane surface partially and block the exposure to carbon dioxide and water. The analyses of these surfaces are not presented here since XRD traces only showed the characteristic of platinum peaks. Results indicate that BCY20 is unstable under water, carbon monoxide and carbon dioxide containing environment.

SEM surface images of feed and permeate sides of BCY20 membranes, bare and platinum surfaces, after the experiments are given in Figure 5.13. The Hitachi TM3030 Scanning Electron Microscopy which has a premium secondary electron (SE) detector was used in the analysis. Figure 5.13a and Figure 5.13b depict the feed side surfaces. Distributions of small particles are observed in Figure 5.12a. EDXS measurements indicate an approximate atom surface composition of *ca* 36.3% barium, *ca* 0.6% cerium and *ca* 63.1% oxygen in this surface as given in Table 5.2. Table 5.2 displays the average atomic percentages, the measurements are performed more than ones; see Appendix K for other EDXS results. By taking into account XRD and EDXS analysis, these small particles can be ascribed to cerium oxide. SEM image of platinum surface on the feed side displays a little agglomeration and morphology change underneath, possibly a reaction between water and barium cerate according to Equation 5.10.

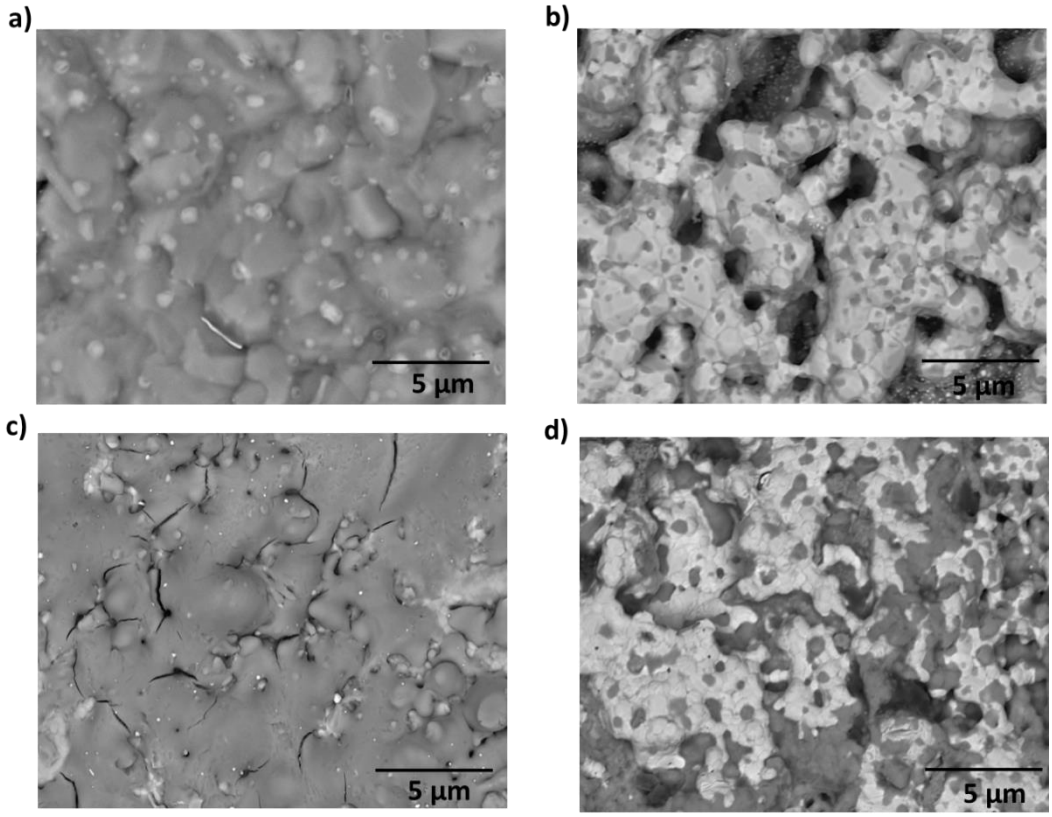

Figure 5.13: Post operation SEM images of the external surfaces of feed sides (a&b) and permeate sides (c &d). Feed side: **a)** bare surface **b)** platinum surface, Permeate side: **c)** bare surface **d)** platinum surface.

Figure 5.13c and Figure 5.13d show the permeate side surface images. Both surfaces indicate a morphology change and distribution of black spots over the whole surfaces. Figure 5.13d depicts agglomeration of platinum particles over the whole surface. EDXS analysis (Table 5.2) suggests carbon content on these surfaces and implies higher carbon content in the presence of platinum on that surface. This displays that carbon accumulation increases in the presence of platinum on the permeate side which could be owing to carbon monoxide disproportionation under this condition. Another reason might be carbon monoxide binding of platinum active sites since carbon monoxide can bind platinum strongly even at low ppm levels [134, 135]. In the case of Figure 5.13c, the surface morphology change could also be due to solid–gas reaction on the BCY20 surface since carbon monoxide could adsorb and react with the lattice oxygen [136]. The presence of silicon in Table 5.2 can be attributed to the sealant used in this study.

Table 5-2: Post operation EDXS average surface compositions of feed sides and permeate sides.

Location	Approximate atom (%)						
	Ba	**Ce**	**Y**	**O**	**Pt**	**Si**	**C**
Feed side, bare surface	36.3±2.96	0.6±0.40	-	63.1±2.61	-	-	-
Feed side, platinum surface	-	-	-	-	100±0.01	-	-
Permeate side, bare surface	24.8±0.49	0.6±0.35	0.1±0.18	70.3±1.08	-	-	4.2±1.33
Permeate side, platinum surface	3.4±0.46	-	-	-	22.6±0.29	2±0.35	72±1.10

5.6 Summary and Conclusions

In this chapter, BCY20 perovskite material catalytically modified/unmodified are used as membranes so as to perform water permeation and simultaneous water permeation and water gas shift experiments. The first set of experiments showed that platinum can increase water permeation when it is applied on the feed side surface of the membrane, suggesting that platinum is catalytic for water dissociation/ incorporation. A decrease is observed in water flux when platinum is coated on the permeate side of the membrane compared with bare membrane. This implies that platinum has a negative role in water recombination. Platinum coating on the permeate side seems to create a blocking mechanism for water recombination. This could be due to the fact that platinum reduces the active sites for recombination on the permeate side or low ionic conductivity of platinum layer.

The second set of experiments (water permeation coupled with water–gas shift reaction experiments) is conducted for four different membrane configurations in three steps for over 45 hrs. By comparing the rate of hydrogen production in step three and water flux in step two, it is found that the water permeation rate depicted an increase in the presence of reducing gas on the permeate side in step three. Moreover, the water permeation rate and post operation analysis suggest that the presence of platinum on the permeate side is detrimental for both water permeation and water–gas shift reaction.

Platinum coating on the permeate side surface of the membrane decreased water permeation via a site–blocking mechanism and also increased carbon deposition via carbon monoxide disproportionation reaction. In addition, post operation SEM images of permeate side platinum shows agglomeration which in turn reduces the available porous surface area for water recombination. On the other hand, unmodified permeate side surface of the membrane analysis exhibits decomposition into cerium oxide and barium cerate. Neither platinum nor bare BCY20 membrane is favourable for water permeation and water–gas shift reaction on the permeate side of the membrane. In the case of practical membrane applications, a better electrode which has less catalytic activity towards carbon monoxide disproportionation and high catalytic activity for hydrogen/oxygen evolution should be preferred.

The equilibrium carbon monoxide conversion of water–gas shift reaction at 700 °C with a 1:1 ratio of water to carbon monoxide is reported as 55% by Haryanto *et al* [137]. That ratio is very low (about 0.01) under these experimental conditions which resulted in undesirable side reactions (e.g. carbon monoxide disproportionation). In order to achieve full carbon monoxide conversion higher water flux is needed. By assuming that membrane thickness is a rate limiting step of bulk diffusion and the relationship between water flux and membrane thickness is linear, a 35–fold decrease in membrane thickness (~34 μm) is required to provide sufficient water flux for full carbon monoxide conversion in the case of using Pt|BCY20 membrane reactor which gives a better performance in terms of water permeation and stability than other membrane configurations under the current experimental conditions. In addition, platinum should not be preferred as an electrode on the permeate side of the membrane in the case of using a water permeable electrolyte. While the water permeation seems to very low for practical operation of a solid oxide fuel cell, this study enables evaluating the concept and guides towards improving of membrane performance.

Chapter 6
Investigation of Simultaneous Water and Oxygen Transport through BCY20 Membrane for IT-SOFCs

6.1 Introduction

In conventional hydrocarbon–fuelled fuel cells, water is injected to the anode side which results in several problems in terms of the cell degradation and efficiency as discussed in *Section 2.4.3.* Water permeable electrolytes could offer introduction of water to the cathode side along with air as oxidant and could eliminate most of these problems. Water permeation from the cathode side of cell to the anode side could facilitate hydrocarbon reforming so that IT–SOFCs can directly use hydrocarbon fuels without any previous reforming treatment. Moreover, as the process continues water will be generated as a result of fuel cell reactions, hence with sufficient time, the introduction of water to the cathode side may even be decreased or interrupted. For a water permeable electrolyte to be viable for hydrocarbon reforming in IT–SOFCs it is important to understand the coupled transport mechanism for water and oxygen from cathode side to anode side.

The main charge carriers for both water and oxygen transport in perovskite type of materials are protons ($H^{\bullet}$) and oxygen vacancies ($Vo^{\bullet\bullet}$) [138]. The transport of water starts with water splitting reaction at the interface between the electrode and electrolyte or on the electrolyte surface ($H_2O_{(g)} + V_o^{\bullet\bullet} + O_o^x \leftrightarrow 2OH_o^{\bullet}$). Then, the transport of water within the electrolyte takes place as follows:

$$OH_O^{\bullet} + O_O^x \leftrightarrow O_O^x + OH_O^{\bullet} \quad 6.1$$

The oxygen incorporation into the electrolyte and desorption from the electrolyte at the electrode–electrolyte interface , are shown by the reversible reaction [139]:

$$1/2\, O_{2(g)} + 2e' + V_O^{\bullet\bullet} \leftrightarrow O_O^x \quad 6.2$$

where e' is the electron from the electrode, $V_O^{\bullet\bullet}$ is the oxygen vacancy and O_O^x is the lattice oxygen. The transport of oxygen within the electrolyte is expressed by Equation 6.3 [118, 140]:

$$O_O^x \xleftrightarrow{V_o^{\bullet\bullet}} O_O^x \quad 6.3$$

Equation 6.2 involves a number of steps including adsorption, disassociation, ionisation and incorporation of oxide ions into the oxygen vacancies of lattice at the electrochemically active region. The electrochemically active regions are the three phase boundaries in fuel cells where electrode, electrolyte and gas phase are in contact [141, 142] and necessary when electrode possesses electronic and electrolyte possesses ionic conductivity. Also, Equation 6.3 displays bulk diffusion. The BCY20 electrolyte is capable of transporting both oxygen and water at the same time under fuel cell operating conditions as shown in Figure 6.1. However, Equations 6.1 to 6.3 indicate that both water and oxygen incorporation into the electrolyte and diffusion within the electrolyte requires oxygen vacancies and oxygen sites within the electrolyte, assuming that both oxygen and water chemical potential gradients are in the same direction.

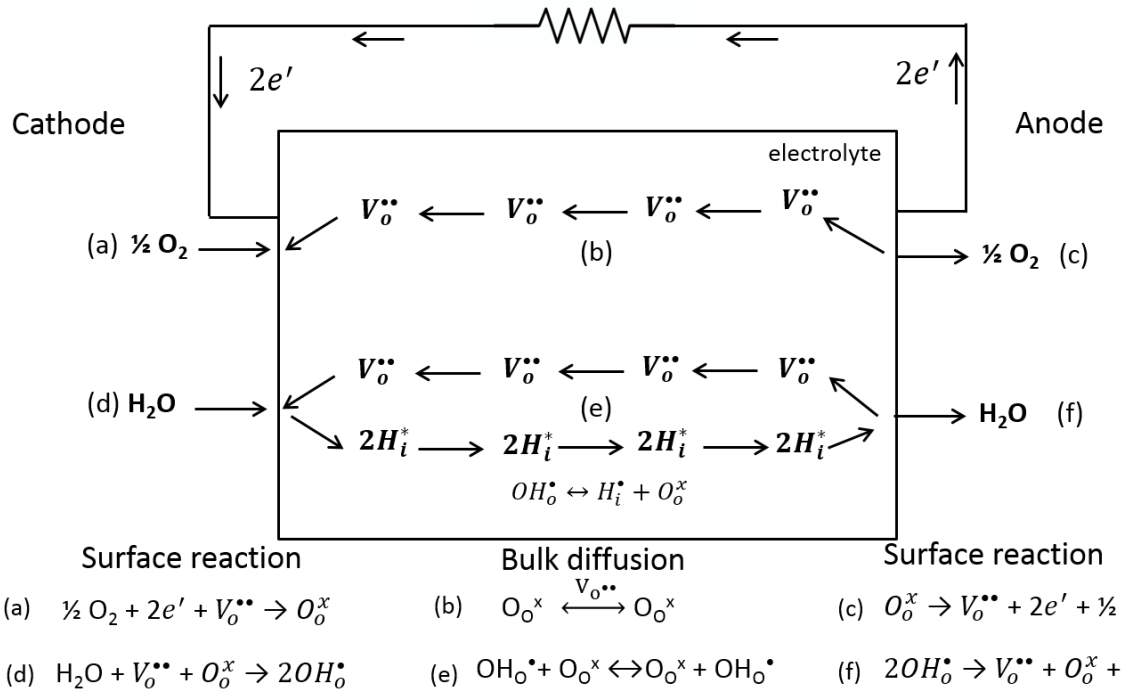

Figure 6.1: Schematic representation of co-transport of oxygen and water from cathode side to anode side. The transport of oxygen involves reduction of oxygen at the cathode (Equation a), then incorporation into electrolyte and bulk diffusion via oxygen vacancies ($V_O^{\bullet\bullet}$) within the electrolyte (Equation b). The reverse reaction (Equation c) takes place at the anode. Electron transfer occurs via the external circuit. The transport of water from cathode to anode takes place via the reaction of water with oxygen vacancy and lattice oxygen at the surface (Equation d). Then diffusion within the electrolyte occurs as interstitial defects ($H_i^{\bullet}$) that jumps between OH groups (Equation e) and finally water desorption happens (Equation f) at the anode. The electronic charge carrier does not involve in water transport. All the reactions are shown in Kröger –Vink notation.

In the case of simultaneous incorporation and diffusion, both processes may compete with each other or may have separate pathways. A separate route for oxygen and water would be beneficial in terms of increasing the efficiency of the cell and would be favourable for hydrocarbon reforming. Moreover, the presence of one species may help to drive the flux of the other species since the actual transport of oxygen and water occurs by the separate migration of protonic defects and oxide ions within the electrolyte.

However, a competition between the two external reactions and bulk diffusion could affect permeation of one or both species partially or significantly as seen in Figure 6.1. When

oxygen and water share active sites then, water may occupy oxygen adsorption sites at the cathode surface. This would deteriorate the oxygen reduction reaction and incorporation into the electrolyte or/and water may consume oxygen vacancies within the electrolyte. Resulting in reduction of their concentration and hence reducing the oxide ion conductivity of the electrolyte. One can equally consider oxygen to be occupying water sites at the cathode surface or within the electrolyte and hence reducing the water permeation flux.

Another possibility is that they could both deteriorate each other's transport partially instead of one stops the other`s incorporation and diffusion completely. In order to utilise these electrolytes in fuel cells the complex electrochemistry must be known. There has been no attention to this mechanism in the oxidant side in terms of fuel cell application in the literature. Therefore, a better understanding of the behaviour of this system can lead to a better evaluation of the feasibility of water permeable electrolytes to be used for hydrocarbon reforming. For instance, if water affects oxygen conduction significantly, this may undermine the overall fuel cell efficiency. Since oxygen produces current and helps fuel combustion at the anode. However, water transport would decrease temperature gradient and help reducing carbon deposition.

Previous chapter has focused on the water permeation behaviour of the membrane and the feasibility of water gas shift reaction via utilising the permeated water. In addition to that, the first part of this study will evaluate the water, oxygen and simultaneous oxygen and water transport by using current–overpotential characteristics and evolution of water and oxygen at the anode. This will reveal the additive or hindering effect of water on oxygen incorporation and transport, providing a direct and critical assessment of simultaneous water and oxygen transport for IT–SOFCs. Finally, the second part of this study will look at the fuel cell performance using various fuels for internal reforming and evaluate the ability of the membrane for simultaneous multi–tasks.

6.2 Water Permeation under Polarisation

The results for water concentration without and with polarisation are presented in Figure 6.2. The cathode side of the cell (previously referred as feed side, Chapter 5) represents where 3% water in argon is fed and the anode side of the cell (previously referred as permeate side, Chapter 5) represents where helium is fed. This terminology has been used throughout the chapter to avoid confusion and ease the discussion. The working electrode is placed at the cathode side. The anode outlet stream is analysed by using a hygrometer and a mass spectrometer. Stable water concentration at the anode outlet is observed for 3600 s before application of polarisation at a fixed temperature of 700 °C. Then the potential is applied from 0 V to -1 V at 3600 s. The insert in Figure 6.2a shows the water concentration before and during the polarisation, where ‘a’ corresponds to 0 V and ‘k’ corresponds to -1 V applied potential. The difference between each step is 100 mV with an acquisition time of 200 s to monitor any change in water concentration with the applied potential. Figure 6.2a shows the measured water concentration versus the applied potential between 0 V and -1 V, the steady values are taken as the water concentration at each applied potential. Figure 6.2b presents an I–V curve obtained during water concentration using the cell configuration in Figure 3.5a. The anode side outlet stream monitored using the mass spectrometer, is also given in Figure 6.2c.

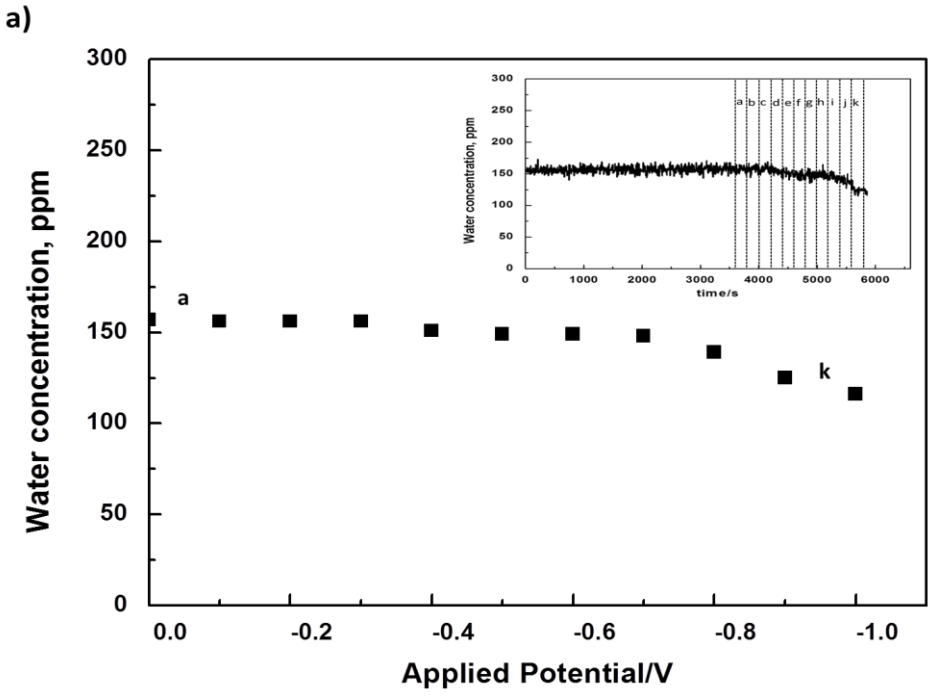

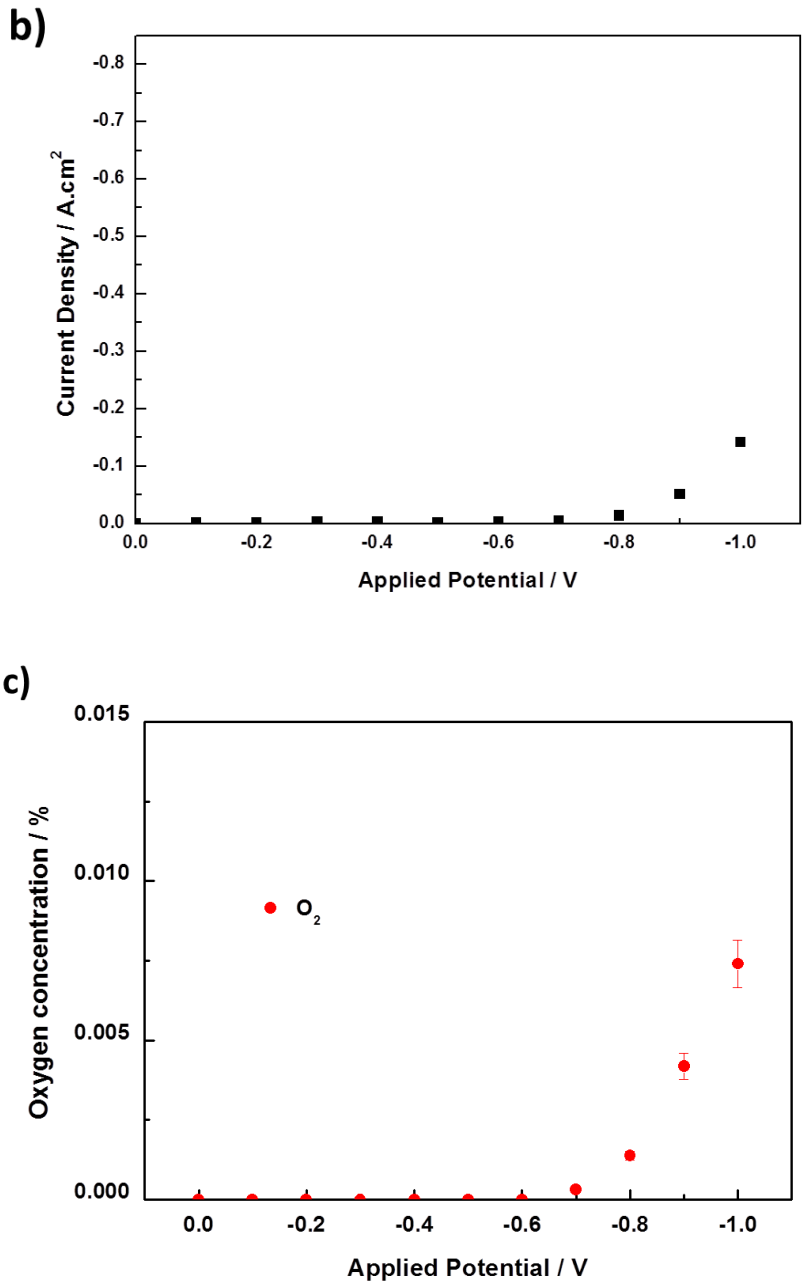

Figure 6.2: a) The water concentration is presented versus the applied potential. The potential is applied between working (cathode) and reference electrode (anode side). The insert graph shows the raw data that is obtained using the hygrometer at the anode outlet which exhibits the change in water concentration at the anode side versus time. Argon is used as a carrier gas at the cathode side. (water concentration is observed for 3600 s under non–polarised conditions, then the potential is applied between 0 V and -1 V with -100 mV steps and the acquisition time is 200 s per set voltage, `a` corresponds to 0 mV and `k` corresponds to -1 V, between a and k corresponds -100 mV step) **b)** The current is presented versus the applied potential **c)** The oxygen concentration is observed at the anode outlet using the mass spectrometer. All measurements are done at 700 °C.

There is no significant difference (the change in water concentration is less than 10 ppm) observed in water concentration at 700 °C under the applied potential of up to -0.8 V (until letter i in Figure 6.2a). This suggests water permeation is not affected by the application of potential; also polarisation does not seem to have influence on the water permeation rate under these experimental conditions up to a certain potential. A representation of the transport phenomenon under polarisation is shown in Figure 6.3. Water reacts with the available lattice oxygen and oxygen vacancy at the cathode side regardless of the applied potential. Following the transport of protons and oxygen vacancies within the electrolyte, the dehydration occurs on the other surface. The water transport does not involve any electron transfer (only a chemical reaction) hence the current is expected to be zero. However, a small current around 1 mA is observed as can be seen in Figure 6.2b. This current may be due to the hole current which could be expressed as follows:

$$2h^{\bullet} + 2e' \rightarrow 0 \quad (Cathode) \tag{6.4}$$

$$0 \rightarrow 2h^{\bullet} + 2e' \quad (Anode) \tag{6.5}$$

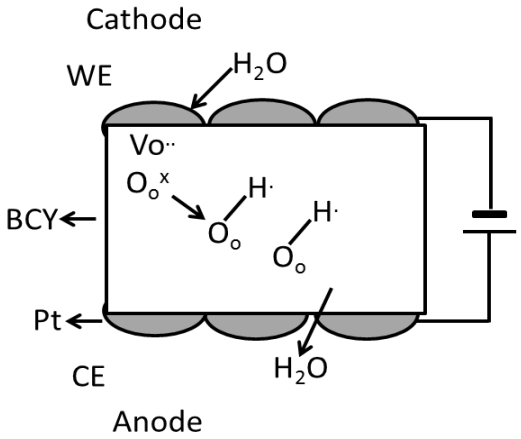

Figure 6.3: Schematic illustration of water transport within the electrolyte under polarisation. The transport of water occurs via oxygen vacancies within the electrolyte regardless of applied potential in water containing environment.

As suggested by Grover [81], the hole current may be neglected at low and moderate oxygen pressures demonstrating that water transport process is independent of an externally applied potential and occurs due to chemical diffusion.

Subsequently, the water concentration starts to decrease at the anode side for the applied potential values below -0.8 V. Simultaneously oxygen evolution at the anode side outlet stream is observed represented in Figure 6.2c. This may be attributed to decomposition of water on this side due to the following reasons. The voltage of water decomposition for standard conditions at 700 °C is calculated as ~ 0.99 V. However, the potential is applied versus reference electrode, not counter electrode (anode).Thus, -0.8 V is not the cell potential between cathode (working electrode) and anode (counter electrode). Thus, the exact cell potential is unknown. The reference electrode`s potential is assumed to be more or less stable (versus hydrogen electrode) and taken as a pseudo reference.

On the other hand, water may decompose at lower potential than the theoretical value. This may be owing to the fundamental difference between liquid water and gaseous water electrolysis. The voltage of electrolytic water splitting at room temperature and 1 bar ambient pressure is 1.23V (U°) [143]. However, when the water vapour is used, the partial pressure of all gases is changeable. In this case, the decomposition voltage of water is given as follows [143];

$$U = U^{\circ} - \frac{RT}{2F} ln \frac{P_{H_2O}}{\sqrt{P_{O_2}}.P_{H_2}} \qquad 6.6$$

Where U is the decomposition voltage of water, U° is the decomposition voltage of water at standard conditions; R, T and F represent the universal gas constant, the temperature in Kelvin and the Faraday constant, respectively. P_{H_2O} is the partial pressure of water at the cathode (working electrode) side, P_{O_2} is partial pressure of oxygen at the anode (counter electrode) side, and P_{H_2} is partial pressure of hydrogen at the cathode.

Even for known P_{H_2O} at the cathode, it is not possible to estimate the decomposition voltage of water under these conditions since the cathode outlet stream is not analysed and partial pressure of hydrogen is unknown. Also, P_{H_2} and P_{O_2} vary with the gas flow and the current. This phenomenon of water splitting below standard decomposition voltage was observed and reported in the literature by Walch *et al* [143].

As can be seen from Figure 6.2b and 6.2c, following the decomposition of water, oxygen evolution is observed. Subsequently, the current density increases from ~ 0 A/cm^2 to ~ - 0.14 A/cm^2. This increase could correspond to proton and oxide ion current (electrolysis current) due to water splitting. However, the cathode side outlet stream is not analysed. That is out of the scope this work since the interest is investigation of water on oxygen transport. The water decomposition can take place based on the following electrode reactions [144]:

$$Anode: H_2O_{(g)} \rightarrow 2H^{\bullet} + 2e' + \tfrac{1}{2}O_2 \qquad 6.7$$
$$O^{2-} \rightarrow \tfrac{1}{2}O_2 + 2e'$$

$$Cathode: 2H^{\bullet} + 2e' \rightarrow H_2 \qquad 6.8$$
$$H_2O_{(g)} + 2e' \rightarrow H_2 + O^{2-}$$

It is also observed that decrease in water concentration at the anode side is not equal to increase in oxygen concentration at the anode outlet, suggesting that oxygen is pumped from cathode to anode electrochemically. Pumping hydrogen from anode to cathode is another possibility due to mixed conductivity which in turn could affect water permeation rate. This could be investigated further. However, since cathode side water concentration is much higher than anode side water concentration, pumping oxygen would be much favourable.

In conclusion, water permeation is not affected by externally applied potential and it remains as a chemical reaction rather than an electrochemical reaction. The driving force for this reaction is the partial pressure difference of water between two surfaces.

6.3 Water Permeation under Polarisation and Air as a Carrier

6.3.1 Water and Oxygen Permeation under Polarisation

Two cases are discussed in this section; when only air is present at the cathode and 3% H_2O in air is present at the cathode. The anode feed gas is helium in both cases. The anode outlet stream is monitored by using a hygrometer and a mass spectrometer. When only air is present at the cathode, oxygen evolution at the anode outlet is measured. On the other hand, oxygen and water evolution at the anode outlet are measured when 3% H_2O in air is present at the cathode. Figure 6.4a corresponds to hygrometer data with 3%H_2O in air is fed to the cathode side of the cell and the helium is fed to the anode side of the cell. Stable water concentration is observed until the application of potential for 3600 s. The potential is then applied between 'a' and 'k' starting from 0 V to -1 V with -100 mV steps and the acquisition time is 200 s per set voltage to observe any change in water concentration. Water concentration increases at the anode side with the application of potential up to -0.8 V shown in Figure 6.4a. Then a decreasing water concentration trend is seen similar to Figure 6.2a. The analysis will be carried out in the rest of the study for the applied potential of up to -0.8 V since the mechanistic interpretation lower than this potential lies beyond the scope of this work.

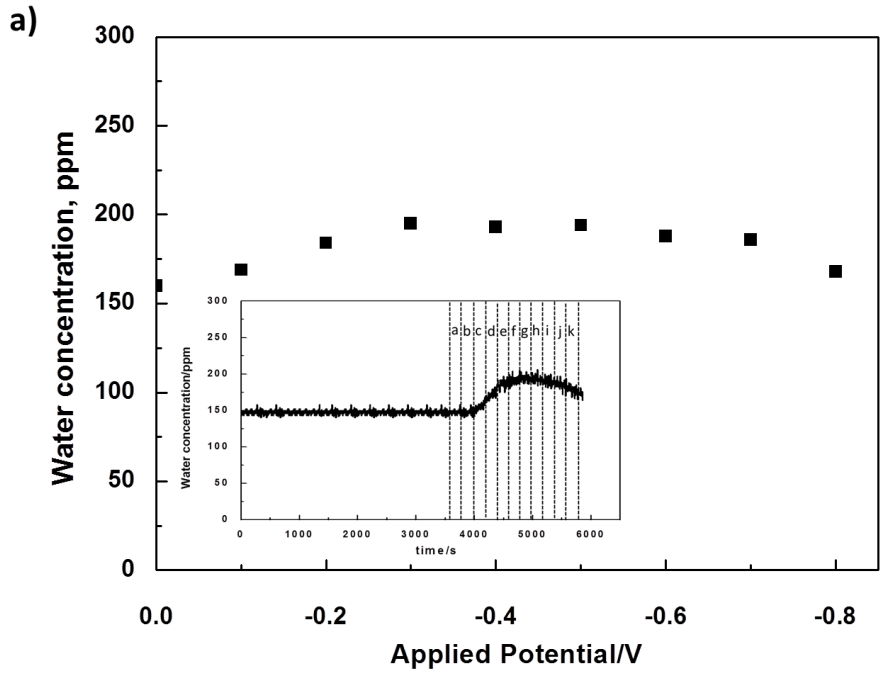

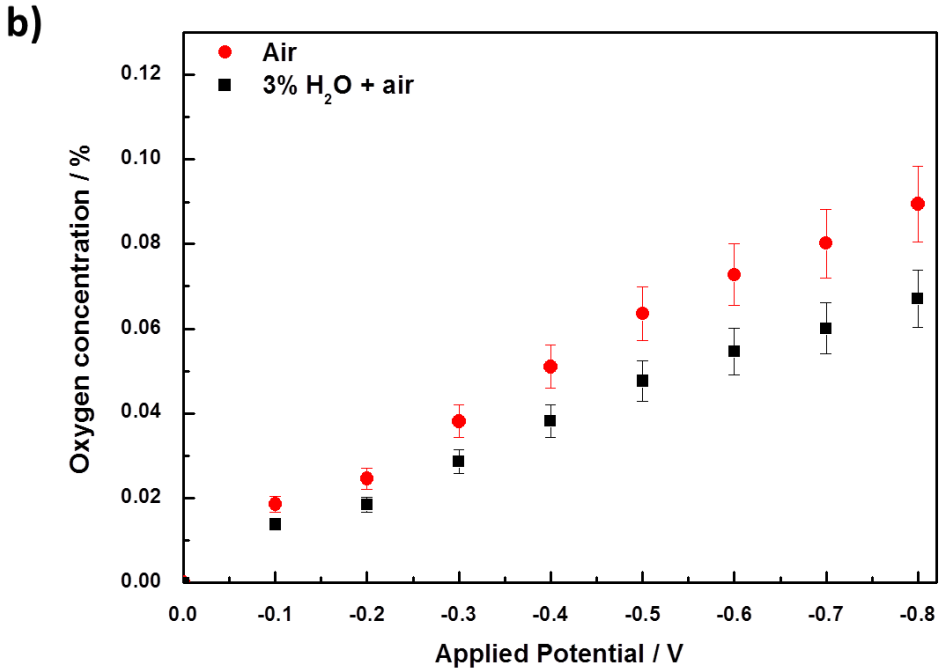

Figure 6.4: a) The water concentration is presented versus the applied potential at the anode outlet after polarisation is applied at 3600 s. Water concentration change versus time is also shown. Air is used as carrier gas at the cathode side. (water concentration is observed for 3600 s under non-polarised conditions, and then the polarisation is applied between 0 V and -1 V with 100 mV steps and the acquisition time is 200 s per set voltage, 'a' corresponds to 0 mV, 'k' corresponds to -1 V with -100 mV step between them) **b)** Oxygen evolution is monitored at the anode outlet by the mass spectrometer in the presence of only air and 3% H_2O in air is present at the cathode and the anode gas is helium.

Under non–polarised conditions water interacts with oxygen vacancies and the lattice oxygen at the cathode side of the cell and forms two protonic defects at this surface. The protons then jump from one oxygen site to another until they reach the other surface where dehydration occurs, protons react with available surface oxygen atoms and leave the lattice. In the presence of high oxygen partial pressure at the cathode side, oxygen may compete for oxygen vacancies at this surface according to reaction shown in Equation 6.2. The water concentration does not show any significant change when air is used as a carrier gas instead of argon as shown in Figure 6.4a under the current experimental condition. This means that under the non–polarised experimental conditions where oxygen partial pressure is ~ 0.2 atm similar to air that is used in fuel cells, the presence of oxygen has no parasitic effect on water

permeation due to a competition for oxygen vacancies. It has been reported that this may be the case in extreme conditions where the oxygen partial pressure is above 0.5 atm [85]. This may be due to incorporation of water is more facile than incorporation of oxygen.

On the other hand, the water concentration alters with the application of the potential as shown in Figure 6.4a. The electrochemical pumping of oxygen (polarisation) (Cathode: $½O_2+2e'\rightarrow O^{2-}$ Anode: $O^{2-}\rightarrow ½O_2+2e'$) from the cathode side to the anode side increased the water concentration slightly at the anode side as shown in Figure 6.4a. Under polarised conditions where an electric field is established due to the potential difference between the electrodes, the charged defects are free to migrate through the electrolyte and reach the other electrode surface to oxidise. Oxygen pumping turns out to be an additional driving force for water transport. However, the transport of water still relies on the ambipolar diffusion of protonic defects and oxygen ion vacancies and independent of externally applied potential. An explanation for the increase in water concentration might be; the removal of protons by reacting available surface oxygen atoms at the anode side of the electrolyte surface. Pumping oxygen to anode surface may increase the possibility of proton and oxygen recombination at that high temperature at this surface.

Additionally, it is possible that the surface oxygen atoms may prefer to recombine with protons (hydrogen) and form water again at the anode surface rather than leaving the electrolyte as oxygen. This implies that protons can recombine with any available surface oxygen and exchange partner oxygen atoms. The results also suggest that the presence of oxygen in the feed stream may affect the diffusion of oxygen vacancy through the electrolyte as compared with absence of oxygen in the feed stream. Similarly, Sakai *et al* [145] studied the impact of water on oxygen transport for fluorite–type oxide ion conductor (YSZ) and reported slightly lower oxygen diffusion coefficient for wet atmosphere than dry atmosphere. Although, they have studied the effect of water on oxygen transport, the reverse effect is also possible.

There is no significant decrease observed in oxygen evolution due to the presence of water in air. Figure 6.4b suggests that oxygen evolution decreases slightly when water is introduced to air at the cathode. This is possible due to a decrease in current and partial pressure of oxygen

(discussed later in *Section 6.3.2*). The concentration of oxygen in air is 20.5%, however, the concentration of oxygen decreases to ~19.8% when 3% water is added to air.

The impact of humid atmosphere on oxygen transport was also studied for LAMOX family oxide ion conductor $La_2Mo_2O_9$ by Liu *et al* [95, 146, 147]. Their result exhibited a decrease in oxygen diffusion coefficient. They explained this decrease by formation of hydroxyl groups at the surface and capturing available oxygen vacancies, however, they did not point out whether hydroxyl groups diffuse into the bulk or not. Therefore, it is also possible that adsorbed water plays a role in the dissociation, reduction and incorporation of oxygen at the surface in this study. This could be similarly because of reduction in the active sites at the electrolyte surface for oxygen reduction reaction near the three phase boundary region or reduction available oxygen vacancies at the surface for oxygen incorporation into the electrolyte. Further analysis will be carried out in the next section by comparing currents that are obtained with and without water in air at the cathode side.

6.3.2 Current –Voltage Curve

Figure 6.5 shows the current density overpotential characteristics when air (cell configuration b in Figure 3.5) and 3%H_2O in air (cell configuration c in Figure 3.5) are fed to the cathode side and dry helium is fed to the anode side. The overpotential of the electrode is calculated by subtracting the ohmic resistance of electrolyte from the applied potential between working and reference electrode as described in *Section 3.1.4d.* The current density increases as applied potential increases. However, Figure 6.5 demonstrates a slight decrease in current density (maximum 50 mA/cm^2) when water is introduced to air at the cathode. This is speculated due to a decrease in oxygen partial pressure at the cathode side.

The data obtained in this study are consistent with the previously reported data by Guan *et al* [148] who studied the transport properties of 5% yttrium–doped $BaCeO_3$ with impedance spectroscopy. Their total conductivity results in different atmospheres show that the total conductivity decreased when 2% water is introduced to oxygen atmosphere. Additionally, increasing electronic conductivity (hole conductivity) with increasing temperature (from 500 °C to 800 °C) and oxygen partial pressure has been reported for these types of materials in the

literature [10, 148-152]. This phenomenon is not studied in detail as it is beyond the scope of the current research.

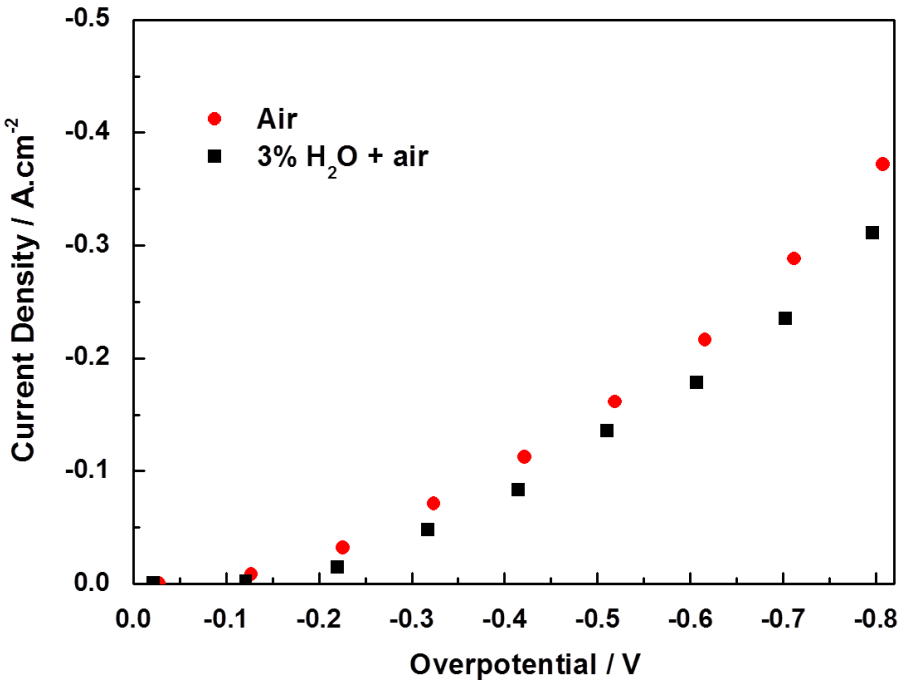

Figure 6.5: The current is presented versus overpotential. Measurements are done for two cases; only air is present at the cathode and 3% H_2O in air is present at the cathode. Helium is fed to anode.

In this study there is no significant impact observed in current and oxygen evolution due to the presence of water in air. It has been demonstrated that BCY20 membrane allows both water and oxygen transport under fuel cell operation conditions (i.e. under oxidising environment and high temperature). In order to evaluate the effect of simultaneous oxygen and water transport on the fuel cell performances, further investigation is performed by using various fuels at the anode in the next section.

6.4 Fuel Cell Operations using Various Fuels with Simultaneous Water Permeation

The operation of a SOFC with various fuels to evaluate its feasibility of hydrocarbon reforming with the aid of water permeation from cathode side to anode side is carried out. The performance of the fuel cell modules are evaluated by measuring the OCP and the current associated with the application of potentials from OCP to 0 V with 1 mV/s step change. The theoretical OCP at 700 °C with hydrogen as fuel and air as oxidant is calculated as ~999 mV, based on the water formation reaction. This value is affected by the nature and composition of fuel, gas leakage from the sealants and the kinetics of the electrode reactions. Figure 6.6 depicts the relationship between the overpotentials and the current density as well as I–V curves when the fuel cell is tested using 5% H_2 in helium at the anode as fuel and air and 3% H_2O in air at the cathode as oxidant.

The experimentally measured OCP value for hydrogen as fuel and air as oxidant is 948 mV which is slightly lower, but still close to the theoretical value (~999 mV). The slight difference may be due to gas leakage from the sealants. In the case of using 3% H_2O in air at the cathode the OCP of the cell decreased to 915 mV. Such phenomenon is observed when 5% CO in helium or 5% CH_4 in argon is used as fuel at the anode, too. This decrease may be due to the change in oxygen partial pressure at the cathode side (*Section 6.3.2*). When, water is added to anode, the partial pressure of oxygen drops.

The non–linear I–V curve indicates the existence of polarisation at the electrode/electrolyte interface [153, 154]. Moreover, the platinum electrode polarisations are greater than the electrolyte resistance, indicating that the performance of the cell is significantly affected by the electrode polarisations. There is no activation losses observed in the IV curves possible due to operating at high temperatures. The anode overpotential increases in both cases as the current density increasing, demonstrating mass transport resistance in that region.

Akoshima *et al* [155] reported slow surface diffusion of adsorbed hydrogen near three phase boundary as the rate determining step at Pt/$BaCe_{0.95}Y_{0.05}O_{3-\delta}$ interface. However, they

observed that the overpotential of cathode decreased with the introduction of water to the cathode side. This indicated that water can catalyse the cathode reaction kinetics and is favourable for the cathode reactions. Similar result was obtained by Sakai *et al* [156] who studied the effect of water on Pt|YSZ interface and reported an improvement on cathode overpotential by addition of water to air, suggesting that reactions around three phase boundary are rate determining. Therefore a similar effect of water facilitating cathode reactions and thus decreasing the electrode resistance is observed in this study. The curvature in the I–V curve can be attributed to adsorption or mass transport limitations.

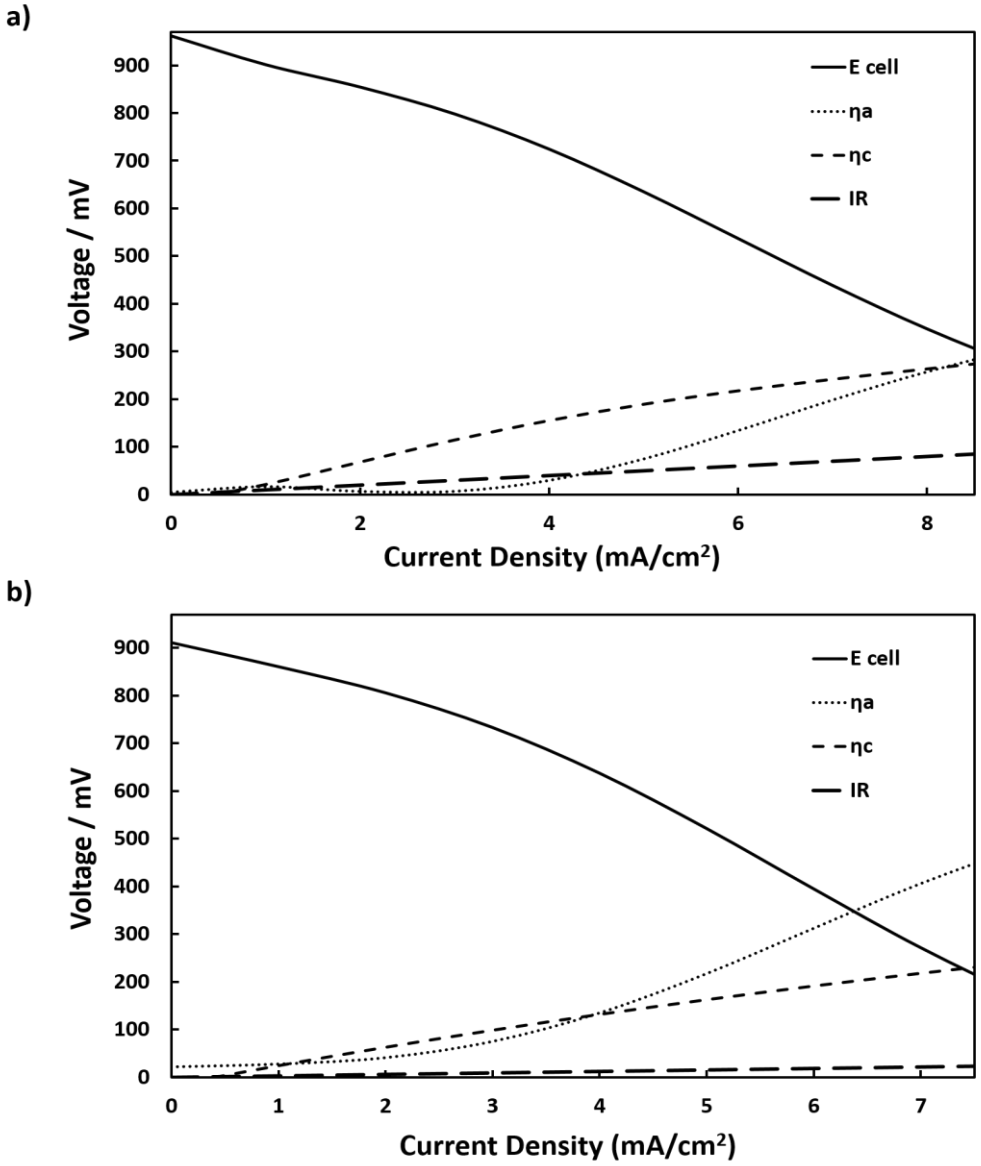

Figure 6.6: I–V curves at 700 °C and dependence of overpotentials on current density **a)** Anode: 5% H_2, Cathode: Air, **b)** Anode: 5% H_2, Cathode: 3% H_2O in air

Depending on the composition of the gas fed to the cathode side of the cell, different OCP values are obtained as shown in Figure 6.7. The current and power densities of the cells are also presented in Figure 6.7. When 5% CH_4 in argon is used at the anode, the OCPs obtained for air and 3% H_2O in air used at the cathode are 387 mV and 279 mV, respectively. By replacing 5% CH_4 in argon with 5% CO in helium at the anode 381 mV and 314 mV OCPs are obtained. The lower OCPs with respect to hydrogen (when hydrogen is used as fuel) can be explained by the decreased availability of hydrogen due to the decreased catalytic activity of anode towards reforming of methane and water–gas shift reaction. Therefore, the low OCPs cannot be attributed to the failure of the sealant as the OCP is restored to the value of about 950 mV when the fuel is switched to hydrogen.

One reason for insufficient fuel reforming could be low water permeation. Similarly, carbon monoxide poisoning of anode may be a reason for low current densities since platinum is used as anode. Adsorption of carbon monoxide on the platinum surface can decrease active surface area and thus cell performance as observed and explained by Mamlouk *et al* [157]. It is known that platinum is not a very good catalyst for steam reforming [158, 159]. Nickel would be a better catalyst for the anode of an SOFC and steam reforming, but a steam to carbon ratio of greater than two is required to avoid carbon deposition [160].

The non–linearity in the I–V curves are not observed in these cases. This might be due to lower current densities. The non–linearity in hydrogen fuel cells is observed for the current densities of above 5 mA/ cm^2. Nevertheless, the scope of this work is to investigate the possibility of directly feeding a hydrocarbon fuel to the cell to evaluate simultaneous water and oxygen transport from cathode side to anode side. Thus platinum electrodes are preferred to other materials to have more easily reproducible cells. The maximum current density obtained by using 5% CO as fuel at the anode is about two times higher than the obtained maximum current density when 5% CH_4 is used as fuel. However, the current density of the cell is also limited due to the kinetics of anode electrode reactions. More catalytically active anode and higher water permeation rate are required to achieve reasonable current densities.

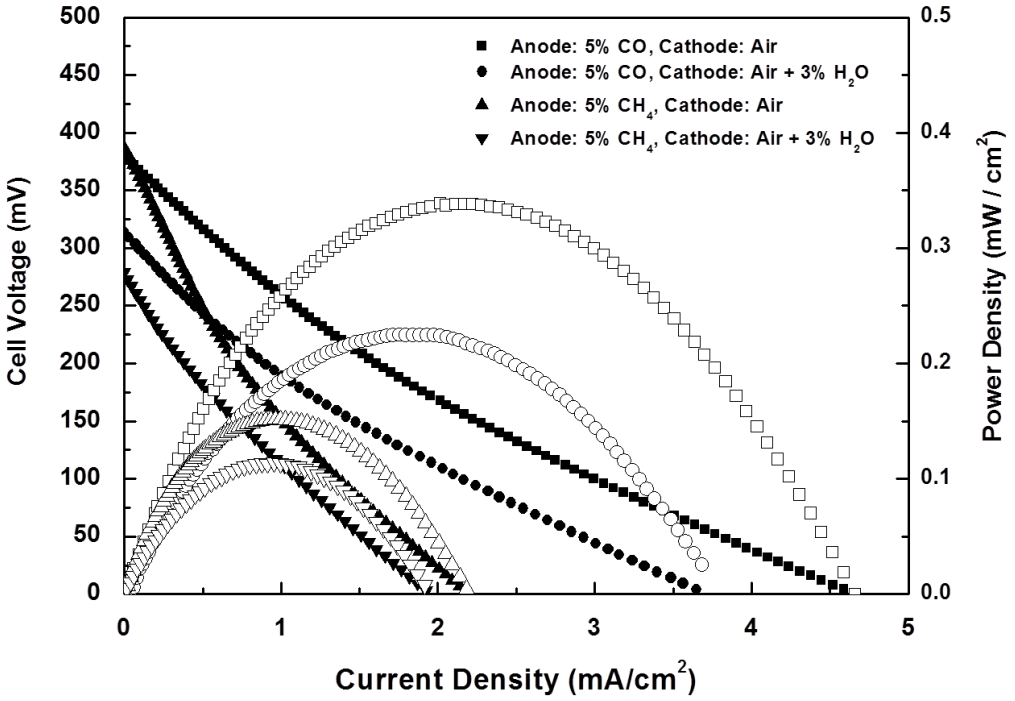

Figure 6.7: I–V–P curves at 700 °C for different anode and cathode gas compositions, (■) Anode: 5% CO, Cathode: Air, (●) Anode: 5% CO, Cathode: 3% H_2O in air, (▲) Anode: 5% CH_4, Cathode: Air, (▼) Anode: 5% CH_4, Cathode: 3% H_2O in air

The simultaneous transport of water and oxygen does not seem to interfere with each other. No vital effect is observed due to addition of water to air at the cathode side. However, a performance loss is observed in the cell, possibly due to a decrease in oxygen partial pressure. Results suggest that water may be added and transported simultaneously with oxygen so as to assist in–situ reforming of hydrocarbon fuels. However, the partial pressure of oxygen should be kept the constant. Also, the water permeation capability of the membrane needs to be optimised.

6.5 Summary

The impact of simultaneous water and oxygen transport from cathode side to anode side of the cell on water and oxygen evolution under polarisation is investigated. The water evolution is found independent of externally applied potential until a decomposition potential is reached. It is also found that transport of oxygen and water are in the same direction and is not purely independent. Results suggest that pumping of oxygen in the same direction as the water concentration gradient increases water evolution slightly at the anode side. By applying the same potential range to the cell when 3% H_2O in air is present at the cathode side decreases the current and oxygen evolution at the anode side compared with no water in air at the cathode side. The decrease in current and oxygen evolution is due to the presence of water at the cathode which in turn reduces oxygen partial pressure. Additionally, water may block diffusion of adsorbed oxygen towards three phase boundary and consume oxygen vacancies at the surface to form hydroxyl groups. This will lead to a decrease in the number available oxygen vacancies for oxygen incorporation. Thus, the reason for decrease in oxygen evolution could be a combination of multi–process rather than one parameter.

Finally, a single solid oxide fuel cell is prepared and tested with only air and 3% H_2O in air gas compositions at the cathode side. A range of fuels (i.e. hydrogen, carbon monoxide, methane) is used at the anode. A decrease in cell performance is observed for all studied cells. This may be due to slow kinetics of the anode reactions and macro scale water permeation. The performances of fuel cells are low compared to conventional SOFCs. Moreover, the visual post operational inspection of the cell revealed carbon deposition occurred during the process.

Chapter 7
Conclusions and Suggested Future Work

7.1 Overall Conclusions

The main aim of this study is to investigate the water permeation feature of yttrium–doped barium cerate perovskite membrane as an electrolyte material for intermediate temperature solid oxide fuel cells to be operated with simultaneous water permeation. BCY20 perovskite material is selected as potential electrolyte for this purpose due to its mixed ionic conductivity along with water permeation capability. Deep understanding of mechanism will allow rational design of cells for improved water permeation and cell performances.

A model is developed for hydration of BCY membranes and successfully applied for calculating diffusion coefficients of protonic defects and oxygen vacancies using the Nernst–Planck equation. The transient behaviour of electrical potential during hydration of the membrane is obtained by changing the surrounding atmosphere. The data are in good agreement with the model. The diffusion coefficients of protonic defects are found to be greater than the diffusion coefficient of oxygen vacancies which is in agreement with the literature. However, they are one order magnitude higher than the values reported in the literature which may be attributed to grain boundary effects. The concentration distributions of protonic defects, oxygen vacancies and electric potential are obtained as a function of time and space. The concentration of protonic defects increased rapidly at the hydration surface with the introduction of water into the reaction chamber indicating that formation of protonic defects is a fast process.

The study continued investigating the water permeation behaviour through BCY20 membrane modified with platinum at temperatures between 500–800 °C. Platinum is applied on one, both or no surfaces of the membrane. Water flux across the membrane is enhanced when platinum is applied on the feed side surface of the membrane, suggesting that platinum increases reaction kinetics for water adsorption and/or dissociation and/or water incorporation into the membrane. Results also indicate that protonic defects could be the minority defects on this surface. However, it is found that the presence of platinum on the permeate side surface decreases the water flux by about one third. This could be attributed to the fact that platinum partially blocks water recombination by reducing the number of active sites for water recombination via decreasing the available surface area or due to low ionic conductivity of platinum.

In addition, similar experiments are performed using modified membranes with platinum in order to investigate membrane based water permeation coupled with water–gas shift reaction at a fixed temperature in one membrane reactor. The findings suggest that the presence of a reducing gas on the permeate side increases the water flux by a factor of about 1.5. The presence of reducing gas seems to promote the driving force for diffusion of lattice oxygen from feed side to permeate side across the membrane.

Pt|BCY20 membrane configuration showed the best performance in terms of the rate of product formation. While the fluxes that are obtained seem to still very low for real world applications, it is important to prove the concept in order to improve membrane performance in terms of water permeation for final use of this phenomenon. Post operational material characterisation of the membranes revealed that BCY20 lost most of its crystal structure and decomposed to $BaCO_3$ and CeO_2 when bare surface of the membrane is subjected to feed and permeate side gas compositions. The morphology of platinum layer also changed after reaction. The SEM images exhibited agglomeration of platinum and EDXS analysis demonstrated carbon content on the permeate side membrane surfaces in the presence of platinum. As a result, platinum is not suggested to be used as an electrode/catalyts on the permeate side of the membrane.

The simultaneous water and oxygen transport through BCY20 membrane from cathode side to anode side for a working solid oxide fuel cell is then carried out. Firstly, the role of oxygen transport on water flux is investigated. The results indicate that pumping oxygen from cathode side to anode side increases water flux slightly at 700 °C when helium is fed to anode side and 3% water in air is fed to the cathode side. Subsequently, the presence of water on oxygen transport is studied by introducing 3% water in air to the cathode side while the anode side is fed with helium. The results are compared with no water in air at the cathode side. It is observed that the presence of water in air at the cathode side decreases oxygen transport from cathode side to anode side slightly. The oxygen transport rate when only air is present at the cathode side is greater than the oxygen transport rate when 3% water is present in air. One possible explanation for this decrease might be a reduction in oxygen partial pressure at the anode side. Additionally, water may reduce the active sites for oxygen incorporation into the electrolyte. Results suggest that water incorporation and evolution are much favourable than oxygen incorporation and evolution.

The fuel cell operations with simultaneous water permeation using various fuels, i.e. hydrogen, carbon monoxide, methane are further carried out. The open circuit potentials of the cells decrease when water is introduced to the cathode side for all kinds of fuels that are used. This could be also due to the change in oxygen partial pressure at the cathode side. Moreover, the fuel cells performances are significantly affected by the electrode polarisations. The overall fuel cell performances are found to be limited by slow kinetics of the anode reactions when carbon monoxide or methane is used as fuels at the anode side. This can be explained by insufficient fuel reforming due to low water permeation from cathode side to anode side and low catalytic activity of anode towards reforming of methane and water–gas shift reaction.

In conclusion, in order to utilise this specific water permeable membrane in a working solid oxide fuel cell, the electrodes should be designed to optimise water permeation. The electrolyte thickness also needs to be minimised. Platinum would be beneficial on the water surface, on the other hand, permeate surface should have sufficient uncovered areas for water recombination when platinum is used on this surface. Moreover, a protective layer is required in CO_2 environment since post operation analysis suggests that the membrane decomposes in CO_2 containing environment even at ppm levels.

7.2 Suggested Future Work

The obtained results in this study suggest several avenues for further research. For instance, the mathematical model can be developed further so as to obtain charge distribution within the membranes during transient state. This might require addition of Poisson equation to the model. Moreover, it is predicted that there is the presence of a third charge carrier in the actual membrane system, which brings complications. This point is commonly ignored in the literature and can be considered for better predictive modelling.

In order to compare water fluxes for Pt|BCY20|Pt and BCY20|Pt membranes and understand the role of platinum on this surface for water recombination, the platinum layer should be well controlled and characterised. The thickness and porosity of platinum can be controlled by using pulsed laser deposition technique. This will allow designing electrode structures that can provide adequate surface area available for water recombination resulting in optimised water permeation for fuel cell applications. Also, other electrode materials can be tested that offer better porosity and ionic conductivity on the permeate side rather than platinum for practical applications.

X–ray photoelectron spectroscopy (XPS) may be used to analyse these platinum surfaces before and after operation to identify oxygen on the surface (Oxygen may be the reason for blocking mechanism, discussed in *Section 5.3*). Another possible study would involve using isotopically labelled water in order to investigate whether protons exchange partner oxygen on the permeate surface to form water.

In this study BCY20 membranes showed poor chemical stability during water permeation coupled with water–gas shift reaction. This could be easily avoided by applying a thin protective layer without compromising the conductivity of the electrolyte. For instance, it was reported that application of a thin layer of barium zirconate by pulsed layer deposition on barium cerate improved its chemical stability without compromising the its conductivity [161]. A protective layer can be placed at the cathode side and a further water reactivity test can be carried out.

Finally, in order to perform simultaneous water and oxygen transport for operation of a SOFC coupled with water permeation platinum electrodes are used for benchmark studies to identify the main stages of the process. However, it is found that the fuel cell performances are limited due to slow kinetics of anode reactions. Therefore, explorations of better anode materials are needed to improve fuel cell performance. Nickel alloys can be applied as anodes and are expected to perform better in terms of reforming reactions. However, the impact of metal electrode (platinum in this study) on water recombination should be taken into account as well.

References

1. Larminie, J. and A. Dicks, *Fuel Cell Systems Explained*. 2003, West Sussex: Wiley.
2. Yamamoto, O., *Solid oxide fuel cells: fundamental aspects and prospects.* Electrochimica Acta, 2000. **45**(15–16): p. 2423-2435.
3. Kilner, J.A. and M. Burriel, *Materials for Intermediate-Temperature Solid-Oxide Fuel Cells.* Annual Review of Materials Research, 2014. **44**(1): p. 365-393.
4. Ormerod, R.M., *Solid oxide fuel cells.* Chemical Society Reviews, 2003. **32**(1): p. 17-28.
5. Mahato, N., et al., *Progress in material selection for solid oxide fuel cell technology: A review.* Progress in Materials Science, 2015. **72**: p. 141-337.
6. Yang, L., et al., *Promotion of water-mediated carbon removal by nanostructured barium oxide/nickel interfaces in solid oxide fuel cells.* Nat Commun, 2011. **2**: p. 357.
7. Achenbach, E., *Three-dimensional and time-dependent simulation of a planar solid oxide fuel cell stack.* Journal of Power Sources, 1994. **49**(1–3): p. 333-348.
8. Achenbach, E. and E. Riensche, *Methane/steam reforming kinetics for solid oxide fuel cells.* Journal of Power Sources, 1994. **52**(2): p. 283-288.
9. Janardhanan, V.M., V. Heuveline, and O. Deutschmann, *Performance analysis of a SOFC under direct internal reforming conditions.* Journal of Power Sources, 2007. **172**(1): p. 296-307.
10. Bonanos, N., et al., *Ionic conductivity of gadolinium-doped barium cerate perovskites.* Solid State Ionics, 1989. **35**(1–2): p. 179-188.
11. Bonanos, N., K.S. Knight, and B. Ellis, *Perovskite solid electrolytes: Structure, transport properties and fuel cell applications.* Solid State Ionics, 1995. **79**(0): p. 161-170.
12. Iwahara, H., *Technological challenges in the application of proton conducting ceramics.* Solid State Ionics, 1995. **77**(0): p. 289-298.
13. Thursfield, A. and I.S. Metcalfe, *High temperature gas separation through dual ion-conducting membranes.* Current Opinion in Chemical Engineering, 2013. **2**(2): p. 217-222.
14. Kreuer, K.D., *Proton Conducting oxides.* Annual Review of Materials Research, 2003. **33**(1): p. 333-359.

15. Kreuer, K.D., et al., *Water solubility, proton and oxygen diffusion in acceptor doped $BaCeO_3$: A single crystal analysis.* Solid State Ionics, 1996. **86–88, Part 1**(0): p. 613-620.
16. Knight, K.S., *Structural phase transitions in $BaCeO_3$.* Solid State Ionics, 1994. **74**(3–4): p. 109-117.
17. Takeuchi, K., et al., *The crystal structures and phase transitions in Y-doped $BaCeO_3$: their dependence on Y concentration and hydrogen doping.* Solid State Ionics, 2000. **138**(1–2): p. 63-77.
18. Tong, J., et al., *Proton-conducting yttrium-doped barium cerate ceramics synthesized by a cost-effective solid-state reactive sintering method.* Solid State Ionics, 2010. **181**(33–34): p. 1486-1498.
19. Malavasi, L., C. Ritter, and G. Chiodelli, *Correlation between Thermal Properties, Electrical Conductivity, and Crystal Structure in the $BaCe_{0.8}Y_{0.2}O_{2.9}$ Proton Conductor.* Chemistry of Materials, 2008. **20**(6): p. 2343-2351.
20. W. Grover Coors and R. Swartzlander, *Partial Conductivity Measurements in $BaCe_{0.9}Y_{0.1}O_{3-\delta}$ by Impedance Spectroscopy.* Proceedings of the 26th Risø International Symposium on Materials Science Solid State Electrochemistry, 2005(September): p. 185-196.
21. Bjorheim, T.S., T. Norby, and R. Haugsrud, *Hydration and proton conductivity in $LaAsO_4$.* Journal of Materials Chemistry, 2012. **22**(4): p. 1652-1661.
22. Kjølseth, C., et al., *Determination of the enthalpy of hydration of oxygen vacancies in Y-doped $BaZrO_3$ and $BaCeO_3$ by TG-DSC.* Solid State Ionics, 2010. **181**(39–40): p. 1740-1745.
23. Hancke, R., et al., *Hydration of lanthanum tungstate (La/W=5.6 and 5.3) studied by TG and simultaneous TG–DSC.* Solid State Ionics, 2013. **231**: p. 25-29.
24. Guan, B., et al., *A Performance Study of Solid Oxide Fuel Cells With $BaZr_{0.1}Ce_{0.7}Y_{0.2}O_{3-\delta}$ Electrolyte Developed by Spray-Modified Pressing Method.* Fuel Cells, 2012. **12**(1): p. 141-145.
25. Guo, Y., R. Ran, and Z. Shao, *Optimizing the modification method of zinc-enhanced sintering of $BaZr_{0.4}Ce_{0.4}Y_{0.2}O_{3-\delta}$ based electrolytes for application in an anode-supported protonic solid oxide fuel cell.* International Journal of Hydrogen Energy, 2010. **35**(11): p. 5611-5620.
26. Sun, W., et al., *Evaluation of $BaZr_{0.1}Ce_{0.7}Y_{0.2}O_{3-\delta}$-based proton-conducting solid oxide fuel cells fabricated by a one-step co-firing process.* Electrochimica Acta, 2011. **56**(3): p. 1447-1454.

27. Liu, M., et al., *High performance of anode supported $BaZr_{0.1}Ce_{0.7}Y_{0.2}O_{3-\delta}$(BZCY) electrolyte cell for IT-SOFC.* International Journal of Hydrogen Energy, 2011. **36**(21): p. 13741-13745.
28. Nien, S.H., et al., *Preparation of $BaZr_{0.1}Ce_{0.7}Y_{0.2}O_{3-\delta}$ based Solid Oxide Fuel Cells with Anode Functional Layers by Tape Casting.* Fuel Cells, 2011. **11**(2): p. 178-183.
29. Xie, K., et al., *A simple and easy one-step fabrication of thin $BaZr_{0.1}Ce_{0.7}Y_{0.2}O_{3-\delta}$ electrolyte membrane for solid oxide fuel cells.* Journal of Membrane Science, 2008. **325**(1): p. 6-10.
30. Yang, L., C. Zuo, and M. Liu, *High-performance anode-supported Solid Oxide Fuel Cells based on $BaZr_{0.1}Ce_{0.7}Y_{0.2}O_{3-\delta}$ (BZCY) fabricated by a modified co-pressing process.* Journal of Power Sources, 2010. **195**(7): p. 1845-1848.
31. Zhao, L., et al., *High performance of proton-conducting solid oxide fuel cell with a layered $PrBaCo_2O_{5+\delta}$ cathode.* Journal of Power Sources, 2009. **194**(2): p. 835-837.
32. Zhao, L., et al., *Micro-tubular solid oxide fuel cells with graded anodes fabricated with a phase inversion method.* Journal of Power Sources, 2011. **196**(3): p. 962-967.
33. Viswanathan, B., Aulice Scibioh, M *Fuel Cells Principles and Applications*. 2007, India: CRC Press.
34. *Recent Trends in Fuel Cell Science and Technology*. 2007, New Delhi. India: Anamaya Publishers.
35. Inc., P., *Fuel Cell Handbook 5th Edition*. 2000: EG and G Services Parsons.
36. F, B., *PEM Fuel Cells: Theory and Practice*. 2005, London: Elsevier Academic Press.
37. Haile, S., *Fuel Cell Materials and Components.* Acta Mater, 2003. **51**(19): p. 5981-6000.
38. Kawamato, H., *Research and Development Trends in Solid Oxide Fuel Cell Materials.* Science and Technology Trends 2008. **26**.
39. Ellamla, H.R., et al., *Current status of fuel cell based combined heat and power systems for residential sector.* Journal of Power Sources, 2015. **293**: p. 312-328.
40. Sammes, N., R. Bove, and K. Stahl, *Phosphoric acid fuel cells: Fundamentals and applications.* Current Opinion in Solid State and Materials Science, 2004. **8**(5): p. 372-378.
41. Barbir, F., *PEM Fuel Cells Theory and Practice*. 2005, London: Elsevier Academic Press.
42. Yano, S., et al., *Solid Oxide Fuel Cell with Anodes using Proton Conductor (Barium-Cerium/Yttrium Oxide).* Journal of Thermal Science and Technology, 2009. **4**(3): p. 431-436.

43. Singh, P. and N.Q. Minh, *Solid Oxide Fuel Cells: Technology Status.* International Journal of Applied Ceramic Technology, 2004. **1**(1): p. 5-15.
44. Rayment, C. and S. Sherwin, *Introduction to Fuel Cell Technology*. Vol. 2012. May 2003, Notre Dame, IN 46556, U.S.A.: Department of Aerospace and Mechanical Engineering, University of Notre Dame.
45. Singhal, S.C. and K. Kendall, *High Temperature Solid Oxide Fuel Cells: Fundamentals, Design and Applications*. 2003, Oxford: Elsevier.
46. Hoogers, G., *Fuel Cell Technology Handbook*. 2002, CRC Press.
47. Jacobson, A.J., *Materials for Solid Oxide Fuel Cells.* Chemistry of Materials, 2010. **22**(3): p. 660-674.
48. Liu, Y., et al., *Significant performance enhancement of yttrium-doped barium cerate proton conductor as electrolyte for solid oxide fuel cells through a Pd ingress–egress approach.* Journal of Power Sources, 2014. **257**: p. 308-318.
49. Orera, A. and P.R. Slater, *New Chemical Systems for Solid Oxide Fuel Cells.* Chemistry of Materials, 2010. **22**(3): p. 675-690.
50. Mogensen, M., et al., *Factors controlling the oxide ion conductivity of fluorite and perovskite structured oxides.* Solid State Ionics, 2004. **174**(1–4): p. 279-286.
51. Aguadero, A., et al., *Materials development for intermediate-temperature solid oxide electrochemical devices.* Journal of Materials Science, 2012. **47**(9): p. 3925-3948.
52. Kharton, V.V., F.M.B. Marques, and A. Atkinson, *Transport properties of solid oxide electrolyte ceramics: a brief review.* Solid State Ionics, 2004. **174**(1–4): p. 135-149.
53. Manthiram, A., et al., *Crystal chemistry and properties of mixed ionic-electronic conductors.* Journal of Electroceramics, 2011. **27**(2): p. 93-107.
54. Kharton, V., *Solid State Electrochemistry I, Fundamentals, Materials and their Applications*. 2009, Weinheim: WILEY-VCH.
55. V.Thangadurai, W.H.K., B.Mirfakhraei, S.S. Bhella, and T.T. Trinh, *Materials for Proton Conducting Solid Oxide Fuel Cells.* The Electrochemical Society, 2011. **35**(1): p. 483-492.
56. Sanders, M.D., *The Role of Multi-Species Transport in Proton-Conducting Perovskite Permeation Membranes*, in *Colorado School of Mines*. 2013: Golden, Colorado.
57. *The CRC Handbook of Solid State Electrochemistry*, ed. P.Gellings and H.M.Bouwmeester. 1997, New York: CRC Press.
58. Gellings, P.J. and H.J.M. Bouwmeester, *Solid state aspects of oxidation catalysis.* Catalysis Today, 2000. **58**(1): p. 1-53.

59. Fabbri, E., D. Pergolesi, and E. Traversa, *Materials challenges toward proton-conducting oxide fuel cells: a critical review.* Chemical Society Reviews, 2010. **39**(11): p. 4355-4369.
60. Norby, T., *Protonic defects in oxides and their possible role in high temperature oxidation.* J. Phys. IV France, 1993. **03**(C9): p. C9-99-C9-106.
61. Madhavan, B. and A. Ashok, *Review on nanoperovskites: materials, synthesis, and applications for proton and oxide ion conductivity.* Ionics, 2015. **21**(3): p. 601-610.
62. Iwahara, H., et al., *Proton conduction in sintered oxides and its application to steam electrolysis for hydrogen production.* Solid State Ionics, 1981. **3–4**(0): p. 359-363.
63. Liu, Y., X. Tan, and K. Li, *Mixed Conducting Ceramics for Catalytic Membrane Processing.* Catalysis Reviews, 2006. **48**(2): p. 145-198.
64. Babilo, P., T. Uda, and S.M. Haile, *Processing of yttrium-doped barium zirconate for high proton conductivity.* Journal of Materials Research, 2007. **22**(05): p. 1322-1330.
65. Jacobson, A.J., B.C. Tofield, and B.E.F. Fender, *The structures of $BaCeO_3$, $BaPrO_3$ and $BaTbO_3$ by neutron diffraction: lattice parameter relations and ionic radii in O-perovskites.* Acta Crystallographica Section B, 1972. **28**(3): p. 956-961.
66. Bonanos, N. and F. Willy Poulsen, *Considerations of defect equilibria in high temperature proton-conducting cerates.* Journal of Materials Chemistry, 1999. **9**(2): p. 431-434.
67. Norby, T., *Solid-state protonic conductors: principles, properties, progress and prospects.* Solid State Ionics, 1999. **125**(1–4): p. 1-11.
68. Guan, J., et al., *The Effects of Dopants and A:B Site Nonstoichiometry on Properties of Perovskite‐Type Proton Conductors.* Journal of The Electrochemical Society, 1998. **145**(5): p. 1780-1786.
69. Tauer, T., R. O'Hayre, and J.W. Medlin, *A theoretical study of the influence of dopant concentration on the hydration properties of yttrium-doped barium cerate.* Solid State Ionics, 2011. **204–205**(0): p. 27-34.
70. Sawant, P., et al., *Influence of synthesis route on morphology and conduction behavior of $BaCe_{0.8}Y_{0.2}O_{3-\delta}$.* Journal of Thermal Analysis and Calorimetry, 2012. **107**(1): p. 189-195.
71. Nikodemski, S., J. Tong, and R. O'Hayre, *Solid-state reactive sintering mechanism for proton conducting ceramics.* Solid State Ionics, 2013. **253**(0): p. 201-210.
72. Subramaniyan, A., et al., *Sintering Studies on 20 mol% Yttrium-Doped Barium Cerate.* Journal of the American Ceramic Society, 2011. **94**(6): p. 1800-1804.

73. Tomita, A., et al., *Chemical and redox stabilities of a solid oxide fuel cell with $BaCe_{0.8}Y_{0.2}O_{3-\alpha}$ functioning as an electrolyte and as an anode.* Solid State Ionics, 2006. **177**(33–34): p. 2951-2956.
74. Coors, W., *Protonic ceramic steam-permeable membranes.* Solid State Ionics, 2007. **178**(7-10): p. 481-485.
75. Coors, W.G., *Protonic ceramic fuel cells for high-efficiency operation with methane.* Journal of Power Sources, 2003. **118**(1-2): p. 150-156.
76. Kan, H. and H. Lee, *Sn-doped Ni/YSZ anode catalysts with enhanced carbon deposition resistance for an intermediate temperature SOFC.* Applied Catalysis B: Environmental, 2010. **97**(1–2): p. 108-114.
77. Eguchi, K., *Performance and Degradation of Ni-based Cermet Anode for Solid Oxide Fuel Cells.* Journal of the Japan Petroleum Institute, 2015. **58**(2): p. 79-85.
78. Cui, S.-H., et al., *Effects of H_2S and H_2O on carbon deposition over $La_{0.4}Sr_{0.5}Ba_{0.1}TiO_3$/YSZ perovskite anodes in methane fueled SOFCs.* Journal of Power Sources, 2014. **250**(0): p. 134-142.
79. Gao, J., et al., *A thermodynamic analysis of methanation reactions of carbon oxides for the production of synthetic natural gas.* RSC Advances, 2012. **2**(6): p. 2358-2368.
80. Dehimi, S., et al., *Thermal field under the effect of the chemical reaction of a direct internal reforming solid oxide fuel cell DIR-SOFC.* International Journal of Hydrogen Energy, 2014. **39**(27): p. 15261-15265.
81. W. Grover, C., *Protonic ceramic steam-permeable membranes.* Solid State Ionics, 2007. **178**(7-10): p. 481-485.
82. Kreuer, K.D., E. Schönherr, and J. Maier, *Proton and oxygen diffusion in $BaCeO_3$ based compounds: A combined thermal gravimetric analysis and conductivity study.* Solid State Ionics, 1994. **70–71, Part 1**(0): p. 278-284.
83. Kreuer, K.D., et al., *Proton conducting alkaline earth zirconates and titanates for high drain electrochemical applications.* Solid State Ionics, 2001. **145**(1–4): p. 295-306.
84. Medvedev, D., et al., *$BaCeO_3$: Materials development, properties and application.* Progress in Materials Science, 2014. **60**(0): p. 72-129.
85. Micheal D. Sanders, R.O.H., W.Grover Coors, *Modelling of Material Parameters for Increased Steam-Permeation in Yttrium-Doped Barium Cerate Ceramic Membranes.* Proceedings of FUELCELL2008, 6th International Fuel Cell Science, Engineering and Technology Conference, 2008.
86. Kreuer, K.D., *Aspects of the formation and mobility of protonic charge carriers and the stability of perovskite-type oxides.* Solid State Ionics, 1999. **125**(1–4): p. 285-302.

87. Ricote, S., N. Bonanos, and G. Caboche, *Water vapour solubility and conductivity study of the proton conductor $BaCe_{(0.9-x)}Zr_xY_{0.1}O_{(3-\delta)}$*. Solid State Ionics, 2009. **180**(14-16): p. 990-997.

88. Norby, T., et al., *Hydrogen in oxides.* Dalton Transactions, 2004(19): p. 3012-3018.

89. Yamazaki, Y., C.-K. Yang, and S.M. Haile, *Unraveling the defect chemistry and proton uptake of yttrium-doped barium zirconate.* Scripta Materialia, 2011. **65**(2): p. 102-107.

90. Schober, T. and H.G. Bohn, *Water vapor solubility and electrochemical characterization of the high temperature proton conductor $BaZr_{0.9}Y_{0.1}O_{2.95}$*. Solid State Ionics, 2000. **127**(3–4): p. 351-360.

91. Oishi, M., et al., *Defect structure analysis of B-site doped perovskite-type proton conducting oxide $BaCeO_3$: Part 2: The electrical conductivity and diffusion coefficient of $BaCe_{0.9}Y_{0.1}O_{3-\delta}$.* Solid State Ionics, 2008. **179**(39): p. 2240-2247.

92. Kreuer, K.D., et al., *Defect interactions in proton conducting perovskite-type oxides.* Berichte der Bunsengesellschaft/Physical Chemistry Chemical Physics, 1997. **101**(9): p. 1344-1350.

93. Grimaud, A., et al., *Transport properties and in-situ Raman spectroscopy study of $BaCe_{0.9}Y_{0.1}O_{3-\delta}$ as a function of water partial pressures.* Solid State Ionics, 2011. **191**(1): p. 24-31.

94. Manning, P.S., J.D. Sirman, and J.A. Kilner, *Oxygen self-diffusion and surface exchange studies of oxide electrolytes having the fluorite structure.* Solid State Ionics, 1996. **93**(1–2): p. 125-132.

95. Liu, J., et al., *Oxygen surface exchange and diffusion studies of $La_2Mo_2O_9$ in different exchange atmospheres.* Solid State Ionics, 2011. **189**(1): p. 39-44.

96. [cited 2016 20/1/2016]; Available from: http://products.inficon.com/GetAttachment.axd?attaName=TSP2+TechNote+Calculating+Partial+P.

97. Niemantsverdriet, J.W., *Spectroscopy in Catalysis: An Introduction*. 2000: John Wiley & Sons.

98. Atkins, P.W., *Physical Chemistry*. 1994, Oxford: Oxford University Press.

99. Michael Dunlap, J.E.A. *Introduction to the Scanning Electron Microscope, Theory, Practice, & Procedures*. 1997 08/08/2012]; Available from: https://imf.ucmerced.edu/downloads/semmanual.pdf.

100. J. Goldstein, D.E.N., D. C. Joy, P. Echlin, C. E. Lyman, E. Lifshin, L.Sawyer, J. Micheal, *Scanning Electron Microscopy and X-ray Microanalysis*. 2003, New York: Kluwer Academic / Plenum Publishers.

101. Qi, X., F.T. Akin, and Y.S. Lin, *Ceramic–glass composite high temperature seals for dense ionic-conducting ceramic membranes.* Journal of Membrane Science, 2001. **193**(2): p. 185-193.
102. Masliyah, J.H. and S. Bhattacharjee, *Fundamental Transport Equations*, in *Electrokinetic and Colloid Transport Phenomena*. 2005, John Wiley & Sons, Inc. p. 179-220.
103. Kuzmin, D., *A Guide to Numerical Methods for Transport Equations*. 2010, Erlangen-Nürnberg: Friedrich-Alexander Universitat.
104. Shirai, T., H. Watanabe, and M. Fuji, *Structural properties and surface characteristics on aluminum oxide powders.* Annual report of the Ceramics Research Laboratory, Nagoya Institute of Technology, 2009. **9**: p. 23-31.
105. Schober, T. and W.G. Coors, *Entry and exit of water vapor in bulk ceramic proton conductors.* Solid State Ionics, 2005. **176**(3–4): p. 357-362.
106. Yoo, H.-I., et al., *Hydration and oxidation kinetics of a proton conductor oxide, $SrCe_{0.95}Yb_{0.05}O_{2.975}$.* Physical Chemistry Chemical Physics, 2008. **10**(7): p. 974-982.
107. Yoo, H.-I., J.I. Yeon, and J.-K. Kim, *Mass relaxation vs. electrical conductivity relaxation of a proton conducting oxide upon hydration and dehydration.* Solid State Ionics, 2009. **180**(28–31): p. 1443-1447.
108. Yoo, H.-I. and C.-E. Lee, *Conductivity relaxation patterns of mixed conductor oxides under a chemical potential gradient.* Solid State Ionics, 2009. **180**(4–5): p. 326-337.
109. *The KaleidaGraph Guide to Curve Fitting*. 18/1/2016]; Available from: http://www.synergy.com/Tools/curvefitting.pdf.
110. Kee, R.J., et al., *Modeling the Steady-State and Transient Response of Polarized and Non-Polarized Proton-Conducting Doped-Perovskite Membranes.* Journal of The Electrochemical Society, 2013. **160**(3): p. F290-F300.
111. Vøllestad, E., H. Zhu, and R.J. Kee, *Interpretation of Defect and Gas-Phase Fluxes through Mixed-Conducting Ceramics Using Nernst–Planck–Poisson and Integral Formulations.* Journal of The Electrochemical Society, 2014. **161**(1): p. F114-F124.
112. Kostøl, K.B., A. Magrasó, and T. Norby, *On the hydration of grain boundaries and bulk of proton conducting $BaZr_{0.7}Pr_{0.2}Y_{0.1}O_{3-\delta}$.* International Journal of Hydrogen Energy, 2012. **37**(9): p. 7970-7974.
113. Kreuer, K.D., *On the development of proton conducting materials for technological applications.* Solid State Ionics, 1997. **97**(1–4): p. 1-15.

114. Coors, W.G. and D.W. Readey, *Proton Conductivity Measurements in Yttrium Barium Cerate by Impedance Spectroscopy.* Journal of the American Ceramic Society, 2002. **85**(11): p. 2637-2640.

115. Hung, I.M., et al., *Phase stability and conductivity of $Ba_{1-y}Sr_yCe_{1-x}Y_xO_{3-\delta}$ solid oxide fuel cell electrolyte.* Journal of Power Sources, 2009. **193**(1): p. 155-159.

116. Zakowsky, N., S. Williamson, and J.T.S. Irvine, *Elaboration of CO_2 tolerance limits of $BaCe_{0.9}Y_{0.1}O_{3-\delta}$ electrolytes for fuel cells and other applications.* Solid State Ionics, 2005. **176**(39–40): p. 3019-3026.

117. Fu, X.-Z., et al., *Y-doped $BaCeO_{3-\delta}$ nanopowders as proton-conducting electrolyte materials for ethane fuel cells to co-generate ethylene and electricity.* Journal of Power Sources, 2010. **195**(9): p. 2659-2663.

118. Merkle, R. and J. Maier, *How Is Oxygen Incorporated into Oxides? A Comprehensive Kinetic Study of a Simple Solid-State Reaction with $SrTiO_3$ as a Model Material.* Angewandte Chemie International Edition, 2008. **47**(21): p. 3874-3894.

119. Leonhardt, M., et al., *Surface Kinetics of Oxygen Incorporation into $SrTiO_3$.* Journal of The Electrochemical Society, 2002. **149**(2): p. J19-J26.

120. Yu, J.H., J.-S. Lee, and J. Maier, *Peculiar Nonmonotonic Water Incorporation in Oxides Detected by Local In Situ Optical Absorption Spectroscopy.* Angewandte Chemie International Edition, 2007. **46**(47): p. 8992-8994.

121. Mather, G.C., et al., *Hydrogen-permeation characteristics of a $SrCeO_3$-based ceramic separation membrane: Thermal, ageing and surface-modification effects.* Solid State Ionics, 2010. **181**(3–4): p. 230-235.

122. Hancke, R., Z. Li, and R. Haugsrud, *The Kinetics of Hydration and H/D Isotope Exchange of Y-Doped Barium Cerate and Lanthanum Tungstate Studied by Transient Thermogravimetry.* Journal of The Electrochemical Society, 2013. **160**(8): p. F757-F763.

123. Fajín, J.L.C., M.N. D. S. Cordeiro, and J.R.B. Gomes, *Density Functional Theory Study of the Water Dissociation on Platinum Surfaces: General Trends.* The Journal of Physical Chemistry A, 2014. **118**(31): p. 5832-5840.

124. Karlberg, G.S., et al., *Water desorption from an oxygen covered Pt(111) surface: Multichannel desorption.* The Journal of Chemical Physics, 2006. **124**(20): p. 204712.

125. Vøllestad, E., et al., *Hydrogen permeation characteristics of $La_{27}Mo_{1.5}W_{3.5}O_{55.5}$.* Journal of Membrane Science, 2014. **461**: p. 81-88.

126. García-García, F.R., et al., *Studies on water–gas-shift enhanced by adsorption and membrane permeation.* Catalysis Today, 2014. **236, Part A**(0): p. 57-63.

127. Murugan, A., A. Thursfield, and I.S. Metcalfe, *A chemical looping process for hydrogen production using iron-containing perovskites.* Energy & Environmental Science, 2011. **4**(11): p. 4639-4649.

128. Evdou, A., L. Nalbandian, and V.T. Zaspalis, *Perovskite membrane reactor for continuous and isothermal redox hydrogen production from the dissociation of water.* Journal of Membrane Science, 2008. **325**(2): p. 704-711.

129. Kim, J.-H., et al., *Study on the chemical stability of Y-doped $BaCeO_{3-\delta}$ and $BaZrO_{3-\delta}$ films deposited by aerosol deposition.* Thin Solid Films, 2011. **520**(3): p. 1015-1021.

130. Li, Y., et al., *Chemical stability study of nanoscale thin film yttria-doped barium cerate electrolyte for micro solid oxide fuel cells.* Journal of Power Sources, 2014. **268**: p. 804-809.

131. Yajima, T., et al., *Protonic conduction in $SrZrO_3$-based oxides.* Solid State Ionics, 1992. **51**(1–2): p. 101-107.

132. Bhide, S.V. and A.V. Virkar, *Stability of $BaCeO_3$ - based Proton Conductors in Water - Containing Atmospheres.* Journal of The Electrochemical Society, 1999. **146**(6): p. 2038-2044.

133. Tanner, C.W. and A.V. Virkar, *Instability of $BaCeO_3$ in H_2O Containing Atmospheres.* Journal of The Electrochemical Society, 1996. **143**(4): p. 1386-1389.

134. Si, Y., et al., *CO Tolerance of Carbon-Supported Platinum-Ruthenium Catalyst at Elevated Temperature and Atmospheric Pressure in a PEM Fuel Cell.* Journal of The Electrochemical Society, 2004. **151**(11): p. A1820-A1824.

135. Ralph, T.R.H., M. P, *Catalysis for low temperature fuel cells. Part II. The anode challenges.* Platinum Metals Review, 2002. **46**(3): p. 117-135.

136. Laosiripojana, N., W. Sangtongkitcharoen, and S. Assabumrungrat, *Catalytic steam reforming of ethane and propane over CeO_2-doped Ni/Al_2O_3 at SOFC temperature: Improvement of resistance toward carbon formation by the redox property of doping CeO_2.* Fuel, 2006. **85**(3): p. 323-332.

137. Haryanto, A., et al., *Hydrogen Production through the Water−Gas Shift Reaction: Thermodynamic Equilibrium versus Experimental Results over Supported Ni Catalysts.* Energy & Fuels, 2009. **23**(6): p. 3097-3102.

138. Uchida, H., N. Maeda, and H. Iwahara, *Relation between proton and hole conduction in $SrCeO_3$-based solid electrolytes under water-containing atmospheres at high temperatures.* Solid State Ionics, 1983. **11**(2): p. 117-124.

139. Li, Y., R. Gemmen, and X. Liu, *Oxygen reduction and transportation mechanisms in solid oxide fuel cell cathodes.* Journal of Power Sources, 2010. **195**(11): p. 3345-3358.

140. J. Sunarso, S.B., J.M. Serra,W.A. Meulenberg, S. Liu, Y.S. Lin, J.C. Diniz da Costa, *Mixed ionic–electronic conducting (MIEC) ceramic-based membranes for oxygen separation.* Journal of Membrane Science, 2008. **320**: p. 13-41.

141. Baumann, F.S., *Oxygen reduction kinetics on mixed conducting SOFC model cathodes*. 2006.

142. Opitz, A.K. and J. Fleig, *Investigation of O_2 reduction on Pt/YSZ by means of thin film microelectrodes: The geometry dependence of the electrode impedance.* Solid State Ionics, 2010. **181**(15–16): p. 684-693.

143. Walch, G., et al., *Correlation between hydrogen production rate, current, and electrode overpotential in a solid oxide electrolysis cell with $La_{0.6}Sr_{0.4}FeO_{3-\delta}$ thin-film cathode.* Monatshefte für Chemie - Chemical Monthly, 2014. **145**(7): p. 1055-1061.

144. Tanaka, M., Y. Asakura, and T. Uda, *Performance of the electrochemical hydrogen pump of a proton-conducting oxide for the tritium monitor.* Fusion Engineering and Design, 2008. **83**(10–12): p. 1414-1418.

145. Sakai, N., et al., *Effect of Water on Oxygen Transport Properties on Electrolyte Surface in SOFCs: I. Surface Reaction Mechanism of Oxygen Isotope Exchange on Solid Oxide Electrolytes.* Journal of The Electrochemical Society, 2003. **150**(6): p. A689-A694.

146. Liu, J., et al., *Surface enhancement of oxygen exchange and diffusion in the ionic conductor $La_2Mo_2O_9$.* Solid State Ionics, 2010. **181**(17–18): p. 812-818.

147. Liu, J., R.J. Chater, and S.J. Skinner, *Effects of humidified atmosphere on oxygen transport properties in $La_2Mo_2O_9$.* Solid State Ionics, 2011. **192**(1): p. 444-447.

148. Guan, J., et al., *Transport properties of $BaCe_{0.95}Y_{0.05}O_{3-\alpha}$ mixed conductors for hydrogen separation.* Solid State Ionics, 1997. **100**(1–2): p. 45-52.

149. Ma, G., T. Shimura, and H. Iwahara, *Ionic conduction and nonstoichiometry in $Ba_xCe_{0.90}Y_{0.10}O_{3-\alpha}$.* Solid State Ionics, 1998. **110**(1–2): p. 103-110.

150. Ma, G., T. Shimura, and H. Iwahara, *Simultaneous doping with La^{3+} and Y^{3+} for Ba^{2+} and Ce^{4+} sites in $BaCeO_3$ and the ionic conduction.* Solid State Ionics, 1999. **120**(1–4): p. 51-60.

151. Bonanos, N., *Transport properties and conduction mechanism in high-temperature protonic conductors.* Solid State Ionics, 1992. **53**: p. 967-974.

152. Kosacki, I. and H.L. Tuller, *Mixed conductivity in $SrCe_{0.95}Yb_{0.05}O_3$ protonic conductors.* Solid State Ionics, 1995. **80**(3–4): p. 223-229.

153. Maffei, N., L. Pelletier, and A. McFarlan, *Performance characteristics of Gd-doped barium cerate-based fuel cells.* Journal of Power Sources, 2004. **136**(2): p. 24-29.

154. Fabbri, E., et al., *Tailoring the chemical stability of $Ba(Ce_{0.8-x}Zr_x)Y_{0.2}O_{3-\delta}$ protonic conductors for Intermediate Temperature Solid Oxide Fuel Cells (IT-SOFCs).* Solid State Ionics, 2008. **179**(15–16): p. 558-564.

155. Akoshima, S., et al., *Reaction kinetics on platinum electrode / yttrium-doped barium cerate interface under H_2–H_2O atmosphere.* Solid State Ionics, 2010. **181**(3–4): p. 240-248.

156. Sakai, N., et al., *Erratum to "Effect of water on electrochemical oxygen reduction at the interface between fluorite-type oxide-ion conductors and various types of electrodes".* Solid State Ionics, 2005. **176**(29–30): p. 2327-2333.

157. Mamlouk, M., T. Sousa, and K. Scott, *A High Temperature Polymer Electrolyte Membrane Fuel Cell Model for Reformate Gas.* International Journal of Electrochemistry, 2011. **2011**: p. 18.

158. Souza, M., R. Macedo Neto, and M. Schmal, *Synthesis Gas Production from Natural Gas on Supported Pt Catalysts.* Journal of Natural Gas Chemistry, 2006. **15**(1): p. 21-27.

159. McMinn, T.E., F.C. Moates, and J.T. Richardson, *Catalytic steam reforming of chlorocarbons: catalyst deactivation.* Applied Catalysis B: Environmental, 2001. **31**(2): p. 93-105.

160. Buccheri, M.A., A. Singh, and J.M. Hill, *Anode- versus electrolyte-supported Ni-YSZ/YSZ/Pt SOFCs: Effect of cell design on OCV, performance and carbon formation for the direct utilization of dry methane.* Journal of Power Sources, 2011. **196**(3): p. 968-976.

161. Fabbri, E., et al., *Design and fabrication of a chemically-stable proton conductor bilayer electrolyte for intermediate temperature solid oxide fuel cells (IT-SOFCs).* Energy & Environmental Science, 2008. **1**(3): p. 355-359.

162. Fabbri, E., et al., *Design and fabrication of a chemically-stable proton conductor bilayer electrolyte for intermediate temperature solid oxide fuel cells (IT-SOFCs).* Energy & Environmental Science, 2008. **358**(1): p. 355-359.

163. Tomita, A., et al., *Proton conduction at the surface of Y-doped $BaCeO_3$ and its application to an air/fuel sensor.* Journal of Materials Science, 2004. **39**(7): p. 2493-2497.

164. Suksamai, W., *Intermediate Temperature Operation of a Proton Conducting Solid Oxide Fuel Cell*. 2007, Manchester University.

Appendix A

The electrical conductivity of BCY20 membrane was measured using a three–electrode cell set up with a thickness of 1.55 mm BCY20 shown in Figure A.1 under single gas atmosphere over the temperature range of 500–800 °C. The flow rates of gases were 100 ml/min. The impedance spectra were obtained at amplitude of 100 mV with a frequency sweep from 500 KHz to 50 MHz for several times.

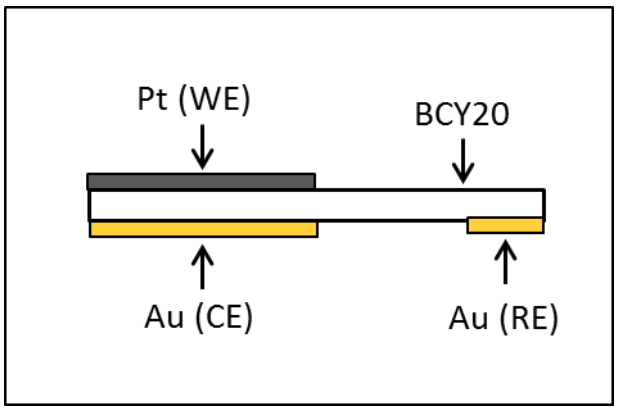

Figure A.1: Three electrode set up in a single chamber reactor for impedance measurements.

The electrical conductivity of BCY20 membrane was calculated using the following equation;

$$\sigma = \frac{l}{A \times R} \qquad 1$$

Where R represents bulk resistance, l represents the distance between the electrodes (membrane thickness), A represents affective surface area of working electrode. The high frequency region intercept with the real axis was used to obtain bulk resistance (where the impedance plot cuts the real axis). Since the bulk resistance was used to calculate electrical conductivity, the result may be assumed as bulk conductivity. The grain (medium frequency

region) and the electrodes effect (low frequency region) did not show clear division. The obtained electrical conductivity is given in Figure A.2.

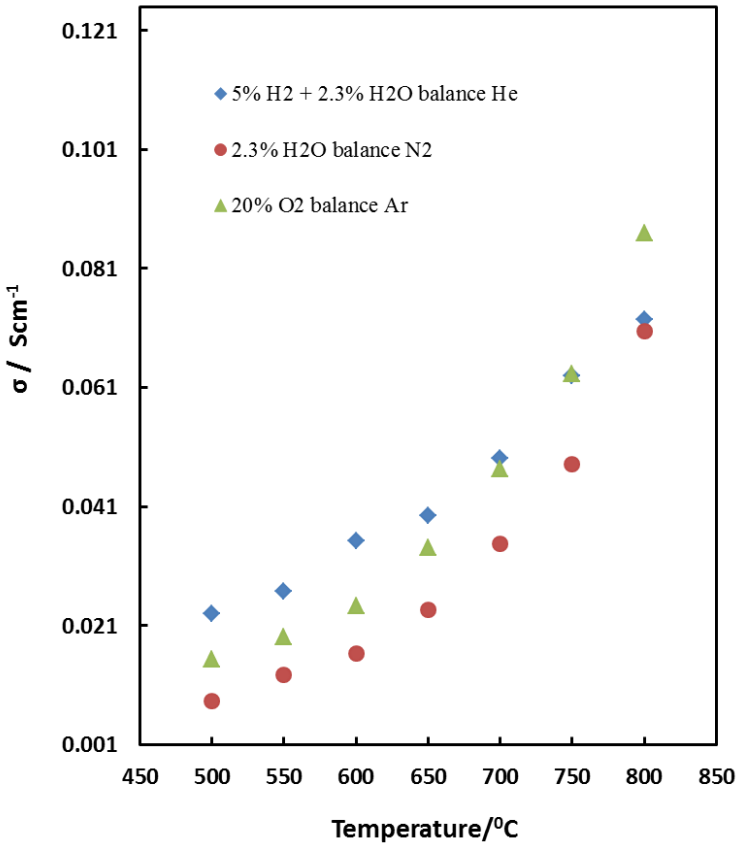

Figure A.2: The electrical conductivity of BCY20 membrane as a function of temperature. (▲) 20% O_2 balance Ar, (●) 2.3% H_2O balance N_2, (♦) 5% H_2 + 2.3% H_2O balance He.

The activation energy using the Arrhenius plot shown in Figure A.3 was calculated as ~0.35 eV for bulk conductivity (in 5% H_2 + 2.3% H_2O balance He) which is consistent with the literature [72, 162, 163].

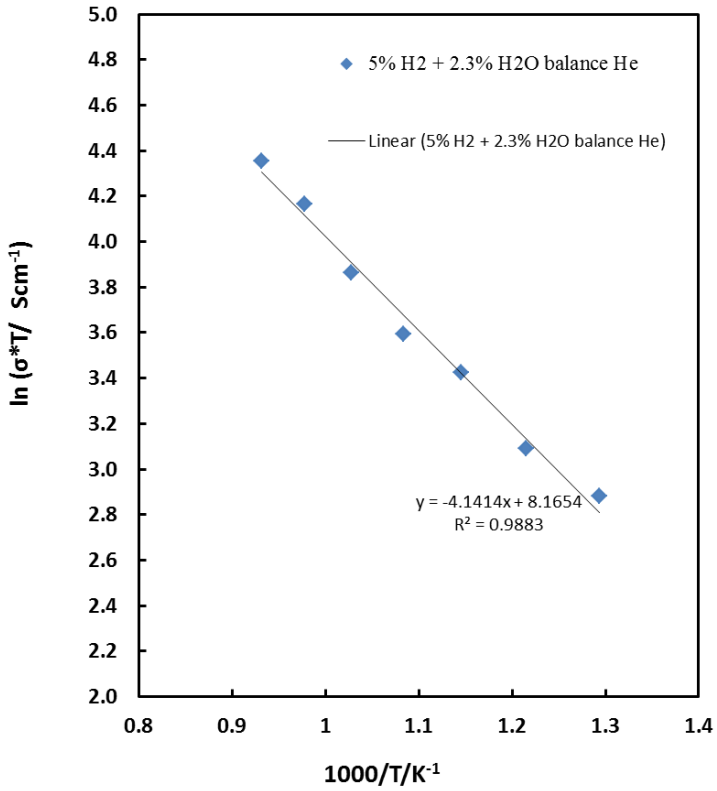

Figure A.3: The Arrhenius plot of bulk conductivity of BCY20.

The activation energy is given as:

$$k = A\, e^{\frac{-E_a}{RT}} \qquad 2$$

$$\ln(k) = \frac{-E_a}{R}\left(\frac{1}{T}\right) + ln(A) \qquad 3$$

Equation 3 shows the relationship between Arrhenius plot and $y = mx + c$ equation. From this relationship the activation energy can be obtained as follows;

$$m = \frac{-E_a}{R} \qquad 4$$

$$E_a = -m \times R \times 1000 \quad (5)$$

$$E_a = -(-4.1414\ K^{-1}) \times 8.314 J/molK \times 1000 \quad (6)$$

$$E_a = \sim 35\ kJ/mol \quad (7)$$

$$1 \frac{kJ}{mol} = 0.01\ eV \quad (8)$$

$$E_a = \sim 0.35\ eV \quad (9)$$

Appendix B

Derivation of chemical diffusion coefficient of water

Kreuer *et al* . derived the chemical diffusion coefficient of water using the Fick`s law of diffusion and assuming that the chemical diffusion of water occur by appropriate counter diffusion of protonic defects and oxygen vacancies [82].

The relationship between water, oxygen vacancies and protonic defects flux densities are given below:

$$J_{H_2O} = \frac{1}{2} J_{OH_o^{\bullet}} = -J_{V_o^{\bullet\bullet}} \quad (1)$$

The flux density of species *i* can be written as a function of its conductivity (σ), electrochemical potential (η) and electrostatic potential (Φ) as shown below [164]:

$$J_i = -\frac{\sigma_i}{n_i^2 F^2} \nabla \eta_i \quad (2)$$

Where η_i is the electrochemical potential, $\eta_i = \mu_i + n_i F\Phi$, *F* is the Faraday constant, n_i is the number of electrons involved in the reaction.

By substituting the electrochemical potential into Equation 1, the flux density can be obtained as follows:

$$J_i = -(\frac{\sigma_i}{n_i^2 F^2})\nabla \mu_i - (\frac{\sigma_i}{n_i F})\nabla \Phi \quad (3)$$

Assuming that the electrostatic potential within the membrane is constant and the gradient will become zero; the last term of Equation 2 can be eliminated.

The flux density can be written as a function of the diffusion coefficient and concentration using the Nernst–Einstein relation as follows:

$$\sigma_i = \frac{n_i^2 F^2 D_i C_i}{RT} \quad (4)$$

At equilibrium:

$$H_2O + V_o^{\bullet\bullet} + O_o^x \leftrightarrow 2OH_o^{\bullet} \quad (5)$$

$$\nabla\mu_{H_2O} = 2\nabla\mu_{OH_o^{\bullet}} - \nabla\mu_{V_o^{\bullet\bullet}} \quad (6)$$

By substituting $\nabla\mu$ of protonic defects and oxygen vacancies obtained from Equations 1, 2 and 3 into Equation 6, and converting the concentrations into the mole fractions ($C_i = \frac{X_i}{V}$, V is the total molar volume, cm^3/mol) the following equation can be obtained:

$$J_{H_2O} = -\frac{X_{OH_o^{\bullet}} D_{OH_o^{\bullet}} X_{V_o^{\bullet\bullet}} D_{V_o^{\bullet\bullet}}}{X_{OH_o^{\bullet}} D_{OH_o^{\bullet}} + 4X_{V_o^{\bullet\bullet}} D_{V_o^{\bullet\bullet}}} \frac{\nabla\mu_{H_2O}}{VRT} \quad (7)$$

In order to determine the chemical diffusion coefficient of water, an expression should be derived for the flux density of water that relates it to the concentration gradient of water. It may be now therefore manipulated as follows:

$$\mu_{H_2O} = \mu^0_{H_2O} - RT\ln a_{H_2O} \quad (8)$$

$$\nabla\mu_{H_2O} = RT\nabla\left(\ln a_{H_2O}\right)\frac{d(\ln C_{H_2O})}{d(\ln C_{H_2O})} \quad (9)$$

$$\nabla\mu_{H_2O} = W_{H_2O}\frac{RT}{C_{H_2O}}\nabla C_{H_2O} \quad (10)$$

Where $W_{H_2O} = \frac{dlna_{H_2O}}{dlnC_{H_2O}}$ is the thermodynamic factor and can be calculated as a function of $V_o^{\bullet\bullet}$, $OH_o^{\bullet}$ and H_2O as follows by differentiating Equations 6 and 8:

$$\frac{d\mu_{H_2O}}{dC_{H_2O}} = 2\frac{d\mu_{OH_o^{\bullet}}}{dC_{H_2O}} - \frac{d\mu_{V_o^{\bullet\bullet}}}{dC_{H_2O}} \quad 11$$

$$d\mu_i = RTlna_i \quad 12$$

By substituting $d\mu_i$ and $dC_{H_2O} = -dC_{V_o^{\bullet\bullet}} = \frac{1}{2}dC_{OH_o^{\bullet}}$ into Equation 11 and assuming that $\frac{d(lna_i)}{d(lnC_i)} = 1$ for defects of $V_o^{\bullet\bullet}$ and $OH_o^{\bullet}$, and converting concentrations into mole fractions W_{H_2O} can be obtained as follows:

$$W_{H_2O} = \frac{d(lna_{H_2O})}{d(lnC_{H_2O})} = \frac{2X_{V_o^{\bullet\bullet}} + X_{H_2O}}{X_{V_o^{\bullet\bullet}}} \quad 13$$

By combining Equations 7, 10 and 13, the following equation for the flux density can be obtained:

$$J_{H_2O} = -\frac{(2X_{V_o^{\bullet\bullet}} + X_{H_2O})D_{OH_o^{\bullet}}D_{V_o^{\bullet\bullet}}}{X_{H_2O}D_{OH_o^{\bullet}} + 2X_{V_o^{\bullet\bullet}}D_{V_o^{\bullet\bullet}}} \nabla C_{H_2O} \quad 14$$

Kreuer *et al* [82] defined the degree of hydration X as the fraction of oxygen vacancies in the dry state filled by *OH* groups:

$$X = \frac{C_{H_2O}}{C^0_{V_o^{\bullet\bullet}}} = \frac{X_{H_2O}}{X^0_{V_o^{\bullet\bullet}}} \quad 15$$

$$X^0_{V_o^{\bullet\bullet}} = X_{H_2O} + X_{V_o^{\bullet\bullet}} \quad 16$$

$$X_{V_o^{\bullet\bullet}} = 1 - X \quad (17)$$

Where, $C_{V_o^{\bullet\bullet}}^{0}$ is the concentration of oxygen vacancies in the dry state.

Finally, the flux density and the chemical diffusion coefficient of water can be obtained as a function of degree of hydration as follows:

$$J_{H_2O} = -\frac{(2-X)D_{OH_o^{\bullet}}D_{V_o^{\bullet\bullet}}}{XD_{OH_o^{\bullet}}+2(1-X)D_{V_o^{\bullet\bullet}}}\nabla C_{H_2O} \quad (18)$$

$$J_{H_2O} = -\widetilde{D}_{H_2O}\nabla C_{H_2O} \quad (19)$$

$$\widetilde{D}_{H_2O} = \frac{(2-X)D_{OH_o^{\bullet}}D_{V_o^{\bullet\bullet}}}{XD_{OH_o^{\bullet}}+2(1-X)D_{V_o^{\bullet\bullet}}} \quad (20)$$

Appendix C

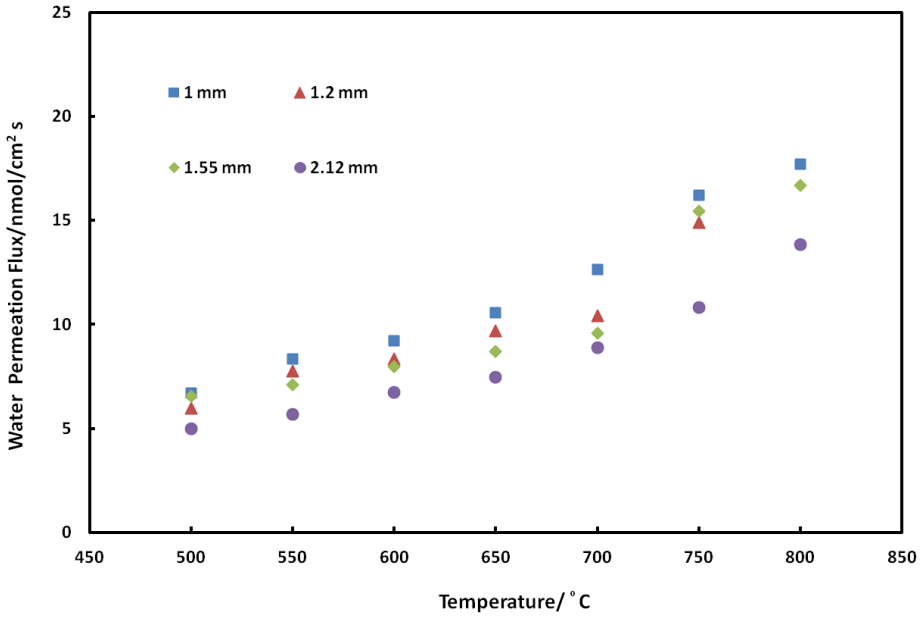

Figure C.4: Molar fluxes of water permeated through the BCY20 membrane for different membrane thicknesses (Feed side inlet gas concentration: 3% H_2O in nitrogen, permeate side inlet gas concentration: dry helium, flow rates of gases are 100 ml/min)

Appendix D

a)

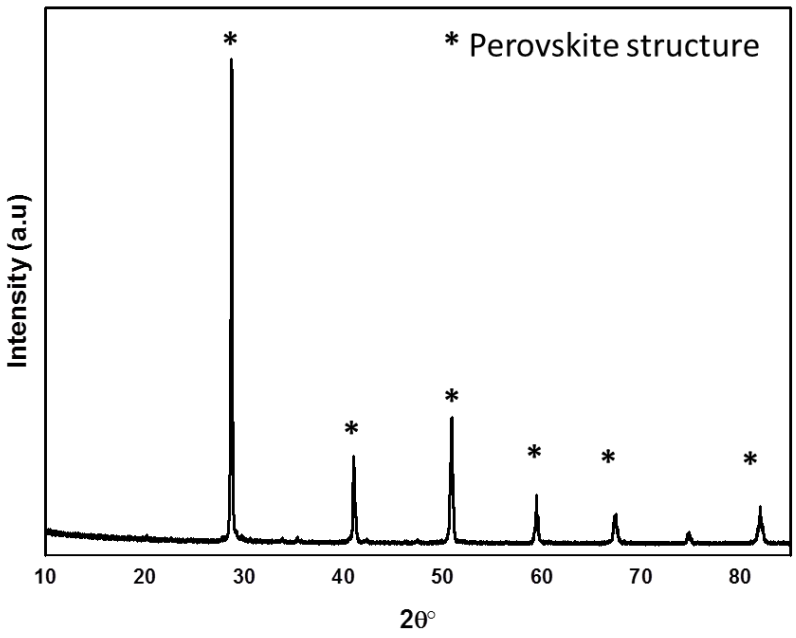

b)

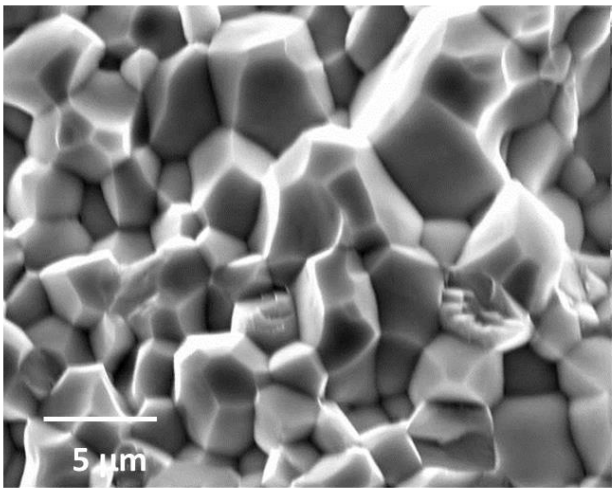

Figure D.5: a) XRD patterns of BCY10 pellets. **b)** cross section SEM image of BCY10. The pellets were sintered at 1450 °C for 12 hrs.

Appendix E

Comparison of data in hygrometer readings with theoretical values:

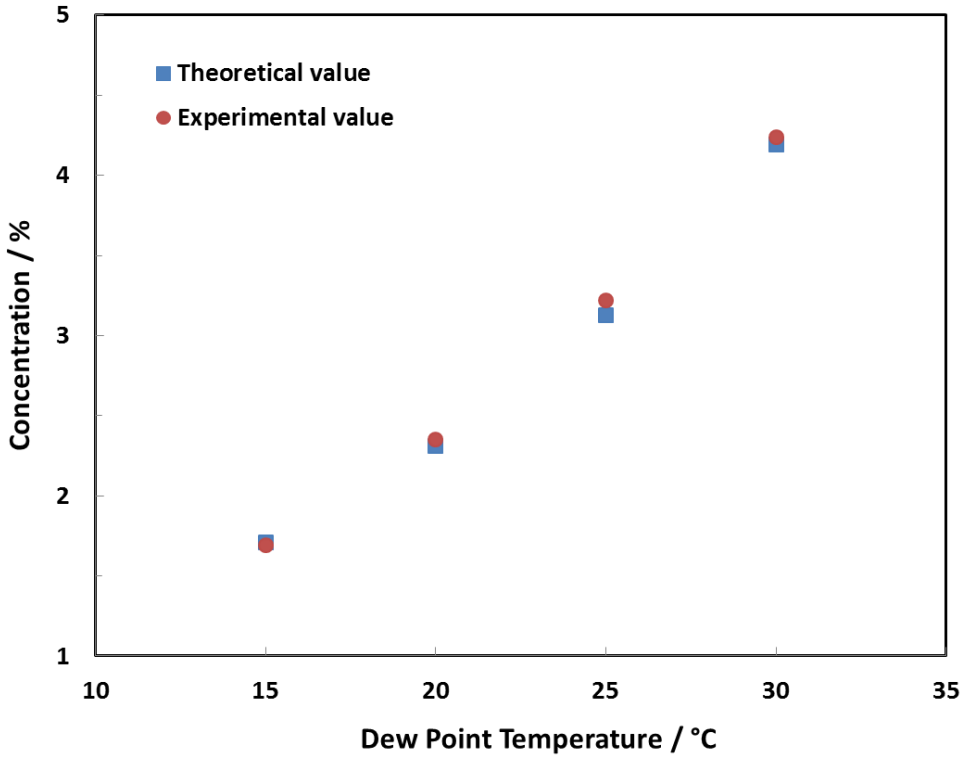

Figure E.6: Data comparison for the hygrometer

The minimum and maximum deviation in hygrometer readings were found as 0.8% and 3%.

Example:

Dew point temperature = 25 °C

Theoretical concentration at 25 °C = 31285 ppmV

Experimental value at 25 °C = 32201 ppmV

Referring to Equation 3.2:

$$\%Error = \frac{|31285 - 32201|}{31285} \times 100\% \approx 2.92\ \%$$

Appendix F

Calculating the rate of carbon dioxide for Water Permeation coupled with Water–Gas Shift Reaction Experiments

The rates of carbon dioxide during simultaneous water permeation and water–gas shift reaction experiments were determined in step there (Refer to Table 3.1). The contributions of other reactions to rate of carbon dioxide (e.g. a reaction between carbon monoxide and sealant) were subtracted which were determined after step three by running only argon the feed side instead of 3% H_2O in argon (we named this as blank run for the sake of calculation).

An example of the rate of carbon dioxide calculation:

Membrane configuration: BCY20

The mole fraction of carbon dioxide in step three at t_1 = 0.0368%

The mole fraction of carbon dioxide in blank run = 0.0260%

$$J_{CO_2} = [x - y]F\frac{1}{V_m}\frac{1}{60}\frac{1}{SA} = \frac{[0.0368-0.0260]}{100} \times 100\,\frac{ml}{min} \times \frac{1}{22400} \times \frac{1}{60} \times \frac{1}{0.5\,cm^2} \times 10^9 = 16\,nmol/cm^2$$

Appendix G

Calibration plots for different gases used in water permeation and water gas shifts experiments:

Calibration plot for water permeation experiments (gas mixture: N_2 (2%), O_2 (2%), H_2 (1%) balance in helium, flow rate of gas is 100 ml/min):

a)

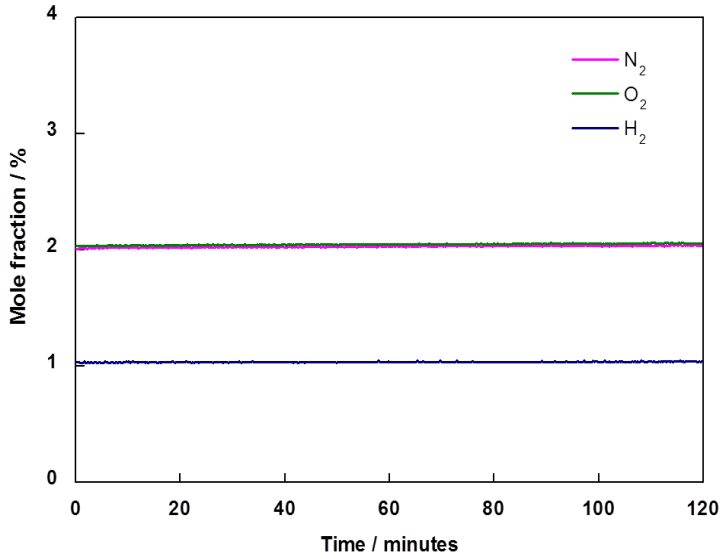

Calibration plot for water gas shift experiments (gas mixture; CH_4 (2%), CO (2%), O_2 (2%), CO_2 (2%), H_2 (2%) balance in helium, flow rate of gas 100 ml/min):

b)

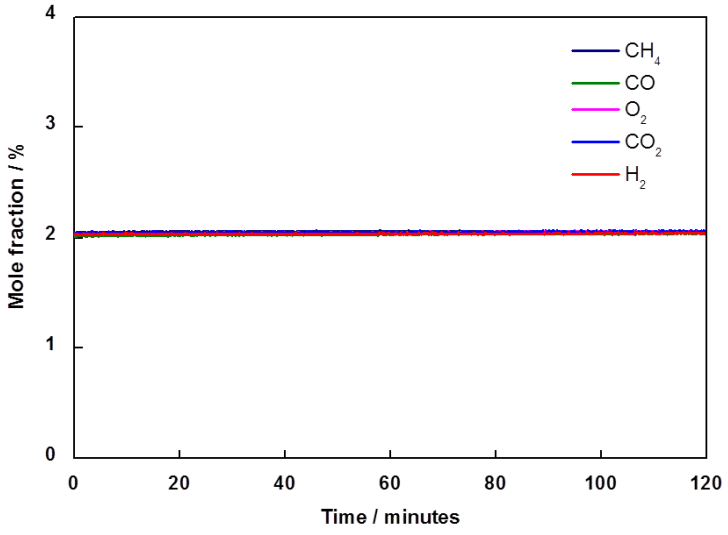

Figure G.7: Calibration curves for different gases employed in the experiments.

Appendix H

The initial concentrations of species for BCY20 ($BaCe_{0.8}Y_{0.2}O_{2.9}$) are calculated as follows:

1. 1 mole of BCY20 includes 2.9 mole of O_O^x , 0.2 mole of Y'_{Ce} and 0.1 mole of $V_O^{\bullet\bullet}$.

Molar mass of Ba = 137.33 g/mol

Molar mass of Ce = 140.12 g/mol

Molar mass of Y = 88.906 g/mol

Molar mass of O = 15.999 g/mol

Molecular weight of BCY20: $M_{BCY20} = 313.6\ g/mol$

2. Mole of BCY20:

$m_{BCY20} = 1.4\ g$

$$n = \frac{m}{M} = \frac{1.4\ g}{313.6\ g/mol} = 4.47 \times 10^{-3}\ mol$$

3. Volume of BCY20:

Membrane thickness = 1.44 mm

Membrane diameter = 15.08 mm

$$Volume(V) = \pi \times r^2 \times h = \pi \times (\frac{15.08}{2})^2 \times 1.44 = 257.19\ mm^3 = 257.19 \times 10^{-9}\ m^3$$

4. Concentration of species:

$$C_{BCY20} = \frac{n}{V} = \frac{4.47 \times 10^{-3}\ mol}{257.19 \times 10^{-9}\ m^3} = 1.7371 \times 10^4\ mol/\ m^3$$

$$C_{O_O^x} = 2.9 \times C_{BCY20} = 2.9 \times 1.7371 \times 10^4 = 5.0377 \times 10^4\ mol/m^3$$

$$C_{Y'_{Ce}} = 0.2 \times C_{BCY20} = 0.2 \times 1.7371 \times 10^4 = 3.4743 \times 10^3\ mol/m^3$$

$$C_{V_O^{\bullet\bullet}} = 0.1 \times C_{BCY20} = 0.1 \times 1.7371 \times 10^4 = 1.7371 \times 10^3\ mol/m^3$$

The initial concentrations of species for BCY10 ($BaCe_{0.9}Y_{0.1}O_{2.95}$) are calculated as follows:

1. 1 mole of BCY10 includes 2.95 mole of O_O^x , 0.1 mole of Y'_{Ce} and 0.05 mole of $V_O^{\bullet\bullet}$.

Molecular weight of BCY10: $M_{BCY10} = 319.5\ g/mol$

2. Mole of BCY10:

$m_{BCY10} = 1.482\ g$

$$n = \frac{m}{M} = \frac{1.482\ g}{319.5\ g/mol} = 4.64 \times 10^{-3}\ mol$$

3. Volume of BCY10:

Membrane thickness = 1.14 mm

Membrane diameter = 18.51 mm

$$Volume(V) = \pi \times r^2 \times h = \pi \times \left(\frac{18.51}{2}\right)^2 \times 1.14 = 306.76\ mm^3 = 306.76 \times 10^{-9}\ m^3$$

4. Concentration of species:

$$C_{BCY10} = \frac{n}{V} = \frac{4.64 \times 10^{-3}\ mol}{306.76 \times 10^{-9}\ m^3} = 1.513 \times 10^4\ mol/\ m^3$$

$$C_{O_O^x} = 2.95 \times C_{BCY10} = 2.95 \times 1.513 \times 10^4 = 4.4633 \times 10^4\ mol/m^3$$

$$C_{Y'_{Ce}} = 0.1 \times C_{BCY10} = 0.1 \times 1.513 \times 10^4 = 1.513 \times 10^3\ mol/m^3$$

$$C_{V_O^{\bullet\bullet}} = 0.05 \times C_{BCY10} = 0.05 \times 1.513 \times 10^4 = 7.565 \times 10^2\ mol/m^3$$

Appendix I

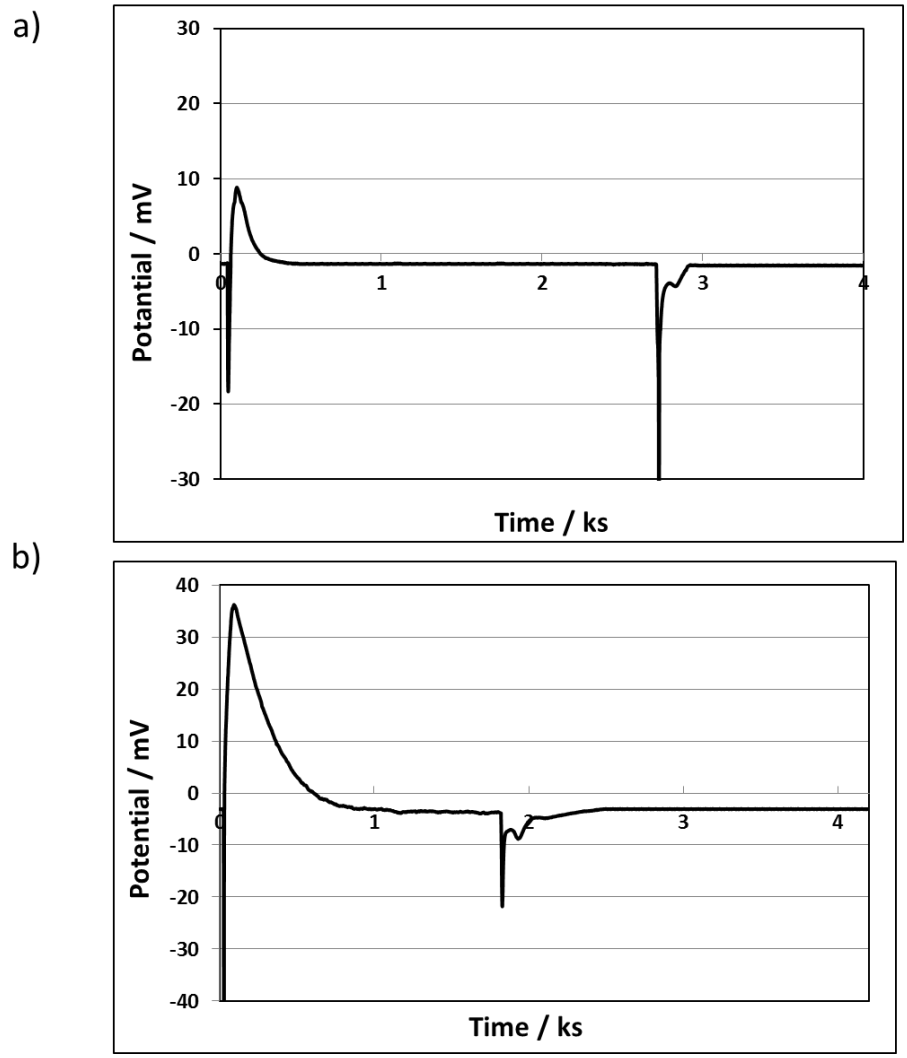

Figure I.8: The repeat measurement of the electrical potential difference of BCY membranes upon hydration and dehydration at 700 °C for Chapter 4 **a)** BCY20, **b)** BCY10.

Appendix J

Calculating average surface loading of platinum onto BCY20 membrane surface

The mass of platinum deposited on the BCY20 membrane surface was calculated by measuring the mass of unmodified BCY20 membrane and modified BCY20 membrane with platinum to find the amount of platinum deposited on the membrane surface. The samples were weighted right after; they were taken out of the furnace.

$$\text{Weight of unmodified BCY20 membrane} = 1.37\ \text{g}$$

$$\text{Weight of BCY20 membrane modified with platinum (one surface)} = 1.378\text{g}$$

$$\text{Amount of platinum deposited on BCY20 membrane surface} = 8\ \text{mg}$$

$$\text{Surface area of BCY20 that platinum deposited} = \pi \times r^2 = \pi \times (\frac{15.75\ \text{mm}}{2})^2 = 195\ \text{mm}^2 = 1.95\ \text{cm}^2$$

The average surface loading of platinum on BCY20 surface is given as follows:

$$\frac{\text{The amoun of platinum deposited on BCY20}}{\text{Surface area of BCY20 that platinum deposited}} = \frac{8\ \text{mg}}{1.95\ \text{cm}^2} = 4.1\ \text{mg/cm}^2$$

Estimation Porosity of Platinum Layer

The porosity of a layer is defined as the ratio of the pore volume to the total volume of the layer. Thus, the porosity of platinum layer that deposited on BCY20 membrane surface can be estimated as follows:

$$\text{Porosity} = \frac{\text{Pore volume}}{\text{Total bulk volume}} \times 100$$

$$\text{Pore volume} = \text{Total bulk volume} - \text{Grain (platinum)volume}$$

From the SEM analysis in Chapter 5, the thickness of platinum layer is:

$$\text{Platinum layer thickness} \approx 5\ \mu\text{m}$$

$$\text{Platinum layer diameter} = 15.75\ \text{mm}$$

Density of platinum $= 21.45\ \mathrm{g/cm^3}$

Weight of platinum layer $=\ 8\ \mathrm{mg}$

The bulk volume of platinum layer can be calculated roughly from the geometric dimensions as follows:

$$V_{bulk} = =\ \pi \times r^2 \times h =\ \pi\ \times (\frac{15.75\ \mathrm{mm}}{2})^2\ \times 5.10^{-3}\ \mathrm{mm} = 974\ \times\ 10^{-6}\ \mathrm{cm^3}$$

$$V_{grain} =\ \frac{m_{platinum}}{d_{platinum}} =\ \frac{8\ \times\ 10^{-3}\ \mathrm{g}}{21.45\ \mathrm{g/cm^3}} = 373\ \times\ 10^{-6}\ \mathrm{cm^3}$$

$$\text{Porosity} = \frac{974\ \times\ 10^{-6}\ \mathrm{cm^3} - \ 373\ \times\ 10^{-6}\ \mathrm{cm^3}}{974\ \times\ 10^{-6}\ \mathrm{cm^3}}\ \times 100\ \approx 61\ \%$$

Appendix K

Post Operation EDXS Results

Feed Side, Bare Surface

Table K-1: EDXS of the bare surface of BCY20 on the feed side after experiment.

Spectrum: Point

Element	AN	unn. C [wt.%]	norm. C [wt.%]	Atom. C [at.%]
Oxygen		12.83	14.39	58.1
Barium		73.64	82.54	38.8
Carbon		0.24	0.27	1.4
Cerium		1.95	2.19	1.0
Yttrium		0.43	0.48	0.3
Silicon		0.12	0.13	0.3
Total:		89.21	100.00	100.00

Table K-2: EDXS of the bare surface of BCY20 on the feed side after experiment.

Spectrum: Point

Element	AN	unn. C [wt.%]	norm. C [wt.%]	Atom. C [at.%]
Oxygen		17.31	17.20	61.9
Barium		78.91	78.41	32.9
Carbon		0.65	0.65	3.1
Cerium		3.32	3.30	1.4
Silicon		0.34	0.34	0.7
Yttrium		0.10	0.10	0.1
Total:		100.63	100.00	100.00

Permeate Side, Bare Surface

Table K-3: EDXS of the bare surface of BCY20 on the permeate side after experiment.

Spectrum: Point

Element	AN	unn. C [wt.%]	norm. C [wt.%]	Atom. C [at.%]
Barium	56	61.75	74.88	25.38
Oxygen	8	19.37	23.48	68.31
Carbon	6	1.34	1.63	6.31
Cerium	58	0.00	0.00	0.00
Yttrium	39	0.00	0.00	0.00
Total:		82.46	100.00	100.00

Table K-4: EDXS of the bare surface of BCY20 on the permeate side after experiment.

Spectrum: Point

Element	AN	unn. C [wt.%]	norm. C [wt.%]	Atom. C [at.%]
Barium	56	67.65	73.50	24.41
Oxygen	8	22.15	24.06	68.58
Carbon	6	1.62	1.76	6.66
Yttrium	39	0.63	0.68	0.35
Cerium	58	0.00	0.00	0.00
Total:		92.04	100.00	100.00

Permeate Side, Platinum Surface

Table K-5: EDXS of the platinum surface of BCY20 on the permeate side after experiment.

Spectrum: Point

Element	AN	unn. C [wt.%]	norm. C [wt.%]	Atom. C [at.%]
Carbon		15.46	15.88	73.90
Platinum		75.02	77.03	22.10
Barium		6.24	6.41	2.60
Silicon		0.67	0.69	1.40
Yttrium		0.00	0.00	0.00
Cerium		0.00	0.00	0.00
Total:		97.39	100.00	100.00

Table K-6: EDXS of the platinum surface of BCY20 on the permeate side after experiment.

Spectrum: Point

Element	AN	unn. C [wt.%]	norm. C [wt.%]	Atom. C [at.%]
Carbon		14.14	14.90	72.00
Platinum		72.27	76.14	22.60
Barium		7.58	7.99	3.40
Silicon		0.93	0.98	2.00
Yttrium		0.00	0.00	0.00
Cerium		0.00	0.00	0.00
Total:		94.92	100.00	100.00